TUM School of Computation, Information and Technology

Organ-on-a-chip: Engineering of microfluidic large-scale integration chip technologies for 3D human stem cell cultures

Nina Huber

Vollständiger Abdruck der von der TUM School of Computation, Information and Technology der Technischen Universität München zur Erlangung des akademischen Grades einer

Doktorin der Ingenieurwissenschaften (Dr.-Ing.)

genehmigten Dissertation.

Vorsitz: Prof. Dr.-Ing. Christian Jirauschek

Prüfende der Dissertation:

1. Prof. Dr. Bernhard Wolfrum
2. Prof. Dr. Berna Özkale Edelmann

Die Dissertation wurde am 08.06.2022 bei der Technischen Universität München eingereicht und durch die TUM School of Computation, Information and Technology am 16.11.2022 angenommen.

Zusammenfassung

Um die physiologische Relevanz von *in-vitro*-Zellmodellen zu erhöhen, wird daran geforscht die *in-vivo*-Umgebung der Zelle mittels dreidimensionaler (3D) Kulturen humaner Stammzellen und der sogenannten Organ-on-a-Chip-Technologie räumlich wie zeitlich möglichst präzise *in vitro* nachzubilden. Trotz enormer Fortschritte auf diesem Gebiet ermöglichen nur sehr wenige Organ-on-a-Chip-Plattformen die Möglichkeit zur Automatisierung und Parallelisierung, was deren Einsatz für industrielle Anwendungen limitiert. Die Microfluidic Large-Scale Integration (mLSI) Technologie, die die parallele Durchführung mehrerer hunderter biologischer Untersuchungen am Zellgewebe mit verschiedensten Reagenzien ermöglicht, hat das Potenzial, diesen Mangel an Hochdurchsatzkompatibilität zu überwinden. Die Technik wurde bereits für viele zweidimensionale (2D) Zellkulturprozesse angewandt, aufgrund von Einschränkungen in der Herstellung ihres zentralen Funktionselements, des pneumatischen Membranventils (PMV), ist die Technologie bisher jedoch mit Gewebekulturen und Organoide mit Abmessungen von mehr als einigen zehn Mikrometern nicht kompatibel.

Um diese Einschränkung zu beheben, wurde in dieser Arbeit untersucht, inwieweit sich die Kompatibilität der mLSI-Technik mit humanen 3D-Stammzellkulturen mittels der Verwendung additiver Fertigungsverfahren erreichen lässt. Zu diesem Zweck wurden zunächst drei handelsübliche Druckmaterialien in Bezug auf Druckauflösung, Oberflächenrauheit und Biokompatibilität charakterisiert. Zwei von ihnen erwiesen sich aufgrund ihrer geringen Oberflächenrauhigkeit bzw. hohen Biokompatibilität als geeignet für die Herstellung von Gussformen für den Abguss von Polydimethylsiloxan (PDMS) sowie die Fertigung monolithischer Mikrofluidik-Chips. Während die Entwicklung eines monolithischen Mikrotiterplatteneinsatzes zur Generierung, Kultivierung und Analyse von humanen 3D-Stammzellkulturen in Standard-Gewebekulturplatten ebenfalls gezeigt wird, lag der Schwerpunkt dieser Arbeit auf der Entwicklung von PDMS-basierten mLSI-Chiptechnologien. Hierfür wurde ein robuster Herstellungsprozess entwickelt, der eine Kombination aus 3D-gedruckten Gussformen, deren Oberflächenbeschichtung und herkömmliche Soft-Lithographie-Verfahren nutzt, um PMVs mit Fließkanalhöhen von mehr als 100 µm zu fertigen und so Kompatibilität mit 3D-Zellkulturabmessungen zu erreichen. Auf Basis dieser hochskalierten PMVs wurde dann eine funktionale Elementareinheit für die Generierung und Langzeitkultur von 3D-Zellkulturen entworfen und charakterisiert. Die serielle und parallele Anordnung dieser Elementareinheit sowie die Integration weiterer hochskalierter PMVs zur zerstörungsfreien Manipulation von 3D-Zellkulturen auf zwei speziell entwickelten mLSI-Plattformen ermöglichte 1) die automatisierte Fusion von 3D-Zellkulturen innerhalb eines definierten Flussprozesses und 2) die automatisierte und zuverlässige Generierung, Langzeitkultivierung und Analyse von aus Stammzellen gewonnenen Adipozytenorganoiden in hohem Durchsatz. Letztere ermöglichte dank der zerstörungsfreien Wiedergewinnung der

Adipozytenorganoide und anschließender Massenspektroskopie, eine detaillierte Charakterisierung der Organoide auf Proteinebene zusätzlich zur klassischen bildgebungsbasierten Analyse während der Kultivierung.

Die im Rahmen dieser Arbeit entwickelte additive Fertigungsstrategie für die Hochskalierung von PMVs gemeinsam mit den hier vorgestellten mLSI-Plattformen sollen zukünftig neue Entwicklungen für Hochdurchsatz-Screeninganwendungen von 3D-Zellkulturen fördern und den generellen Einsatz von Organ-on-a-Chip-Technologien in einem industriellen Kontext vorantreiben.

Abstract

To increase the physiological relevance of *in vitro* models, researchers aim to mimic the cell's *in vivo* microenvironment with high spatiotemporal precision *in vitro* by combining three-dimensional (3D) human stem cell cultures and organ-on-chip technology. Despite huge progress in this field, only very few organ-on-a-chip platforms allow for automation and parallelization, thus limiting the adoption of the technology for applications in an industrial scale. By enabling the execution of several hundreds of cell assays with multiple reagents in parallel, a technology called microfluidic large-scale integration (mLSI) has the potential to overcome this lack of high-throughput compatibility. This technique has already been applied for many two-dimensional (2D) cell culture processes, but manufacturing limitations of the central functional element, the pneumatic membrane valve (PMV), make the technology inaccessible for integrating tissue cultures and organoids with dimensions larger than tens of microns.

To address this shortcoming, this work investigated the feasibility of additive manufacturing technologies, *i.e.* 3D printing, to render the mLSI technique compatible with 3D human stem cell cultures. For this, three commercially available printing materials have first been characterized in terms of printing resolution, surface roughness, and biocompatibility. Among them, two proved suitable for the fabrication of either polydimethylsiloxane (PDMS) replica molds or monolithic microfluidic chips due to their low surface roughness and high biocompatibility, respectively. While the development of a monolithic microwell insert to enable the formation, culture, and analysis of 3D human stem cell cultures in standard tissue culture plates is also shown, the main focus of this work lay on the development of PDMS-based mLSI chip technologies for 3D human stem cell cultures. For this, a robust manufacturing process that combined 3D-printed molds, surface coating of these, and traditional multi-layer soft lithography was developed to upscale PMVs to flow channel heights greater than 100 µm and thus, yield compatibility with 3D cell culture dimensions. Based on upscaled PMVs, a functional unit cell for the formation, long-term culture, and reversible trapping of 3D cell cultures has been designed and characterized. Arraying of this unit cell and integration of upscaled PMVs for non-destructive handling of 3D cell cultures on two mLSI platforms allowed for 1) the automated fusion of 3D cell cultures within a defined flow process and 2) high-throughput generation, long-term culture, and analysis of stem cell-derived adipocyte organoids in an automated and reliable manner. Further, the combination of the latter platform with mass spectrometry complemented the imaging-based analysis by a detailed characterization of the organoids on a proteomic level.

The additive manufacturing strategy for upscaling PMVs as well as the mLSI platforms presented in this thesis will hopefully foster new developments for highly parallel 3D cell culture screening applications and spur the adoption of organ-on-a-chip technologies in an industrial context.

Acknowledgments

I would like to thank the following people, without whom I would not have been able to successfully complete this work!

First of all, I want to thank my two supervisors, Dr. Matthias Meier at the Helmholtz Center Munich and Prof. Dr. Bernhard Wolfrum at the TUM, for giving me this opportunity to pursue my interests in biomedical and engineering research as well as their insight and knowledge into the subject. Thanks for the interesting and enriching discussions and the trust in my work. A special thanks also goes to Prof. Dr. Claas Müller for being my mentor, asking critical questions, and providing highly valuable input especially when it came to the engineering part of my research. Thank you also to Prof. Dr. Berna Özkale Edelmann for being my second examiner and Prof. Dr.-Ing. Christian Jirauschek for being chairman in my defense. I could not have had a better thesis committee.

I also want to thank my working group at the Helmholtz Center for the creative and helpful exchange, for inspiring discussions and for the continuous support through the ups and downs of my projects. I would not have been able to finish my PhD without you! A special thanks goes to Dr. Scott Atwell, who taught me a lot of the knowledge I now have and helped me realize my own ideas. The discussions with him were always a valuable contribution to my work. Further, I want to thank the neuroelectronics working group at the TUM, especially Dr. Philipp Rinklin and Lennart Weiß, whom I could always contact if I needed any help and the nice working atmosphere. I also want to thank Dr. Christine von Törne and the Research Unit Protein Science for the preparation and proteomic analysis of my samples and their valuable feedback concerning the design of experiments and downstream analyses. Many thanks also to all the doctoral students, post-doctoral researchers, and the admin team of the Helmholtz Pioneer Campus, as well as the teams of the IDR and ITS for the time spent together, inspiring exchange, and their support whenever needed.

Most importantly I want to thank my partner, my family and my friends for their great support, their patience, their curiosity in my work and for the distraction from work when I needed it. Many thanks to Yves, Christian, and Grit for encouraging me in the decision to pursue a PhD as well as their professional and personal advices during this time. A special thanks goes to my partner Johannes, who never got tired of our discussions whether it’s about work, philosophy or the world, and whose honesty and feedback were always a highly valuable contribution not only to my work but to me growing as a person. I would not have been able to finish this work without you!

Ein besonderer Dank geht an meine Eltern Marianne und Manfred und meinen Bruder Maxi sowie Andrea und meinen Onkel Peter, die mich immer in allen meinen Entscheidungen unterstützt und ermutigt haben. Ihr habt mir stets ermöglicht meinen eigenen Weg zu finden und zu gehen und mir das nötige Selbstvertrauen und den Mut dafür mitgegeben. Danke für alles!

Table of Contents

Abbreviations

2D	Two-dimensional
3D	Three-dimensional
ABS	Acrylonitrile butadiene styrene
ASC	Adult stem cells
BSA	Bovine serum albumin
CAD	Computer-aided design
DEM	Deflection of an elastomeric membrane
DI	Deionized
DLP	Digital light processing
DMD	Digital micromirror-array device
DMEM	Dulbecco’s Modified Eagle Medium
EC	Endothelial cell
ECM	Extracellular matrix
ESC	Embryonic stem cells
EtOH	Ethanol
FBS	Fetal bovine serum
FDM	Fused deposition modeling
FGF	Fibroblast growth factor
hASC	Human adipose tissue-derived adult stem cells
HBP	Hepato-biliary-pancreatic
iPSC	Induced pluripotent stem cells
MJM	Multi-jet modeling
mLSI	Microfluidic large-scale integration
MSC	Mesenchymal stem cells
MSL	Multilayer soft lithography
MW	Microwell
PBS/DPBS	(Dulbecco’s) Phosphate-buffered saline
PDMS	Polydimethylsiloxane
PEG	Poly(ethylene glycol)
PEG-DA	Poly(ethylene glycol) di(acrylate)
PFA	Paraformaldehyde
PJ	Photopolymer inkjet printing
PJM	Poly-jet modeling
PLA	Poly-lactic acid
PLLA	Poly(l-lactide) acid
Poly-HEMA	Poly(2-hydroxyethyl methacrylate)
PMV	Pneumatic membrane valve

PS	Polystyrene
PSC	Pluripotent stem cell
RT	Room temperature
SD	Standard deviation
SEBS	Styrene-ethylene-butylene-styrene
SGBS	Simpson Golabi Behmel syndrome
SL/SLA	Stereolithography
TPE	Thermoplastic elastomer
TPU	Thermoplastic polyurethane
ULA	Ultra-low attachment
UV	Ultra-violet
WST-8	2-(2-methoxy-4-nitrophenyl)-3-(4-nitrophenyl)-5-(2,4-disulfophenyl)-2H-tetrazolium monosodium

List of symbols

∇	Nabla operator
∇^2	Laplace operator
A	absorption
d	diameter
$\frac{\partial u}{\partial y}$	shear rate
$\boldsymbol{f}$	acceleration field
γ	dynamic viscosity
h	height
L	characteristic length
p	pressure
Q	flow rate
r	radius
R_a	surface roughness
Re	Reynold’s number
R_H	hydraulic resistance
ρ	density
τ	shear stress
$\boldsymbol{u}$	velocity field
u	velocity
w	width

1. Introduction

Human physiology both healthy and diseased is governed by a myriad of complex, intertwined mechanisms which are inherently difficult to study due to limited accessibility and ethical concerns regarding experimental perturbations *in vivo*.[1] Hence, biomedical and pharmaceutical research heavily relies on the use of *in vitro* cell culture models to investigate human (patho-) physiology and develop new treatment strategies for various diseases, *e.g.* diabetes mellitus, cancer, or cardiovascular diseases.[2–4] Traditionally, the two-dimensional (2D), monolayer culture of primary or immortalized cell lines has been used as an *in vitro* model system due to its accessibility. However, these systems fall short in mimicking various features of the native, three-dimensional (3D) cellular microenvironment such as the cell-to-cell and cell-to-extracellular matrix (ECM) interactions.[1,5] Especially the lack of important ECM signals has been attributed to the challenges encountered in the long-term maintenance and expansion of *e.g.* primary pancreatic islets or liver cells in 2D *in-vitro* cultures.[6–8] In contrast, immortalized cell lines are well established and allow for serial passaging but suffer from limited physiological relevance due to genetic alterations.[3,4] Hence, there has been an increasing effort in the generation of more reliable and complex *in vitro* models *e.g.* by incorporating different cell types, differentiation of stem cells, and three-dimensional (3D) culture modalities. In particular, the emergence of organoids, by now generated for a large variety of tissues, rapidly developed as a promising alternative for studying organ development and disease.[1] Organoid technology relies on the intrinsic self-organization properties of stem cells to form a multicellular, highly organized structure, which resembles key phenotypic and genetic hallmarks of their native counterpart.[9–11] Organoids typically originate from stem cells, which are cultured in 3D using *e.g.* hydrogel matrices[12], ultra-low attachment wellplates[11], or microwells[13,14] and differentiated towards organ-specific cell types mostly by use of chemical induction. Despite the striking possibilities of organoids, the technology suffers from generally low standardization and a lack of analytical tools to monitor and thoroughly characterize the organoids' phenotype, thus hindering the widespread application of organoids in pharmaceutical drug development.[1,15]

To develop an even more powerful *in vitro* model of human organ physiology that goes beyond current organoid technology, researchers aim to incorporate 3D human stem cell cultures in organs-on-chips. In contrast to organoids which rely on the intrinsic developmental programs of stem cells, organs-on-a-chip try to recapitulate the minimal functional unit of a human organ in an engineered system with the help of microfluidics and microfabrication techniques.[2,4] To emulate the key functional aspects of a human organ on a microfluidic device, the essential components of the organ-specific local environment including cellular tissue composition, oxygen, and nutrient availability, presence of morphogen gradients and mechanical forces, and physical confinements need first to be identified and then engineered accordingly on the artificial system. Up to date, a variety of microfluidic design elements such as microfabricated structures to attain three-dimensional arrangement of the cells[16], perfusion of cells to simulate the flow-induced shear stress present in blood vessels[17], or the integration of hydrogels to mimick tissue barriers[18] have been suggested to allow for precise control of the cellular microenvironment while ensuring accessibility and reproducibility. Despite huge progress in achieving physiologically highly relevant *in vitro* models, only very few organ-on-a-chip platforms allow for automation and parallelization, thus limiting throughput and consequently, the adoption of the technology for pharmaceutical drug development.[19,20]

By enabling parallel and automated execution of several hundreds of cell assays with multiple reagents, a technology called microfluidic large-scale integration (mLSI) has the potential to overcome this lack of high-throughput compatibility.[21] The key component of mLSI chips are pneumatic membrane valves (PMVs) which control fluid flow on-chip through pneumatic actuation. As the name implies mLSI systems typically integrate hundreds to thousands of these valves on a single chip to execute complex tasks such as single-cell analysis[22], automated stem cell differentiation[23–25], cell-to-cell communication studies[26], biomarker detection[27,28], and drug screening[29,30]. Most of these platforms utilize 2D cell cultures as these are well-established and the channel dimensions of the mLSI technique matched with those required for monolayer cultures. While the importance of 3D cell cultures for *in vitro* organ modeling has been advancing and the benefits of microfluidics for such applications have been recognized[31], only a few of the organs-on-a-chips currently presented in the literature are based on the mLSI technique.[24,32] This is likely due to challenges encountered in the traditional production of mLSI chips, namely multilayer soft lithography[33] (MSL), with flow channel heights greater than 100 µm, the minimum dimensional requirement for processing 3D cell cultures. To address this shortcoming, other microfabrication technologies[34] have been exploited for the production of mLSI platforms.

The emergence of highly precise additive manufacturing technologies, *i.e.* 3D printing, has attracted broad interest in the field of microfluidics due to its high design flexibility, rapid prototyping, and achievable aspect ratios of up to 37:1.[35] For example, it has been utilized for the fabrication of soft lithography molds[36–38], standardized micro-to-macro interfaces[39,40], reconfigurable microfluidic modules[41,42], and whole microfluidic chips[43,44]. Despite ongoing technological advances in the field, 3D printing of microfluidic chips is up to now not widely implemented due to limitations regarding achievable resolution, surface quality, autofluorescence, solvent compatibility, gas permeability, and biocompatibility.[45,46] In contrast to the direct printing approach, 3D printing of molds provides numerous advantages of additive manufacturing while maintaining the desirable material properties of the widely used polydimethylsiloxane (PDMS), such as flexibility and oxygen permeability. However, the previously mentioned concerns in terms of printing resolution and material properties, such as surface roughness or biocompatibility remain valid also for this approach.

1.1 Aims of the thesis

To address the aforementioned limitations of the mLSI technology and additive manufacturing of organ-on-a-chip devices, the aims of this thesis were to

i. investigate and characterize 3D printing as an alternative fabrication technique for microfluidic chips in general and mLSI platforms in particular,
ii. develop and optimize manufacturing workflows to render the mLSI technique compatible with 3D cell cultures,
iii. develop and characterize mLSI-based organ-on-a-chip platforms to culture human stem cell-derived organoids in an automated and high-throughput manner, and
iv. integrate the platforms in existing on- or off-chip analytical workflows for detailed phenotypic characterization of the cultured organoids.

1.2 Structure of the thesis

This manuscript is organized as follows: A summary of the scientific context of the thesis is given in chapter 2. In chapters 3 to 5 the results of three interconnected projects are presented and evaluated in the light of relevant literature. The manuscript concludes with a short summary of the obtained results and an outlook on future organ-on-a-chip devices in chapter 6.

In the following, the structure of the results is outlined in detail. The characterization of the resolution and surface roughness of three commercially available printing materials is presented in chapters 3.2.1 and 3.2.2 and generally demonstrated the suitability of the chosen 3D printing process, namely stereolithography, for the fabrication of microfluidic channels. Both, 3D printing of replica molds and direct printing of monolithic microwell arrays, required the development of specific post-processing protocols to enable the culturing of human stem cells as elaborated on in chapters 3.2.3 and 3.2.4. Since directly 3D-printed monolithic devices suffered from several limitations including autofluorescence and minimal biocompatibility despite excessive post-processing, subsequent work focused on 3D-printed molds to upscale PMVs and thus, render the mLSI technique compatible with 3D cell cultures. Development of a robust manufacturing process that combined 3D-printed molds, surface coating of these, and traditional MSL yielded an upscaling of PMVs for flow channels with heights greater than 50 µm (chapter 4.2.1). During the characterization of the upscaled PMVs' operating range, a diminished performance due to staircase effects on the surface of the flow mold, that have been replicated in the PDMS layer, was observed. Systematic investigation of grayscale light exposure and thermal reflow processes lead to a reduction of the staircase effect and restored the function of the upscaled PMVs (chapter 4.2.1). Based on this, an mLSI platform that enabled the parallel formation, culture, processing, and fusion of 3D cell cultures within a defined flow process has been developed and characterized (chapters 4.2.2 and 4.2.3). Utilizing the same functional unit cell principle, a second mLSI-based organ-on-a-chip device has been developed to further exploit the benefits of the mLSI technology in terms of automation and parallelization (chapter 5.2.1). This platform enabled the formation, long-term culture, differentiation, and non-destructive retrieval of 96 human adipose microtissues in parallel as highlighted in chapter 5.2.2. Integrating this platform with a mass spectrometry-based analytical pipeline complemented the imaging-based analysis with a detailed characterization of the organoids on a proteomic level (chapter 5.2.3).

2. Fundamentals and state of the art

In the first two sections of this chapter the basics of human stem cell culture, the general concept of organ-on-a-chip technology, and current trends in this field in terms of scale-up, are presented. The following section focuses on a specific microfluidic technique, namely microfluidic large-scale integration, which holds promise to spur the envisioned scale-up of the organ-on-a-chip technology and was the core focus of this thesis. The remaining section provides an overview of 3D printing concepts in the context of microfluidic chip fabrication as the majority of the work presented later in this thesis made use of this additive manufacturing technique.

2.1 Human stem cell culture

In contrast to primary cells or cell lines, stem cells possess the unique capability to develop into various cell types of the human body. Their differentiation towards a specific cell type of the human body is orchestrated by various biochemical and –physical cues in a precise spatiotemporal manner. During human organogenesis, never all stem cells mature into a specific cell type, but certain stem cell niches remain in the adult organism. The stem cells in these niches can be recruited if needed for example for tissue regeneration. They provide a great tool to study the (patho-) physiology of human organs as they develop from the earliest cell type of a cell lineage into a specialized cell type of tissue with specific morphology and function. Stem cells display a high self-renewal capability, leading to the production of new stem cells as well as cells committing to differentiation during stem cell division. This continuous proliferation of stem cells ensures the maintenance of the stem cell population. Depending on the development stage of the organism, stem cells are discriminated into **embryonic** (ESC) and **adult stem cells** (ASC). ASCs can also be reprogrammed following a groundbreaking approach that was first presented by the research group of Yamanaka in 2007 to obtain **induced pluripotent stem cells** (iPSCs).[47] iPSCs display similar morphological, proliferative, transcriptional, and *in vitro* differentiation characteristics to ESCs but bear fewer ethical concerns. Thus, their use for *in vitro* studies investigating human organogenesis and morphogenesis has increased tremendously over the last decade. A short overview of culture modalities and the application of stem cells for organ modeling is given in the following two chapters.

2.1.1 Traditional culture modalities

During embryogenesis, morphogenesis, and organogenesis, cells respond to various systemic and local biochemical and physical cues such as morphogen gradients[48], mechanical forces[49], or heterogeneous cell-to-cell contacts[50] by self-organization. Traditional 2D adherent **monolayer cultures** fall short to recapitulate this highly complex, 3D microenvironment *in vitro*.[5] Thus, in recent years the cultivation of cells in a 3D architecture has gained great interest as these systems better emulate important cell-to-cell and cell-to- ECM interactions present *in vivo*. As most cells aggregate in a sphere-like architecture, these aggregates are often called **spheroids**.

Various approaches to forming **3D cell cultures** have been proposed in the last couple of years, which can be mainly subdivided into two categories: scaffold-free and scaffold-based approaches. Commonly used techniques for the formation of 3D cell cultures are illustrated in **Figure 2.1**. While scaffold-free approaches rely on the intrinsic self-organization properties of cells when not being able to attach to any kind of surface[51], scaffold-based approaches mostly rely on an external hydrogel matrix for the cellular spatial arrangement. For the latter, different biomaterials, for example, fibrin[52], collagen[53], or hyaluronic acid[54], have been employed.[55] In contrast, in bioreactors, one of the most prominent scaffold-free techniques, a high-density cell suspension is continuously agitated to minimize cell attachment to the surface and thus, create cell aggregates. By adjusting the agitation speed and cell density the size of formed spheroids can be controlled. Despite the good scalability of this approach, its application needs careful consideration as some cell types including MSCs are very sensitive to the microenvironment.[56] To minimize the risk of unintentional alterations of the cell's physiology, 3D cell cultures can also be generated by the hanging drop method. In this, 15 – 30 µL drops of the cell suspension are dispensed onto the underside of the lid of a culture dish.[57,58] Upon inverting the lid, cells aggregate at the free liquid-air interface by gravity. Spheroids of various cell types[57] and compositions[59] have been formed and cultured successfully in hanging drops both in mono- as well as co-cultures[60]. The spheroid size can be precisely controlled by the initial density of the cell suspension.[59,61] However, the method suffers from a high risk of spheroid loss during medium change and spheroid transfer.[62] Another popular approach for spheroid generation is

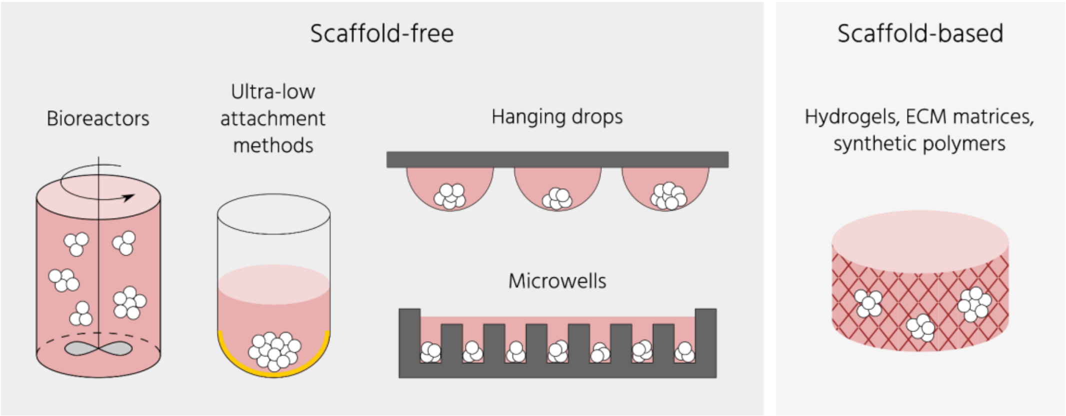

Figure 2.1 Overview of traditional fabrication methods for 3D cell cultures. 3D cell culture approaches are subdivided into scaffold-free and scaffold-based techniques. Scaffold-free techniques typically employ agitation or anti-adhesive coatings to promote cellular self-aggregation. Opposed to this, scaffold-based approaches make use of external matrices to spatially arrange cells in 3D.

an ultra-low attachment (ULA) substrate. Here, the cell culture substrate is either chemically or topologically modified such that cells are unlikely to attach and thus, aggregate and form a spheroid. One benefit of this technique is its versatility, as many normal culture substrates can be modified afterward to become low-adherent by coating with agarose[63] or polymer hydrogels such as *e.g.* poly(2-hydroxyethyl methacrylate) (poly-HEMA)[62]. Besides customized modification of the substrate, also a wide range of commercial ULA culture ware exists. High variability of the size of generated spheroids[64], as well as low efficiency[65] often make the technique inferior to other 3D cell culture approaches. To create more uniform 3D cell cultures, microwell arrays have been proposed. The size[66], shape[67,68], and aspect ratio[69] of the microwells can be precisely adjusted, thus, enhancing the formation of a single spheroid instead of several fragmented aggregates as often seen on ULA substrates[64]. Similar to ULA substrates, the microwells' surface is usually coated with an anti-adhesive agent such as Pluronic F127.[61,67] As these systems are often operated in a static culture condition, mass transfer is easily limited in the microwell causing waste accumulation and low oxygen levels within the spheroid.[68,70]

2.1.2 Organoids

Organoids are **stem cell-derived multicellular 3D aggregates** that self-organize into an organ-like structure *in vitro*. They mimic the architecture, function, and genetic signature of a organ in a simplified setup[1] and thus, are a great tool to study the underlying mechanisms of human organogenesis and morphogenesis[50], to unravel molecular pathways of diseases and potential drug targets, or apply them in regenerative medicine. Organoids typically originate from pluripotent or tissue-resident adult stem cells which are cultured in 3D. When using ASCs for the generation of organoids, signaling factors normally provided by the surrounding microenvironmental niche of the respective adult tissue need to be supplied *in vitro* to emulate the homeostatic conditions of the resident tissue and guide ASC-organoid formation. Due to the restricted potency of ASCs, only tissue-specific organoids can be obtained. In contrast, pluripotent stem cells such as ESCs and iPSCs have the capacity to differentiate into multiple cell lineages and hence, are often the preferred cell source for organoids. By exposing human iPSCs to specific chemical, physical, mechanical, and biological cues, they can be differentiated into organ-specific cell types by sequential addition and/or removal of the instructive cues to mimic the stages of the human developmental process.[71] During the differentiation, cellular intrinsic programs drive the **self-organization** of the organoid to reproduce key structural and functional properties of their *in vivo* counterparts. Organoids for a diverse range of tissue types have been generated by the use of pluripotent stem cells so far, including for example the liver[72], kidney[49], pancreas[9,72], intestine[10], and brain[11].

The differentiation and self-organization process of stem cells is influenced by various local and systemic cues of the cellular microenvironment. Early work in the field of stem cell research focused on investigating and controlling key processes of the differentiation's stochastic nature. As such, it has for example been highlighted that the initial stem cell spheroid size affects differentiation efficiency. Human iPSC spheroids with an initial size of 600 µm exhibited a 1- and 8-fold increase in the hepatic gene expression markers ALB and CYP3A4 compared to ones with an initial size of 250 µm, thus, indicating enhanced hepatic maturation of the larger spheroids.[73] Enhanced differentiation was also observed for the generation of neural organoids when initially incorporating MSCs at various ratios in an iPSC-spheroid and subsequent differentiation of the heterotypic aggregate.[74] More recent approaches in stem cell and organoid research concentrate on increasing the organoid complexity as well as its maturation and functionality *in vitro* by incorporating cell types, which are shared across several organs such as *e.g.* blood vessels.[1,75] Despite the huge progress being made in the field, generally low standardization and scalability of presented methods hinder the widespread application of organoids in precision and regenerative medicine, as well as in pharmaceutical drug development, where they could serve as a surrogate for animal models.[76,77]

2.2 Organ-on-a-chip technology

Compared to organoids, which rely on the intrinsic self-organization properties of stem cells and thus, represent a bottom-up approach in terms of *in vitro* organ modeling, organ-on-a-chip technology employs a top-down approach, *i.e.* an engineered system in which key aspects of the organ's structure and function can be recreated and the microenvironment precisely controlled.[1,15] Both techniques represent two distinct approaches towards the same goal and are currently being explored to be combined synergistically.[15] As organoids often suffer from high variability in size, structure, maturation, and function, researchers hope to enhance reproducibility and physiological relevance by their integration into organ-on-a-chip devices. Potential benefits arise mainly from miniaturization on microfluidic devices, which entails lower reagent consumption as well as laminar flow regimes, and hence allows for enhanced control over soluble and physical aspects of the cellular microenvironment compared to traditional cell culture techniques. Additionally, microfluidics enables multiplexing and automation of cellular assays, thus increasing throughput. Microfluidic approaches to recapitulate human organ physiology *in vitro* as well as the benefits and limitations of state-of-the-art organ-on-chip devices are the focus of the following chapters.

2.2.1 Engineering human physiology

To mimic key aspects of the *in vivo* environment on an organ-on-a-chip device, a fundamental understanding of the native tissues and organs is required. Once key cellular and microenvironment components have been identified, a microfluidic-based device aims to synthesize them in such a way as to promote the development of a model system that is structurally and functionally similar to the *in vivo* organ. This includes for example the co-culture of multiple cell types to emulate the native tissue composition, perfusion of the cell cultures to enhance convective mass transport and thus nutrient and oxygen supply, or to apply mechanical forces such as shear stress on the cells, as well as a defined physical arrangement of the cells to recapitulate morphogen gradients, cell-to-cell, and cell-to-ECM interactions. A broad variety of microfluidic design elements has been proposed so far to achieve an ever-increasing physiological relevance to the *in vitro* system. The following chapters elucidate examples for microenvironmental control as well as tissue interactions on microfluidic chips.

2.2.1.1 Control of the cellular spatial arrangement

Recapitulation of physiological spatial confinements *in vitro* has long been known as an important regulator of various cellular processes such as proliferation, apoptosis, and differentiation at the single-cell level.[78–80] Spatial confinements arise from interactions of individual cells with their neighboring cells, the ECM as well as the nanoscopic features of their surrounding microenvironment.[77] Through individual cells, also whole tissues can sense their boundary conditions and spatially pattern themselves accordingly. Consequently, emulating the whole tissue architecture in model systems and their corresponding physical boundary conditions has been shown to modulate long-term organoid preservation as well as function.[10,81]

Organ-on-a-chip devices aim to recapitulate key hallmarks of the native tissue's architecture by culturing cells in 3D in microfabricated culture compartments which are engineered to provide a spatial arrangement similar to the physiological conditions. This is typically achieved either by allowing cells to **self-aggregate** or by an **extrinsic design** of the microfabricated culture compartment (**Figure 2.2**). To establish and maintain a 3D spatial arrangement of cells by self-aggregation on organs-on-a-chip, often traditional 3D cell culture modalities have been adapted to fit the miniaturized format of microfluidics. In these microfluidic chips, cells are typically introduced as a single cell suspension and trapped by some kind of structure where they eventually aggregate. For example, often an array of microwells[68,82] together with an anti-adhesive coating like bovine serum albumin (BSA) or Pluronic[83] is employed to form and culture cells in 3D (**Figure 2.2A**). Other groups have used U-shaped barriers[83–86] to entrap and perfuse the cell material (**Figure 2.2B**). The underlying trapping principle of the U-shaped barriers, as well as the possibility for retrieval, varies greatly within designs presented in the literature. In fixed structures, the irreversible capture of cells has been reported by asymmetric

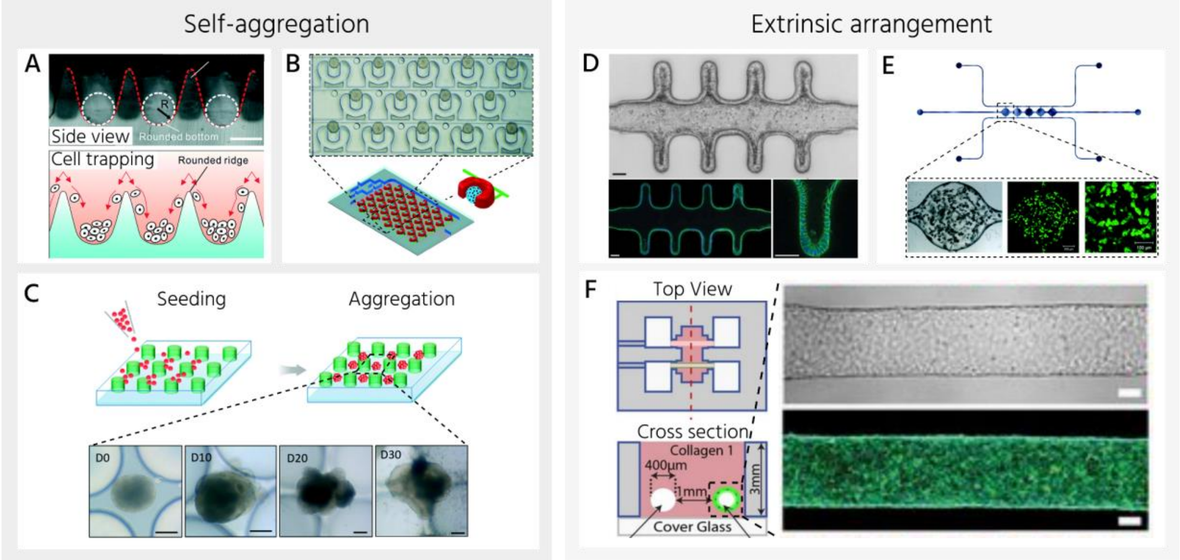

Figure 2.2 Overview of techniques for the control of spatial arrangement of cells on microfluidic chips. (**A**) An anti-adhesive coating ensures formation and maintenance of 3D cell cultures in integrated microwell arrays on-chip. Adapted from Ref.[68] with permission of the Royal Society of Chemistry. (**B**) Pneumatic actuation of the U-shaped barrier to form, culture on, and retrieve cell aggregates off microfluidic chips. Adapted from Ref.[83] with permission of the Royal Society of Chemistry. (**C**) Formation and culture of embryoid bodies in the confined space of an integrated micropillar array. Adapted from Ref.[88] with permission of the Royal Society of Chemistry. (**D**) Tubular hydrogel scaffold containing microcavities mimicking the geometry of native intestinal crypts for the culture of mouse intestinal stem cells. Adapted from Ref.[10] with permission of Nature Research. (**E**) Fibrin hydrogel scaffold for the 3D culture of hASC-derived adipocytes. Adapted from Ref.[52] with permission of the Royal Society of Chemistry. (**F**) Formation of a 3D vessel of endothelial cells in a preformed collagen hydrogel to investigate angiogenic sprouting. Adapted from Ref.[91] with permission of the National Academy of Sciences of the United States of America.

positioning of the barriers within a larger chamber[84,86] or by inclining the whole microfluidic chip and subsequent gravity-assisted sedimentation[87]. In contrast, pneumatically actuated U-shaped barriers reversibly trap cells by dimensional restriction when they pass through the chamber.[16] A somewhat different approach was demonstrated by Wang *et al.*[88], who formed and cultured human iPSC aggregates in the confined space of a micropillar array (**Figure 2.2C**). The authors reported this technique to be beneficial in terms of nutrient supply and waste removal while reducing the shear stress acting on the surface of the 3D cell cultures.

A fundamentally different strategy to spatially arrange cells in 3D on organ-on-chip devices makes use of supporting hydrogel matrices as an extrinsically designed arrangement. Here, cells are either loaded and cultured in a microfluidic network that has been created within the hydrogel matrix[10,89–91] (**Figure 2.2D**, **F**) or directly embedded in an unpolymerized hydrogel, and then the cell-hydrogel mix is loaded into an external microfluidic channel network[52,92,93] (**Figure 2.2E**). The embedding of cells within a hydrogel is mostly applied to cell types that would be hard to culture in 3D otherwise, such as *e.g.* primary adipocytes[94].

2.2.1.2 Control of the biophysical and biochemical cellular microenvironment

In vivo, a myriad of instructive cues stemming from the cellular microenvironment drive organogenesis and morphogenesis. As cells constantly interact with their local microenvironment, researchers hope to guide the self-organization and differentiation capabilities of stem cells, as well as the functionality of derived organ models through precise control of the cellular microenvironment. The latter thereby comprises nutrient availability, the presence or absence of soluble factors, cell-ECM interactions, as well as oxygen tension, and other physical and mechanical cues. Precise control of such microenvironmental conditions and further, dissection of the contribution of individual instructive cues[95] is often limited in conventional cell culture due to their complex and dynamic nature[1] and a high degree of intertwined biochemical and biophysical phenomena[96].

Perfusion. The miniaturization of cell culture processes on microfluidic systems with working volumes typically ranging from tens of nanoliters[22,25,97] to a maximum of a few hundreds of microliters[98,99], ensures a more physiological cell-to-liquid ratio than conventional culture techniques. To still ensure sufficient nutrient supply and removal of waste products secreted by the cells, they are routinely perfused on these systems to exchange the surrounding cultivation media. These dynamic culture conditions have been correlated positively with cell viability[6,68,100], proliferation[101], differentiation capacity[88,100], and functionality[6,68,88]. Depending on the native organ’s environment, cells are either directly[102,103] or indirectly[104,105] perfused and either in a continuous[102,106] or discontinuous fashion, *i.e.* by regularly timed feeding pulses[25]. Vasculature-on-chip models, for example, often directly and constantly perfuse endothelial cells lining a vessel-mimicking lumen structure (see **Figure 2.2F**) to enhance the creation of a cohesive cell sheet as well as alignment of the endothelial cells with the direction of flow similar to the *in vivo* situation.[91,107] Opposed to this, other cell types, such as *e.g.* adipocytes, are only exposed to interstitial flow in physiological conditions and are thus perfused indirectly on microfluidic chips.[104] To achieve indirect microfluidic perfusion, porous membranes[104,105,108,109] or microfabricated protective barriers[16,82,110] have been proposed. Careful consideration needs to be put on the applied continuity and rate of perfusion as excessive perfusion can have detrimental effects on some cell types[16,52,111]. For example, continuous perfusion of ESCs during differentiation towards motor neurons resulted in significantly reduced differentiation efficiency compared to static and discontinuously perfused controls.[102] The authors explain this by perturbation of necessary diffusible cell signaling due to the continuous perfusion.

Soluble factors. The presence of growth factors, cytokines, and nutrients is a key regulatory component of the biochemical microenvironment of cells. Thanks to the highly controllable flow on microfluidic systems, spatially and timely resolved activation of morphogenetic signaling pathways by exogenous soluble factors can be achieved and stem cell differentiation directed.[48,106,112] Integrating microfluidic modules, such as *e.g.* a gradient generator, upstream of the cell culture compartment allows for the delivery of soluble factors at defined concentrations. In a recent study, such a microfluidic gradient generator has been used to recreate patterning aspects of the neural tube development during human embryogenesis.[48]

Extracellular matrix. The ECM is the non-cellular component of every tissue which serves both as structural as well as biochemical support for surrounding cells. It is composed of a mesh-like network of proteins and polysaccharides which is highly specialized for different kinds of tissue within the human body. As it is an important signaling cue for cells, it is frequently modulated in organoid engineering to drive stem cell fate[78,113], morphogenesis[50,54,114], and maturation of organoids[49,115]. For example, the embedding of embryonic and extraembryonic stem cells *in vitro* in a 3D ECM scaffold was sufficient to substitute for the basement membrane normally provided by the primitive endoderm, such that cellular self-assembly produced a structure that mimics the mouse embryo during early development.[114] To provide cells with native ECM-like signaling on organ-on-a-chip devices, several approaches have been exploited: surface patterning of ECM proteins[116], injection and solidification of an ECM-like hydrogel within microfluidic channels[117], or generation of a microfluidic channel network within the hydrogel itself[118] (similar to **Figure 2.2D**).

Oxygen control. Oxygen tension within the cellular microenvironment is a central driver of cell morphology and function. For example, the physiologically occurring oxygen gradient in the liver from the periportal (11-13 % O_2) to the centrilobular (4-5 % O_2) region is crucial for the functional specialization of the parenchyma, the so-called metabolic zonation.[119–121] There have been several attempts to recreate liver zonation on microfluidic chips by establishing and controlling the level of oxygenation during on-chip culture by use of flow-based[120,122] or chemical[123,124] oxygen gradients. A comprehensive review of techniques to precisely manipulate oxygen levels within microfluidic chips is provided by Rivera *et al.*[121].

Mechanical cues. Shear stress, cyclic stretching, compression, ECM stiffness, and other mechanical forces have been shown to impact several cellular processes including proliferation[125,126], intestine crypt formation[12], mesenchymal cell-driven condensation[127], as well as bacteria-gut interaction[128]. Sun *et al.*[129] provide a detailed overview of the effects of mechanical forces in the local cellular microenvironment on stem cells.

2.2.1.3 Control of cellular crosstalk

Human physiology involves the interaction of various kinds of tissues and cells both in close proximity and at periphery sites. Cellular crosstalk is therefore established by different kinds of cell signaling. While paracrine and juxtacrine signaling act locally, endocrine signals are transported via the circulatory system to periphery tissues. For example, in the liver, the expression of the fibroblast growth factor 21 (FGF21) in hepatocytes has been suggested to induce fatty acid uptake and catabolism in a paracrine fashion, while the same signaling molecule also acts in an endocrine manner to stimulate lipolysis in adipose tissue.[130] To emulate these various kinds of cellular cross-talk on organs-on-chips, direct and indirect co-cultures of two or more cell types within one platform, as well as fluidic coupling of individual organ-on-chip units (which are often referred to by the term body-on-a-chip) have been exploited. Body-on-a-chip platforms will not be discussed any further here but have been summarized elsewhere.[131]

To establish a **direct contact** of different cell types and to co-culture them on the same microfluidic platform in 3D, different techniques have been proposed. For example, the group of Hang[132] extended the classical microslit approach – a technique in which single cell aggregates are trapped in microfabricated slits due to a slight hydrodynamic imbalance between the slits and the main channel – to enable the sequential trapping of two spheroids within one location. Thereby, they generated complex multicellular aggregates which resemble patterns of early mouse embryogenesis.[132] Another group also paired two cell aggregates, tumor and stromal spheroids in their case, by transferring pre-formed spheroids onto a microfluidic array-based microwell chip, which already contained one spheroid in each microwell, and centrifugation-aided distribution of them into individual microwells.[133]

To emulate the cellular crosstalk present *in vivo* on an organ-on-a-chip platform, cells do not necessarily need to be in direct contact as they are often rather communicating through the release of **paracrine signals**. For example, the 2D co-culture of endothelial cells and pericytes as a retinal microvasculature model was demonstrated by culturing both cell types on the opposing sides of a microporous membrane.[134] This bilayer design enabled paracrine interaction between the cell types while offering channel and cell type-specific stimuli and analysis. A more versatile approach enabling the modeling of temporal variations in cell signaling was presented by Yu *et al.*[135] who added and removed individual microfluidic layers containing different cell types dynamically on top of each other. Non-dynamic, but rather permanent compartmentalization on organs-on-chip for co-culturing different cell types has also been demonstrated, *e.g.* by the integration of porous barriers[136,137] and membranes.[98,105,134]

2.2.2 Scaling up organ-on-a-chip technology

For the adoption of the organ-on-a-chip technology in an industrial context, developed devices need to allow for mass production and high throughput studies. Unfortunately, these are key limitations of most current organ-on-chips hindering their application in pharmaceutical and biomedical research.[19,20] Addressing this shortcoming, several approaches focusing on fabrication techniques and materials which are commonly used in industry such as injection molding or hot embossing as well as the processing of thermoplastics have been presented in the literature and will be discussed in more detail in the first part of this chapter. The second part will give an overview of microfluidic devices aiming to increase the throughput of *in vitro* organ models through the automation and parallelization of cell culture processes.

2.2.2.1 Mass production

Most organ-on-a-chip platforms are fabricated in **PDMS** due to its optical transparency, gas permeability, and biocompatibility.[138,139] These properties along with its ease of use and inexpensive microfabrication make it an ideal candidate for the development of cell-based microfluidic devices in academic research.[140,141] Despite these prodigious characteristics of PDMS, it has several drawbacks including small hydrophobic molecule absorption[142,143], evaporation of water causing critical changes of osmolarity in the culture medium[144], and labor-intensive fabrication processes impeding large-scale production and therefore commercialization of PDMS-based organ-on-a-chip devices[19,138]. To address the drawbacks of PDMS, other materials and fabrication technologies better suitable for large-scale production, namely injection molding[64,145–148] and hot embossing[139,140], have been exploited. For example, Lohasz *et al.*[145] presented an injection-molded microfluidic device made of polystyrene (PS), a thermoplastic commonly used for traditional laboratory cultureware[149], designed for versatile applications of 3D microtissue cultures. The platform complied with microtiter plate standard formats and did not require any elaborate external equipment for the operation which might facilitate pharmaceutical applications due to easier integration in standardized workflows and classical analytical tools.[20] Another group also investigated injection molding as an alternative fabrication technique for organs-on-chip[147] but used styrene-ethylene-butylene-styrene (SEBS) instead of PS as material. SEBS, a subgroup of thermoplastic elastomers (TPE), has been shown superior to PDMS in terms of processability in commercial mass production[139,150], absorption of drug compounds[147], and absence of toxic crosslinking agents[151] and has been integrated as flexible membranes in microfluidic chips due to its elastic properties similar to PDMS[152,153]. Other methods proposed for upscaling of the fabrication of microfluidic platforms towards mass production include the usage of materials such as poly(methyl methacrylate) (PMMA)[154], reversible attachment of standardized fluid control modules to single-use devices containing the cell material[152,155], and new fabrication techniques like *e.g.* laser micromachining[156,157]. Despite huge efforts, mass production compatible fabrication approaches are not yet widely adopted and the prodigious properties of PDMS still often make it the material of choice when developing new organ-on-a-chip platforms.

2.2.2.2 High throughput

The need for the generation, culture, and analysis of physiologically highly relevant *in vitro* organ models at a large scale for disease modeling, drug screening, or regenerative medicine applications has been highlighted by several studies.[19,158,159] Microfluidic techniques have been proposed to leverage this need for high throughput screening as they offer good reproducibility, automation, and parallelization of cell culture processes.

Enhanced **reproducibility** of organs-on-a-chip in comparison to traditional organoid technology is attributed to the capability of microfluidic systems to provide precise fluidic, mechanical, and structural control over extended periods.[4,158] For example, the generation of a vascularized micro-organ on a microfluidic chip has been shown to be highly reproducible among twelve independently operated devices in terms of vessel area and length.[160] High reproducibility has also been demonstrated for another microfluidic device, where a coefficient of variation of less than 3% for the size of all formed tumor spheroids was reported.[161] Homogeneity of spheroid sizes is a critical prerequisite for the reproducible differentiation of human stem cells as recently highlighted by a study investigating the impact of initial spheroid size on hepatic[73] and intestinal[14] differentiation. Accordingly, organ-on-a-chip models incorporating stem cell-derived 3D cell cultures typically aim for the generation of spheroids with uniform sizes before initiating differentiation.[24,162]

Besides homogeneous starting conditions[14], reproducibility of stem cell differentiation and organoid culture was also demonstrated to increase by the **automation** of the cell culture process.[24,162,163] For the automation of organ-on-chip-related culture processes, different techniques have been proposed.[19] Either the microfluidic setup itself allows for automated manipulation and culture of cells on the chip by the integration of valves and pumps[19,24,164] or external equipment such as liquid handling robots are used to automatize the reagent and cell injection onto and extraction of the chip[14,165]. For the latter, compatibility of the device with existing laboratory equipment and SLAS standards is of critical importance.[99,134] For example, Rogers *et al.*[134] recently presented a retinal microvasculature-on-chip platform consisting of 96 individual arrayed units that are compatible with standard microplate technology. A completely different approach was presented by the group of Ingber, who automated the culture of multiple organs-on-chips by developing a custom-made automation system consisting of a liquid handling robot and an integrated mobile microscope.[165,166] Applying this robotic interrogator, the viability and organ-specific functions of eight vascularized organ chips were successfully maintained for three weeks.[165] Besides enhancing reproducibility, automation of cell culture processes allows for the application of dynamic culture conditions on-chip, which are critical to the maturation[88,167], functionality[101,168], and long-term viability[68,101] of organoids.

By the integration of active components on microfluidic chips, **parallelization** of cell culture tasks and combinatorial assays on a single platform has been achieved. For example, parallel testing of seven drug concentrations on ovarian cancer spheroids was recently demonstrated on a single platform containing eight individual cell culture chambers, which could be addressed in serial or parallel by integrated microfluidic valves.[169] Integration of even more cell culture chambers and thus a higher parallelization degree can be achieved on mLSI chips. These chips have been exploited for the automated generation, maintenance, and analysis of human stem cell cultures at a large scale[24,164,169] and will be reviewed in detail in the next chapter.

Despite the generally good suitability of certain microfluidic technologies for high throughput screening, such as droplet microfluidics[81,170,171] or mLSI[22,164], most organ-on-a-chip devices presented so far remain on the proof-of-principle level due to lacking reliability and reproducibility[4,172], incompatibility with automation[19], and versatility for different kinds of organoid and cell culture studies.[20,173]

2.3 Microfluidic large-scale integration

As presented in the previous chapter, there is a high need for the automation and parallelization of cell culture tasks on microfluidic platforms to be compatible with high throughput applications. One microfluidic technique ideally suited to meet this need is **microfluidic large-scale integration**, which is discussed in the following chapters in detail. The first sections cover basic concepts of pressure-driven microfluidics in general and the mLSI technique in specific. For the sake of a better understanding of pressure-driven microfluidics, fundamental hydrodynamic principles of these systems are briefly presented, before proceeding with the basic concepts of the mLSI technique. Subsequent sections focus on state-of-the-art mLSI platforms and their biological application followed by traditional as well as more recent mLSI chip fabrication techniques.

2.3.1 Hydrodynamic principles of pressure-driven microfluidics

Microfluidic technology refers to the manipulation of fluids at the microscopic scale within an engineered system.[21] These fluids typically flow in a network of one or more microchannels inside the engineered system. Their flow behavior is governed by physical principles which often apprear unintuitive when compared to flow in macroscopic systems. This is primarily due to the miniaturization, as the reduction of the scale to micrometers leads to the domination of viscous and surface forces compared to the dominant inertial and volumetric forces in macroscopic fluid dynamics.[174,175] An important property of the fluids handled on microfluidic platforms, which are typically some kind of aqueous solution, is their **viscosity**. The viscosity of a fluid describes its resistance to deformation by shear or tensile stress and can be described by ‘Stokes’ Law’.[175] According to Isaac Newton, the resulting viscous forces are then calculated by the differential equation (2.1):

$$\tau = \mu \frac{\partial u}{\partial y} \tag{2.1}$$

where τ is the shear stress, μ the dynamic viscosity, and ${}^{\partial u}/_{\partial y}$ the shear rate. Fluids that have a constant viscosity and behave according to Newton’s law, are called **Newtonian fluids** and represent an important class of fluids in microfluidics. To describe their motion inside a microfluidic channel, hydrodynamic equations for a continuous medium are formulated based on the assumption that a fluid particle is much smaller than the size of the system (continuum hypothesis)[175], including three basic conservation principles: the conservation of mass, energy, and momentum.[174] The hydrodynamic equations representing these conservations laws are often referred to by the term **Navier-Stokes** equations, although strictly speaking this term only applies to the conservation of momentum equation.[174] Since microfluidic systems without temperature gradients are the focus of this thesis, the equation for the conservation of energy will be neglected here, but can be found in the literature.[174] For an incompressible (*i.e.* with a constant density over space and time), Newtonian fluid the partial differential equations (2.2) and (2.3) are used to describe the motion of viscous fluids inside a microfluidic system:

Conservation of mass
$$\nabla \cdot \boldsymbol{u} = 0 \tag{2.2}$$

Conservation of momentum
$$\rho\left(\frac{\partial \boldsymbol{u}}{\partial t} + (\boldsymbol{u} \cdot \nabla)\, \boldsymbol{u}\right) = -\nabla p + \mu \nabla^2 \boldsymbol{u} + \boldsymbol{f} \tag{2.3}$$

where $\boldsymbol{u}$ is the fluid velocity field, ρ is its density, p the pressure field, and $\boldsymbol{f}$ an external acceleration field due to gravity for example. The two terms on the left-hand side in equation (2.3) represent forces due to inertia, while the terms on the right-hand side summarize pressure, viscous, and external forces from left to right. For reasons of easier analysis, the Navier-Stokes equations are often converted to a non-dimensional form. This allows assessing the importance of individual terms in the equation for the studied flow based on dimensionless numbers such as the **Reynolds number (Re)**. This number gives the ratio of inertial forces to viscous forces and can be obtained by equation (2.4):

$$Re = \frac{\rho u L}{\mu} \tag{2.4}$$

where u is the typical velocity of the fluid and L is the characteristic length of the geometry. Since inertial forces are the cause for creating turbulence, flow regimes with high Re (> 2300) are called turbulent flow. On the opposite, at low Re, the flow is governed by viscous forces which are intrinsically regular leading to a **laminar flow** regime. This kind of flow is typically present in microfluidic channels, as miniaturization decreases the characteristic length and velocity and thus, favors low Reynolds numbers.

To move a Newtonian fluid, which is incompressible and viscous, through a cylindrical microfluidic channel of length L and radius $R \ll L$ (**Figure 2.3A**), many systems employ a pressure gradient between the inlet and outlet of the channel to generate a laminar flow of this fluid, the **Poiseuille flow**. To describe this kind of flow, the Navier-Stokes equation is applied assuming fully developed flow, a unidirectional velocity field, and no acceleration.[176] This leads to a simplification of equation (2.3) as all inertial terms and the external force term are zero (2.5):

$$0 = -\nabla p + \mu \nabla^2 \boldsymbol{u} \tag{2.5}$$

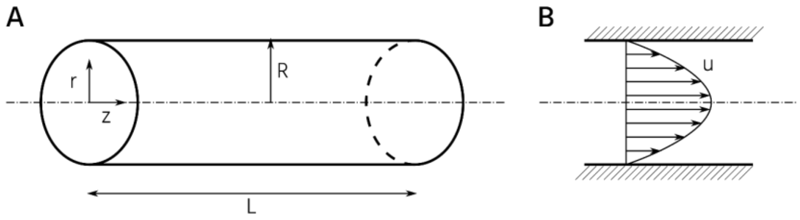

Figure 2.3 Poiseuille flow in a cylindrical microfluidic channel. (**A**) Channel geometry with important axis and parameters. (**B**) Axial velocity profile inside the channel.

Solving equation (2.5) for no-slip boundary conditions ($u = 0$ at $r = R$) and axisymmetric flow yields a parabolic velocity profile (**Figure 2.3B**) across the diameter of the channel (2.6):[176]

$$u(r) = \frac{1}{4\mu}\left(-\frac{dp}{dz}\right)(R^2 - r^2) \tag{2.6}$$

where $-dp/dz$ denotes the axial pressure gradient. Integration of the velocity over the channel's cross-section gives the volumetric flow rate Q (2.7):

$$Q = \int_0^R 2\pi r\, u(r)\, dr = \frac{\pi R^4}{8\mu}\left(-\frac{dp}{dz}\right) \tag{2.7}$$

Assuming that the pressure gradient along the microfluidic channel is uniform, the term $-dp/dz$ can be approximated to be $\Delta p/L$, where Δp denotes the pressure difference along a finite channel of length L. Combining this with a rearrangement of equation (2.7) yields the **Hagen-Poiseuille's law** (2.8):

$$\Delta p = Q \cdot R_H \tag{2.8}$$

where R_H denotes the **hydraulic resistance** and is defined as $R_H = \frac{8\mu L}{\pi R^4}$ for a cylindrical channel. The hydraulic resistances of microfluidic channels of other cross-sections have been summarized elsewhere.[175,176] Hagen-Poiseuille's law is the hydraulic equivalent to Ohm's law in electric circuits, facilitating the design and analysis of pressure-driven microfluidic networks by use of the hydraulic-electric circuit analogy.[176] Similarly to electric circuits, serial and parallel combinations of N microchannels with hydraulic resistances $R_{H,1}$ to $R_{H,N}$ is equivalent to a single microchannel with a fluidic resistance according to equations (2.9) and (2.10):

Serial arrangement $$R_{H,eq} = R_{H,1} + R_{H,2} + \cdots + R_{H,N} \tag{2.9}$$

Parallel arrangement
$$\frac{1}{R_{H,eq}} = \frac{1}{R_{H,1}} + \frac{1}{R_{H,2}} + \cdots + \frac{1}{R_{H,N}} \tag{2.10}$$

To enable precise fluid routing on microfluidic chips, the arrangement of microchannels with different lengths and dimensions within the fluidic network is based on differential hydraulic resistances as fluids preferentially take the path of least resistance.

2.3.2 Basic units of microfluidic large-scale integration

The core part of microfluidic large-scale integration technology are **pneumatic membrane valves** (**PMVs**).[21] mLSI platforms typically integrate hundreds to thousands of these valves on a single platform to facilitate precise fluid routing and massive parallelization on these devices.[177] A single PMV consists of two orthogonally intersecting microchannels separated by a thin, flexible membrane (**Figure 2.4A**). Cellular material, chemical reagents, and other fluids are handled in the half-rounded flow channel, while the other, the control channel, is a dead-end channel and only used to manipulate the flow in the channel above or below it. Depending on the positioning of the control channel relative to the flow channel, two configurations of PMVs can be discriminated: push-down and push-up (**Figure 2.4B**). In both configurations, the valve is normally open, *i.e.* in the resting state, the flow can pass the valve without obstruction (corresponding to the binary state 0). Contrarily, pneumatic actuation of the valve by pressurization of the dead-end control channel causes the thin membrane to deflect into the flow channel where the flow is subsequently constricted and eventually, for high enough pressures, fully stopped. The PMV is then considered fully closed (corresponding to the binary state 1). To reach this state, a half-rounded flow channel profile is required. For a rectangular profile, the flow channel can never be fully sealed despite high control pressures, and the valve is thus considered a sieve valve. Due to the uniform membrane thickness of push-up valves, this configuration requires lower actuation pressures to be fully closed than a push-

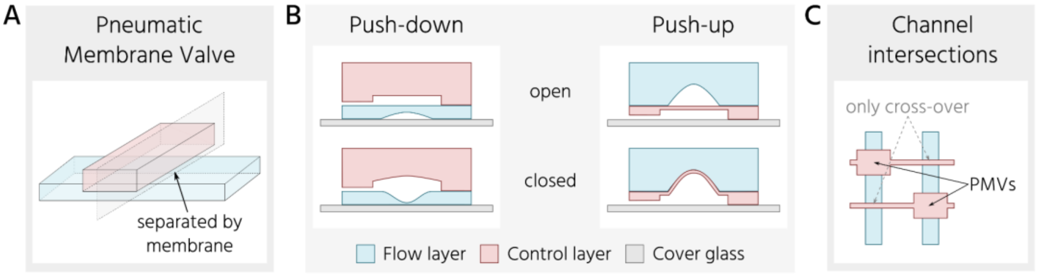

Figure 2.4 Characteristics of pneumatic membrane valves (PMVs). (**A**) Two orthogonally intersecting channels separated by a thin membrane form a PMV. (**B**) Depending whether the control channel runs above or below the fluidic channel, PMVs are configured in push-down or push-up configuration, respectively. PMVs are normally-open valves. Upon actuation of the control channel, the thin membrane deflects and seals the half-rounded channel in the flow layer, *i.e.* the valve is closed. (**C**) PMV formation is geometry-dependent, thus, valves are only formed where wider sections of a control channel intersect a flow channel. At small control line widths, control channels simply pass over fluidic channels.

down valve of a similar dimension.[21,178] This kind of valve has first been introduced by the Quake lab in 2000 offering a reduction in size by more than two orders compared to microfluidic chips incorporating other valve designs.[33] Other common designs based on pneumatic actuation include plunger valves[179], seat valves[180,181], and vertical membrane valves[182]. However, the smaller footprint of "Quake-style" valves compared to other designs offers dense integration of these on mLSI platforms.[183,184]

The logical combination of several PMVs in series or parallel can generate pumps, mixers, and multiplexers offering integration of higher-level components on-chip.[21] For example, a linear array of three valves along a flow channel and their respective actuation in a peristaltic sequence act as an on-chip pump.[21,183] An integrated peristaltic pump has been shown to allow precise metering of volumes as small as 80 pL on microfluidic platforms.[185] Another powerful higher-level component of mLSI chips is **multiplexers** which allow complex fluid handling functionality with a minimum number of control inputs.[186] For this, a single control channel intersects several fluidic channels forming PMVs at each intersection of sufficient footprint (**Figure 2.4C**). Such a serial array of PMVs can then be operated simultaneously, *i.e.* opening and closing all valves along the control channel at the same time. Independent pressurization of other control channels allows for addressing large numbers of PMVs with few external control inputs. The logical combination of independently operable control channels and a network of parallel flow channels allows for directing fluid flow through a single channel by opening all PMVs along this flow channel while any other is closed by at least one PMV (**Figure 2.5**). Such multiplexing structures have been employed for the individual addressability of thousands of chemically independent cell culture compartments with only a few tens of control channels, thus, enabling efficient parallelization of different cell culture tasks on a single chip.[22,186] For example, Thorsen *et al.*[186] demonstrated the use of a binary multiplexer (**Figure 2.5**, left side) comprising only 20 independent control channels for the actuation of > 3000 PMVs and thereby uniquely addressed 1024 separate compartments. In this kind of multiplexing structure, the number of control lines (N) scales with $k = 2^{N/2}$ for

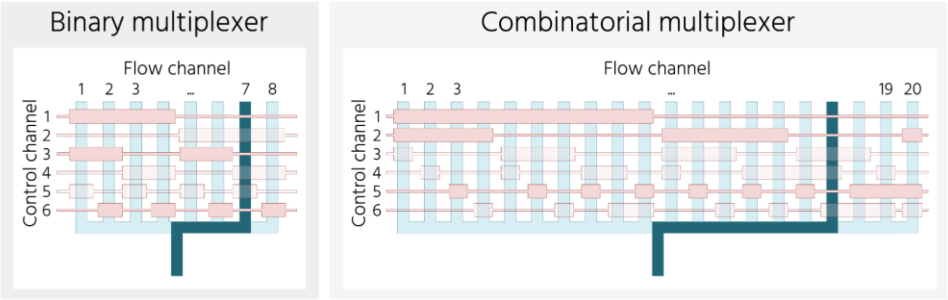

Figure 2.5 Multiplexing logics on mLSI platforms. A multiplexing structure consists of a complex network of PMVs, which are operated by only a few control channels (here $N = 6$) but can manipulate fluid flow in far more flow channels (k). For the **binary** layout the number of addressable flow channels scales by $2^{N/2}$ (here $k = 8$), for the **combinatorial** layout by $N!/[(N/2)!]^2$ (here $k = 20$). For both logics, pneumatic actuation of a subset of control channels (here 3/6) seals the flow in all fluidic channels except for one (highlighted in dark blue color). Here, all PMVs are open and the fluid is free to pass.

the number of independently addressable chambers (k). Hua *et al.*[180] proposed an even more efficient multiplexing algorithm, where the scaling ratio is $k = N!/[(N/2)!]^2$. A so-called combinatorial multiplexer (**Figure 2.5**, right side) yields, for example, 12 870 individual compartments for 16 control channels, whereas the former, binary multiplexer can only address 256. This also highlights the suitability of mLSI platforms for high-throughput studies, which will be reviewed in the following chapter.

2.3.3 Examples of mLSI chips for stem cell culture studies

The use of integrated valves on-chip enables automation and massive parallelization of cell culture processes and analytical protocols on mLSI platforms. Presented applications in the literature include stem cell differentiation[22–25,187], cell-to-cell communication studies[26], cell transfection[188], conditional transcriptomics[189], biomarker detection[27,28], and drug screening[29,30]. For example, Gómez-Sjöberg *et al.*[187] demonstrated the usage of an mLSI platform with 96 independently addressable culture chambers for the fully automated culture of human primary MSCs and investigation of transient stimulation schedules on osteogenic differentiation (**Figure 2.6A**). In their study, an integrated multiplexer was used to expose human MSCs to time-varying osteogenic stimuli. Based on the expression of alkaline phosphatase, a marker for osteogenesis, the group concluded that a minimum stimulation duration of four days is necessary for the full commitment of MSCs toward the osteogenic lineage. Another group had differentiated human adipose-derived stem cells (hASCs) into adipocytes in 128 separate cell culture compartments on an mLSI chip to unravel the regulatory function and signaling network of the kinase complex mTORC1, which was shown to regulate energy balance, in adipogenesis (**Figure 2.6B**).[23] After optimization of the feeding pulse frequency, on-chip adipogenic differentiation of hASCs yielded more homogeneous results in terms of lipid accumulation than traditional well plate-based experiments. A similar observation has been noted by Vollertsen *et al.*[25], who stated a two-fold increase in cardiac mesoderm differentiation of ESCs maintained on an mLSI platform compared to off-chip controls. Their platform contained 64 parallel cell culture chambers and a combinatorial multiplexer to spatiotemporally isolate the chambers and automate medium exchange. While these devices highlighted the feasibility of automation and parallelization of cell culture tasks for the standardization of the differentiation of various kinds of human stem cells, their throughput is rather low compared to the 1500 separate culture compartments recently presented by Zhang *et al.*[22] in their platform (**Figure 2.6C**). The group developed a complex network of fluidic channels and culture chambers to investigate the role of temporal and combinatorial application of six regulatory molecules on the differentiation of mouse embryonic neural stem cells in an ultra-multiplexed manner. For this, hydrogel-based spheres of neural stem cells were cultured in independently programmable two-layer cell chambers by diffusion- or flow-based medium delivery. The special two-layered design of the culture chambers rendered the platform more versatile, also facilitating single-cell studies as well as adherent 2D monolayer and non-adherent suspension cultures. Despite this versatility, this as well as the previously presented platforms are developed for the detailed analysis of individual cell dynamics rather than for the culture and screening of whole 3D cell aggregates in a high throughput manner. Fundamental as well as biomedical and pharmaceutical research, however, is moving towards widespread implementation of 3D cell cultures as these better recapitulate organ physiology than 2D cell models.[5,32] To address this technological shift, our group previously presented mLSI-based

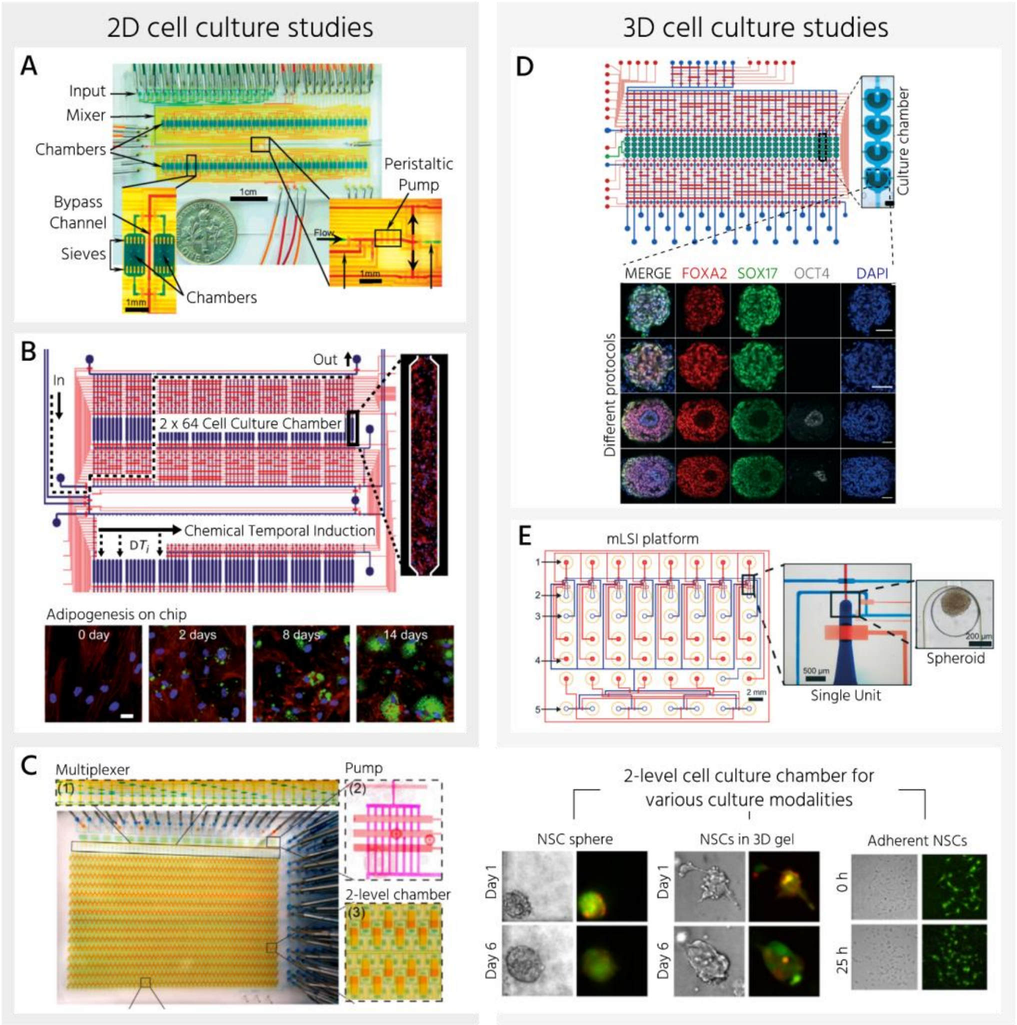

Figure 2.6 Examples of mLSI platforms for 2D and 3D cell culture studies. (**A**) Fully automated culture and differentiation of human MSCs in 96 independently addressable culture chambers to investige the minimum time of osteogenic stimulation required for stem cell lineage specification. Adapted with permission from Ref.[187]. Copyright 2007 American Chemical Society. (**B**) Standardization of adipogenic differentiation of hASC monolayers on an mLSI platform comprising 128 individual culture chambers to unravel the regulatory function of the kinase complex mTOR. Adapted from Ref.[23] with permission of the National Academy of Sciences of the United States of America. (**C**) Ultra-multiplexed microfluidic platform to unravel the role of sequential and combinatorial addition of differentiation regulatory molecules to the culture medium on neural stem cell (NSC) fate decisions. Adapted from Ref.[22] under the terms of the CC BY-NC 4.0 license. (**D**) Automated culture and differentiation of human iPSCs in 3D towards the definitive endoderm lineage to comprehensively compare differentiation yields of different induction protocols. Adapted from Ref.[24] with permission of the Royal Society of Chemistry. (**E**) Analysis of human ASC spheroids on a mLSI chip by whole-mount imaging after osmotic flow-assisted tissue clearing and automation of immunofluorescence staining. Adapted from Ref.[32] with permission of the Royal Society of Chemistry.

platforms for the automated optimization of the endoderm differentiation of human iPSCs[24] and processing of spheroids for whole-mount imaging including tissue fixation, clearing, and immunofluorescent staining[32]. By the integration of U-shaped pneumatic barriers similar to the ones presented by Liu *et al.*[16] into an mLSI platform, 128 iPSC spheroids in 32 independently addressable chambers have been subjected to different differentiation cocktails to comprehensively compare definitive endoderm commitment yields of different protocols (**Figure 2.6D**).[24] To assess the differentiation yield, spheroids were optically cleared and analyzed by whole-mount immunofluorescent imaging on-chip after three days of culture with a slightly modified analytical procedure of the approach presented by Santisteban *et al.*[32], who had used a completely different platform for their study (**Figure 2.6E**). While both platforms proved beneficial either in terms of parallelization[24] or accessability[32] of the 3D cell cultures compared to other microfluidic chips, an mLSI-based approach combining these two features is still missing in the literature. A possible explanation for this is a dimensional incompatibility of 3D cell cultures and microfluidic channels due to limitations in the traditional fabrication processes of mLSI platforms.

2.3.4 Fabrication of mLSI chips

Most mLSI chips are fabricated by stacking multiple individual layers on top of each other with at least one of them made of an elastic or thermoelastic material to ensure sufficient flexibility of the PMV membrane and thus, proper valve functionality. Typically, these individual layers are made of PDMS, an elastomer that can be easily patterned by simply replica molding a negative of the microfluidic channel network. Since such negative molds are commonly produced by photolithography, the process to fabricate mLSI chips from multiple PDMS layers is often referred to by the term **multilayer soft lithography**, which will be elaborated on in the first section of this chapter. Nevertheless, other manufacturing techniques for the production of PDMS molds and mLSI chips have been proposed, which will be highlighted in the following section.

2.3.4.1 Multilayer soft lithography

Multilayer soft lithography with PDMS evolved as the preferred fabrication technology for mLSI chips due to the many attractive physical and chemical properties of PDMS, its ease of use, and low cost.[149,178] Soft lithography comprises two main processes: 1) the fabrication of master molds by micromachining methods, and 2) replica molding of these by casting PDMS (**Figure 2.7**). Since mLSI chips typically consist of three or more PDMS layers, separately cast layers need to be manually aligned on top of each other and then irreversibly bonded in a third step to ensure leak-tight operation of the devices.[33] Final sealing of the device is typically achieved by bonding the device to a cover glass using similar methods as for multiple PDMS layers such as oxygen plasma or off-ratio bonding.[190]

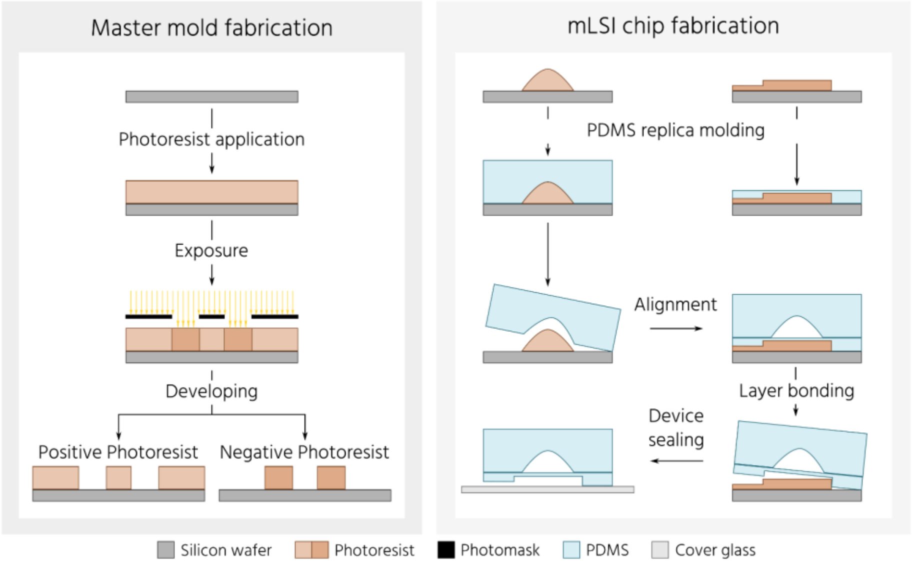

Figure 2.7 Fabrication of mLSI chips by multilayer soft lithography. First, master molds of the fluidic and control circuit are fabricated by photolithograpic micropatterning of a positive and negative photoresist, respectively, on silicon wafers. Subsequently, these are used for casting separate chip layers with PDMS. After alignment and bonding of the layers, the mLSI device is finally sealed by bonding of the multilayer structure to a cover glass.

A replica mold is commonly produced by photolithographic patterning of a photoresist on a silicon wafer. In microfluidics, the most commonly used resist is the **negative photoresist** SU-8. The resist is first deposited homogeneously on the wafer, typically by spin coating, and then exposed to UV through a photomask. Regions that have not been exposed to light can then be simply dissolved by the developing agent in a subsequent washing step, leaving only an extruding pattern of rectangular microchannels on the wafer. PMVs on mLSI chips, however, require a half-rounded cross-sectional shape to guarantee full sealing of the flow channel upon valve actuation. This geometry can be achieved by using a **positive photoresist** (*e.g.* AZ 40 XT or SPR 220) instead of SU-8 as these melt and reflow at elevated temperatures[178], and thus, cause rounding of the initially rectangular microchannels when heating the photolithographic patterning in a post-processing step. Despite this beneficial property of positive photoresists, they are associated with limitations regarding the chemical and thermal stabilities, thereby restricting achievable flow channel heights on mLSI chips to a maximum of a few tens of micrometers in traditional processes.[34,191,192] These sizes are, however, incompatible with 3D cell cultures, whose dimensions typically vary between 50 and 500 µm[13,14,31,73], and thus, hinder the application of the mLSI technique for such studies. To address this limitation, modifications of the traditional photolithography protocol, as well as completely different techniques, have been proposed for the fabrication of rounded flow channels on mLSI chips. These will be reviewed in the following chapter.

2.3.4.2 Other fabrication approaches to achieve half-rounded flow channels

In the literature, different approaches for the fabrication of half-rounded flow channels which are required for the operation of PMVs have been proposed. Since photolithography typically produces rectangular channel geometries and reflow is only amenable to positive photoresists, various modifications of the soft lithography technique presented in the last chapter have been suggested. One such approach is to fabricate a master mold with rectangular channels and then spin-coat a thin film of the same photoresist onto to structure[34,193] such that capillary forces retain the liquid photoresist in the sharp corners between the wafer and the vertical sidewalls of the microchannels. Once the typical process steps of photolithographic patterning including soft bake, exposure, and post bake, are repeated, the spin-coated secondary structure adheres to the original master attaining a widened and rounded channel shape. The process, however, is highly dependent on the location of the microchannels on the wafer, thus, limiting design freedom. To resolve the undesirable widening of the channels, Park *et al.*[194] suggested first producing a microfluidic chip comprising PMVs with solely rectangular flow channels and subsequently adjusting their cross-section *in situ* by local polymerization of a photocurable polymer to achieve full closure of the valve. For this, the group had fabricated a control and flow master mold, both by following standard SU-8 photolithography. After PDMS replica molding, alignment, and plasma bonding of the individual layers, the flow channel was filled with a photocurable prepolymer. Deflection of the valve membrane into the flow channel caused the displacement of the prepolymer into the corners of the channel, where it was exposed to UV light to create a polymeric seal embedded in the channel. Washing out the residual uncured prepolymer resulted in a locally hemicylindrical cross-section of the flow channel at the PMV site. Despite the good sealing properties of the valve, the method is too laborious for mLSI chips incorporating hundreds to thousands of PMVs. The group of Richter proposed using diffusive backside exposure to directly produce rounded channels from negative photoresists.[191] Instead of exposing the photoresist from the top as in traditional photolithography, the UV light source is located at the backside of the wafer, which is made of glass instead of the traditional silicon wafer such that the photoresist can be exposed through it.[34] Diffusive light, compared to collimated light, produces a sloping intensity profile from the middle of the aperture towards the edges[191] resulting in rounded rather than vertical sidewalls of the microchannels. While this technique provides a rather simple approach for fabricating rounded flow channels of different heights, it has only been applied for flow channel heights below 50 µm, which is commonly sufficient for microfluidic 2D cell culture applications but remains to be investigated for 3D cell culture dimensions. In contrast, up to 220 µm, high flow channels with a half-rounded cross-section have been produced by a fabrication method utilizing the deflection of an elastomeric membrane (DEM).[192] For this technique, first a DEM mold consisting of a thin PDMS membrane irreversibly attached to a core block of PDMS with a small channel underneath the membrane is fabricated by standard soft lithography and then passivated to prevent adhesion of uncured PDMS to the DEM mold. Pressurization of the small channel on the DEM mold causes bulging of the membrane, forming an extruding rounded feature on its surface. Upon PDMS casting, these features are imprinted as half-rounded channels into the PDMS layer. The final channel height highly depends on the width of the mold channel (if the same inflation pressure is applied), thus enabling the fabrication of multi-height flow layers simply by varying the channel widths on the DEM mold. This is a major advantage compared to traditional photolithography-based mLSI chip fabrication, which requires separate molds or cumbersome secondary patterning processes to achieve different flow channel heights. When compared to other techniques for achieving rounded microchannels in PDMS, as done so by Bartlett *et al.*[34], DEM molds were laborious to fabricate and prone to frequent failure. In contrast, 3D printing of master molds[37,195,196] proved to be extremely simple and versatile in their study. Flow channels of slightly larger sizes than in traditional MSL, but still reasonable for microfluidic applications, with well-rounded cross-sections were successfully produced from a variety of 3D printers.[34] Since this fabrication technique offers great potential for the rapid prototyping of microfluidic chips as well as rendering the mLSI technique compatible with 3D cell culture applications, it is reviewed in more detail in the next chapter.

2.4 3D printing

3D printing, also referred to as **additive manufacturing**, comprises different techniques, which enable the construction of a 3D structure by sequential deposition of material in a layer-by-layer fashion. It offers high design flexibility, the creation of truly 3D fluidic circuits, and rapid prototyping, and thus, has gained great attention in recent years as an alternative to photolithography-based fabrication of microfluidic chips.[45,197] For example, it has been exploited for the fabrication of replica molds for non-planar microchannels[36–38], micro-to-macro interfaces simplifying microfluidic input and output[39,198], PMVs and integrated peristaltic pumps[183,199], and whole microfluidic chips for cell culture applications[43,44,200,201]. Within 3D printing, various techniques with inherently different 3D construction processes and material choices exist, with the most important ones in the field of microfluidics being fused deposition modeling, photopolymer inkjet printing, and stereolithography.[202] Their respective working principles, strengths, and limitations will be discussed in the first section of this chapter before moving on to the application of additive manufacturing for the fabrication of PDMS replica molds as well as directly 3D-printed microfluidic chips in the following chapters.

2.4.1 Techniques

The selection of a specific 3D printing technique heavily relies on the required resolution and material properties of the device to be produced as each technique allows the processing of only a certain set of materials and possesses inherent strengths and weaknesses. In contrast, the general workflow is irrespective of the chosen 3D printing method. The process starts with the design of a digital 3D object within a computer-aided design (CAD) software, which is subsequently sliced into single 2D layers which are then used to construct the physical object in an additive manner depending on the selected technique. A concise overview of the different techniques is given here with a more elaborate discussion to be found elsewhere.[45,203,204]

Fused deposition modeling (FDM). In FDM a thermoplastic filament is extruded through a heated nozzle, which is moved through a motorized stage to continuously deposit the molten material onto the substrate, where it spontaneously cools down and hardens (**Figure 2.8**, left side). By now, a variety of biocompatible thermoplastics such as acrylonitrile butadiene styrene (ABS)[205,206], poly-lactic acid (PLA)[201,207], and polyurethane (TPU)[208] have been printed by FDM. The processability of these materials is a major advantage of FDM, as mass production techniques also commonly use thermoplastic materials, thus fostering the translation of FDM-based prototypes into industrial-scale labware.[209] While further benefits of FDM 3D printing include its robustness, accessibility, low cost, and possibility to integrate multiple materials in a single print to create advanced microfluidic devices, the technique has been associated with poor dimensional accuracy, high surface roughness, and low structural strength.[204,209] The immediate hardening of the extruded material causes poor fusion between adjacent layers and thus, poor structural integrity and even porosity of the printed structure. Especially, the rather large dimensions of a single deposited strand in microfluidic standards lead to the inferior resolution of FDM printers compared to other additive manufacturing techniques.[202]

Photopolymer inkjet printing (PJ). In this 3D printing technique, an inkjet printhead is used to deposit a layer of a photosensitive polymer by ejecting small droplets of it through hundreds of nozzles onto the substrate (**Figure 2.8**, middle). The layer is subsequently cured by UV exposure and the process is repeated to produce a 3D object in a layer-by-layer fashion. Typically, the printhead ejects two different materials, the build, and the sacrificial support material, simultaneously. The support material is required to deposit the build material on top of voids or overhang structures and is removed in a post-processing step. This kind of 3D printing technology is often also referred to as **poly** or **multi-jet modeling** (PJM/MJM) with the two techniques varying in the kind of material used as a support structure. While PJM uses a support material based on water-soluble poly(ethylene glycol) (PEG), MJM is based on paraffin wax that can be removed by heating. The build resin is typically based on acrylate with monomers, oligomers, and a photoinitiator as additives. A notable advantage of photopolymer inkjet printing is the possibility of multi-material printing by using multiple inkjet printheads. For example, Keating *et al*.[210] employed a multi-material printing approach to building a microfluidic valve made of a flexible membrane and a rigid external valve structure within a single print. Besides this major benefit, the technique's low surface roughness[37], large build size[202], and availability of many materials with different physical and chemical properties make it attractive for microfluidic device fabrication. Despite some materials being evaluated as biocompatible[211,212], this classification is currently still under debate as studies have

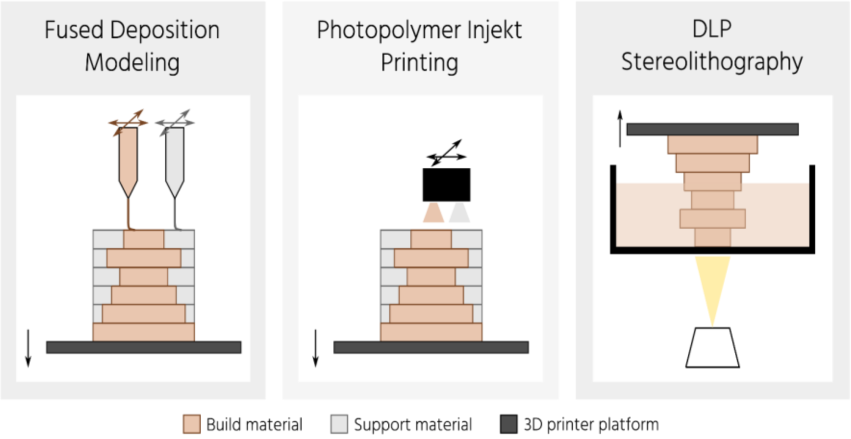

Figure 2.8 3D Printing technologies. In **fused deposition modeling** (FDM), consecutive layers of the 3D object are constructed by lateral movement of heated nozzles which simultaneously extrude the build and support material and downward movement of the 3D printer platform by a preset distance (= layer thickness). In **photopolymer inkjet prining** (PJ), hundreds of nozzles in the inkjet printhead (black box) deposit small droplets of the build and support material onto the substrate to build a 3D structure in a layer-by-layer fashion. In **DLP stereolithography** (SL), a 3D object is generated upside-down by repetitive UV light exposure (yellow triangle) of thin layers of a liquid, photocurable resin at the bottom of the resin reservoir and subsequent upward movement of the 3D printer platform by one layer thickness.

highlighted significantly reduced survival of zebrafish embryos when in contact with 3D-printed specimens[206,213] and require further rigorous investigation[45]. Additionally, the requirement for sacrificial support material in PJ is one of the key drawbacks of the technique for microfluidic applications, since its removal is difficult if not impossible for narrow and enclosed channels.

Stereolithography (SL/SLA). In SL, a moveable substrate is immersed in a tank of liquid, photosensitive resin. A light source focuses on a local region within the liquid and induces spatially controlled photo-polymerization of the material. By changing the focus region of the light source by a predefined distance and repeating the UV light exposure of the photoresin, a 3D object is constructed in a point-by-point or layer-by-layer fashion, depending on the type of the light source. In laser scanning SL, the light source is a single-point laser tracing a 2D cross-section pixel-by-pixel onto the substrate before lowering the substrate to polymerize the next layer, whereas in **digital light processing (DLP)** SL a digital micromirror-array device (DMD) is used as a light source to polymerize all pixels of a layer simultaneously. In the latter, also called ‘constrained’ setup, the layer is typically illuminated through the transparent bottom of the tank with the movable substrate suspended above the liquid reservoir (**Figure 2.8**, right side). Hence, the object is hanging upside down from the substrate during 3D printing. This setup has several advantages compared to constructing the object normally by moving the substrate further into the reservoir with each layer as seen in traditional SL machines: i) there is no need for an extra process step leveling the surface of the liquid to ensure the uniform height of the next layer to be cured as gravity smoothes the surface in the constrained setup; ii) the height of the object to be printed is not restricted by the depth of the resin reservoir; iii) a minimum amount of resin is required as the object is pulled out of the reservoir instead of being immersed in it.[209] The main disadvantages of this configuration comprise the necessity for a highly clean bottom substrate of the tank which is strongly negatively correlated with usage and the possible deformation and destruction of the tank bottom or the object due to strong adhesion between the cured layer and the substrate of the tank. To reduce this risk, the tank bottom is often specially treated to minimize adhesion.[214] After 3D printing, the object typically requires thorough cleaning using alcohols such as ethanol or isopropanol to remove the residual uncured resin.

Similar to PJ, materials for this kind of 3D printing need to be photocurable and are often based on acrylates and epoxides.[204] While there are many materials for DLP printing commercially available, their exact composition including their additives is often proprietary knowledge of the manufacturers hindering their usage in biological applications due to unknown material properties such as biocompatibility or solvent compatibility.[206,215] Additionally, there have been several research efforts to develop custom-made printing resins featuring favorable material properties such as high resolution, similar flexibility to PDMS, good transparency, biocompatibility, and reduced small molecule absorption.[35,44,216] Compared to FDM and PJ, DLP printing showed the highest printing resolution and lowest surface roughness.[34,202] The lateral and vertical resolution of state-of-the-art DLP printers is usually in the range of 5-50 µm and is highly dependent on various factors including the pixel grid of the DMD, the viscosity of the resin, and light-absorbing additives.[204,209] Open microfluidic channels in various materials with diameters below 100 µm have been fabricated by DLP[44,217], whereas the minimum diameter of intruding channels in FDM and PJ typically ranges around 200-300 µm.[202] Even higher resolution than in SL is generally attainable by using a 3D-printing technique based on two-photon polymerization.[218] However, there is a general trade-off between printing resolution (and thus, fabrication time) and overall build size. For microfluidic applications, most desktop SL 3D printers provide a suitable compromise between fabrication cost and time, resolution, and maximum object size.

2.4.2 3D printing-based fabrication approaches for microfluidic chips

Exploiting additive manufacturing for the fabrication of microfluidic chips can generally be divided into two subcategories, both of which will be reviewed in the subsections of this chapter. In the first part, examples of 3D printed master molds and subsequent usage of these for PDMS replica molding are presented. Additionally, the advantages and limitations of this approach are discussed. The second part gives a short overview of directly printed microfluidic chips and reviews their suitability for organ-on-a-chip applications.

2.4.2.1 Master mold fabrication

The additive manufacturing of soft lithography molds provides an attractive fabrication approach for organ-on-a-chip platforms as 3D printing annihilates some of the limitations of photolithography-based micromachining without compromising the prodigious properties of PDMS, such as gas permeability, biocompatibility, and flexibility. For example, master molds comprising microchannels of multiple heights[195,196] and different cross-sectional geometry[37] are easily produced by 3D printing. Comina *et al.*[196], for example, reported the fabrication of PDMS-based lab-on-a-chip devices by using 3D-printed templates (**Figure 2.9A**). Based on the DLP technique, the group successfully produced microfluidic chips integrating different structural elements such as chaotic mixers and multilevel microfluidic channels. In recent years, a growing number of publications reported the use of 3D printed templates for the fabrication of *e.g.* a microfluidic gradient generator[197], PMVs with a single molding step[219,220], capillary circuits enabling autonomous liquid delivery on-chip[221] (**Figure 2.9B**), and a lung-on-a-chip platform[222]. Despite the increasing use of 3D-printed replica molds, many studies reported inhibition of PDMS curing at the surface of the mold, especially when SL was used[196,197], which could only be prevented by tedious post-processing of the mold before casting PDMS (**Figure 2.9C**).[219,223] Phosphine oxide-based photo-initiators leaching out of the bulk material and interacting with the platinum-based PDMS catalyst have recently been identified as the cause of the curing inhibition.[223] Until then uncrosslinked monomers were believed to be the reason why uncured PDMS remained at the PDMS-3D-print interface.[197] Instead, these were found to cause strong adhesion of the PDMS to the printed template in the

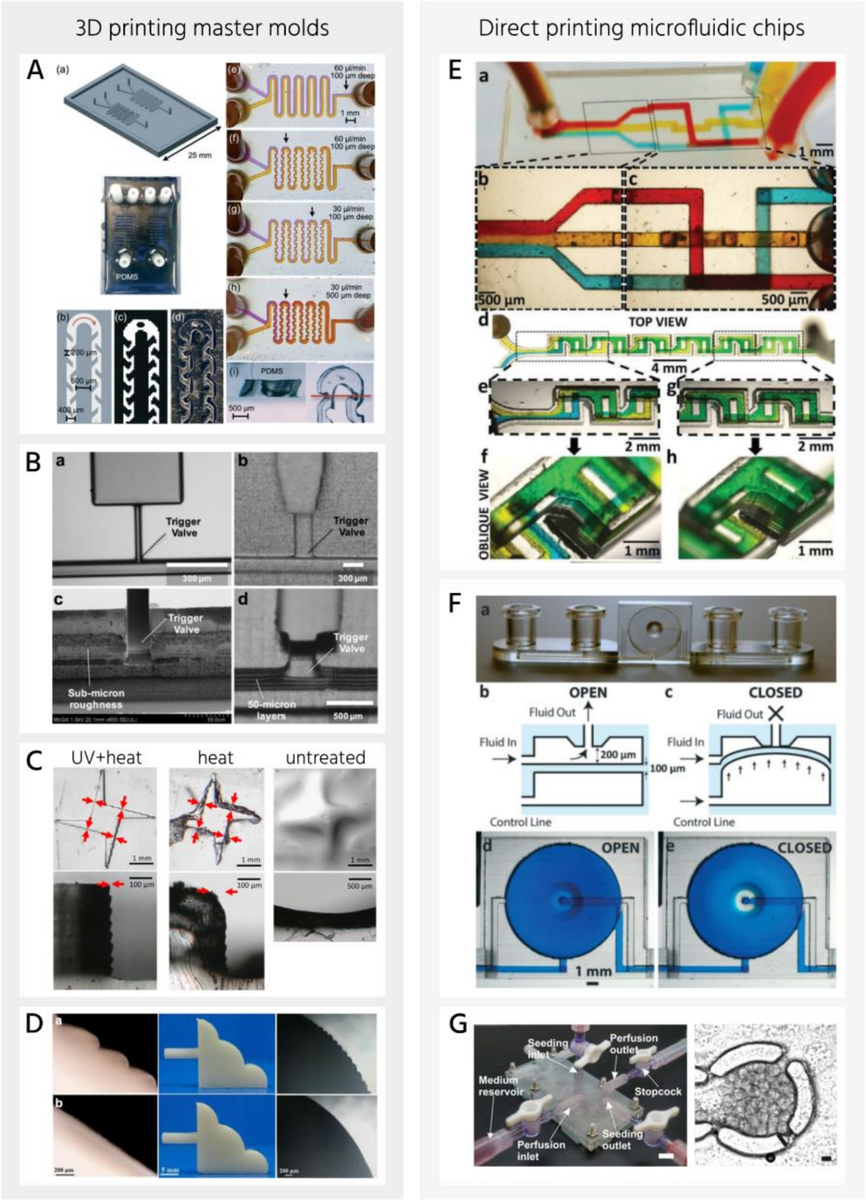

Figure 2.9 Examples of microfluidic chips fabricated either by 3D-printed master molds or directly by 3D printing. (**A**) SL-printed template to fabricate microfluidic diffusive and chaotic mixers. Adapted from Ref.[196] with permission of the Royal Society of Chemistry. (**B**) Master molds (top row) and their corresponding PDMS replicates (bottom row) of capillary trigger valves fabricated by traditional photolithography (left side) or SL printing (right side). Adapted from Ref.[221] with permission of the Royal Society of Chemistry. (**C**) Top view (top row) and cross-sections (bottom row) of fully, partially, and uncured PDMS replicates, which have been cast using 3D-printed molds that have either been left untreated or have been thermally post-processed with or without additional UV post-curing. Adapted from Ref.[223] under the terms of the CC BY-NC-ND 4.0. (**D**) Surface smoothing of FDM-printed ABS part using acetone vapor before (top row) and after (bottom row) treatment. Adapted from Ref.[181] with permission of Springer-Verlag Londong. (**E**) 3D microfluidic router (top) and 3D fluidic mixer (bottom) both fabricated by stereolithography. Adapted from Ref.[35] with permission of John Wiley & Sons. (**F**) Pneumatic membrane valve 3D-printed using SL and the WaterShed XC 11122 resin. Adapted from Ref.[230] with permission of the Royal Society of Chemistry. (**G**) 3D-printed microfluidic chip (left side) developed for the culture of multicellular spheroids (right side). Adapted from Ref.[43] with permission of IOP Publishing.

same study.[223] To prevent both PDMS curing inhibition and strong attachment to the mold, the group suggested a post-processing protocol combining UV post-curing and thermal treatment, which was evaluated on 16 commercially available SLA resins. Other groups had also suggested similar protocols[37,219] as well as ethanol treatmant[196,219], temporary surface coating[196], and silanization[219,220] to achieve complete polymerization of the PDMS and enhance its release of the mold.

Besides the development of post-processing protocols to enable PDMS casting from 3D-printed replica molds, several efforts have been made to optimize the surface quality of the 3D-printed part as surface artifacts and a high surface roughness impairs the bonding strength of the PDMS replicate to substrates typically used in microfluidic platforms, *e.g.* glass.[37] The inherent layering nature of the 3D printing process gives rise to the so-called staircase effect, which impedes the optical quality both of the print and the replicated PDMS layer.[224] Good optical quality, however, is a crucial requirement for most organ-on-a-chip applications as these are mainly accessible by imaging techniques for phenotypical and functional analyses of the incorporated cellular material.[48,167,225] The staircase effect is most pronounced on the surface of rounded features due to the discretization of such features by slices of the defined layer thickness of the 3D printer (**Figure 2.9D**).[209,226] Attempts to mitigate the poor surface finish include adaptive slicing[227], optimization of the part orientation[34,226], grayscale light exposure[228], and post-processing of the 3D-printed part by acetone vapor[181].

Up to now, the resolution, accuracy, and surface roughness of most state-of-the-art 3D printers are still inferior to established photolithography protocols, which enable the fabrication of features in the range of 10-20 µm.[34,221] However, for intermediate dimensions (> 50 µm), such as those required for 3D cell cultures[31], as well as applications that require multiple dimensions on the same mold[195,229], 3D printing of replica molds provides a promising strategy to overcome the inherent manufacturing limitations of traditional soft lithography.

2.4.2.2 Direct printing

3D printing enables the rapid, assembly-free fabrication of complex and truly three-dimensional microfluidic platforms including enclosed channels, integrated membranes, and multi-level circuits[35,41,42] on an unprecedented scale. For example, Kuo *et al.*[35] employed stereolithography to produce a 3D-fluid router and an active microfluidic mixer integrating PMVs in a single manufacturing step (**Figure 2.9E**). Especially the integration of active components such as valves and pumps in directly printed microfluidic chips presented a challenge due to the decreased flexibility of materials commonly used in 3D printing: their Young’s modulus is typically about two to three orders of magnitude higher than that of PDMS.[183,230] To enable the 3D printing of materials with higher flexibility, various groups have developed photocurable resins based on *e.g.* TPU[208], poly(ethylene glycol) di(acrylate) (PEG-DA)[183,199], or acrylated silicone macromers[44]. Using custom-made as well as proprietary resins various designs of integrated, pressure-driven valves have been proposed in the literature up to now.[183,230–232] While most of these are based on a large, circular diaphragm that seals an orifice in the ceiling[199,230] (**Figure 2.9F**), Lee *et al*.[183] recently proposed a slightly modified version of the Quake-style valve traditionally used in mLSI, which is about one order of magnitude smaller than other 3D-printed PMVs and thus amenable to large-scale integration in microfluidic chips.

Some of the strengths and weaknesses of additive manufacturing techniques compared to PDMS-based soft lithography have already been discussed in previous chapters. However, to use directly printed microfluidic chips for cell culture studies, additional requirements, with biocompatibility being one of the most important ones, need to be fulfilled. Unfortunately, characterization of the biocompatibility of a wide variety of printing materials is either missing, especially for many proprietary resins used in stereolithography, or yielded contradicting results. For example, the DLP resin PlasCLEAR based on polypropylene/ABS was found to be biocompatible in one study[233], while another study highlighted impaired viability when exposing cells for longer than 24 hours to the material[234]. Direct comparison of the two studies is, however, limited, as both groups had used different cell lines and post-processing protocols, two parameters that have been demonstrated to significantly impact the biocompatibility evaluation of 3D printing materials.[44,206] Besides flexibility and biocompatibility, the gas permeability and transparency of PDMS are critical material characteristics for many biological applications of microfluidic devices. For example, insufficient oxygen supply can lead to hypoxia-induced impaired function of human islets[235], and thus regular oxygenation needs to be ensured on organ-on-a-chip devices. Since most 3D-printing materials are hard plastics with poor gas permeability, oxygen supply needs to be regulated independently on such systems, *e.g.* by incorporation of additional, gas-transporting microchannels[235,236]. While the optical transparency of several SL- and FDM-printed microfluidic chips are comparable to PDMS[35,207], some printing resins such as silicone hydrogel[44] or PEG-DA[35] even outperformed PDMS in terms of small molecules absorption, which is significantly reduced in the printing resins.

Overall, huge progress has been made in the development of 3D-printed microfluidics, and the first proof-of-concept studies culturing tumor tissue[234], cardiomyocyte-like cells[44], and multicellular spheroids[43] (**Figure 2.9G**) on 3D-printed platforms have already been demonstrated. Nevertheless, direct printing instead of PDMS-based fabrication of organ-on-a-chip devices still faces several challenges regarding feature resolution, surface roughness, optical transparency, autofluorescence, solvent compatibility, gas permeability, and biocompatibility[45,46]. These need to be addressed in the future to fully exploit the design flexibility and rapid prototyping offered by 3D printing. While 3D printing is also not suitable for mass production of organ-on-a-chip platforms, it allows rapid evaluation of design prototypes, and fabrication of personalized devices at a reasonable cost and throughput, and thus, enables a smooth transition to mass production techniques such as injection molding.[45]

3. Characterization of 3D-printing as a fabrication technique for microfluidic chips

For 3D printing to be applied to the fabrication of microfluidic devices and organs-on-a-chip it requires a robust fabrication process, feature dimensions in the 100 µm range, good surface quality, and compatibility with biological systems, most important cells. To evaluate the suitability of the DLP printing technology and commercially available resins either for the fabrication of PDMS replica molds or direct printing of functional devices, three different printing resins have been characterized in detail. The results of this thorough characterization are presented and discussed in the following chapters.

3.1 Materials and methods

3.1.1 Printing resins

Three commercially available resins have been chosen and characterized within the scope of this thesis. The choice of materials was based on a set of requirements including thermal stability of at least up to 80 °C, transparency, and biocompatibility (**Table 3.1**).

Photopolymerizable Resin	Supplier	Molding or direct printing	Chemical basis	Minimum printing layer thickness	Glass transition/ melting temperature	Transparent	Biocompatibility
PlasGRAY	Asiga	molding	Methacrylate[237]	10	84°C	no	n.r.
Freeprint Mould	Detax	both	Acrylate[238]	10	n.r.	yes	[44]
GR-10	Pro3dure	both	Methacrylate[234]	10	n.r.	yes	[234,239]

Table 3.1 Overview of printing resins. Chemical basis, minimum printing layer thickness, and glass transition/melting temperature are provided by the supplier. Biocompatibility lists studies investigating the suitability of the material for working with living systems. n.r. – not reported.

3.1.2 3D-printing workflow

CAD models of the designs were generated in SolidWorks (version 2018-2019; Dassault

Systèmes, France) and 3D-printed using a DLP stereolithography printer (Pico2HD, Asiga, Australia). All materials were processed with printing parameters (*e.g.* light intensity, exposure time) according to the manufacturer's material file. The printing layer thickness was set to the minimum possible for each resin (see **Table 3.1**) unless stated otherwise. 3D-printed molds were printed as negative with extruding channels.

For cleaning, printed parts printed were removed from the building platform, rinsed with isopropyl alcohol, and sonicated for 3 min in a bath of fresh isopropyl alcohol. Parts were subsequently dried for 1 h at 80 °C followed by post-exposure on each side in a flash-curing device (Otoflash G171, NK-Optik, Germany) using 2000 flashes.

3.1.3 PDMS replica molding

To cast PDMS from 3D-printed templates, a surface coating to enhance PDMS curing and peel-off were required. For this, templates were temporarily coated with methylcellulose based on a previously developed protocol[13] and performed immediately before pouring liquid PDMS. In short, 3D-printed templates were coated for 10 min in 0.1% hydroxypropylmethylcellulose (Fluka Analytical) dissolved in 0.2 M sodium phosphate (Sigma), washed with deionized water, and dried with nitrogen. To cast PDMS, Sylgard® 184 (Dow Corning, MI, USA) was mixed in a 10:1 ratio of base material to curing agent, poured onto the 3D print, and degassed in a vacuum chamber. Finally, PDMS was cured for 1.5 h at 80 °C and subsequently released off the mold.

3.1.4 Characterization of the printing resolution

To characterize the resolution of the DLP printer for the different printing resins, two different designs have been created (**Figure 3.1**). The design to characterize the *XY* resolution incorporated arrays of rectangular microchannels of the same height (h_{xy} = 200 µm), but different widths (w = 25-200 µm). The spacing in between two microchannels (d) was designed to be the same as the width of the channel ($d = w$). To exclude printing direction bias, channels were oriented along the *X* and *Y* direction, as well as at a 45° angle (**Figure 3.1A**). The design to characterize the *Z* resolution comprised various features (pillars, channels, domes, cubes) with heights (h_z) ranging from 15 µm to 10 mm (**Figure 3.1B**). Specimens of both designs were printed, cleaned, and post-processed for PDMS casting as described above using all printing materials except for GR-10, which was only used to print the *XY* design. PDMS layers of approximately the same height were cast from the specimen and cut orthogonally to the feature axes for measurements. Surface measurements of the *XY* molds were recorded using a confocal laser scanning microscope (VK--X250; Keyence, Japan) and exported by the proprietary microscope software (VK Analyzer, v.3.8.0.0, Keyence). Additionally, images of the PDMS cross-sections were acquired on an inverted microscope and subsequently analyzed in ImageJ

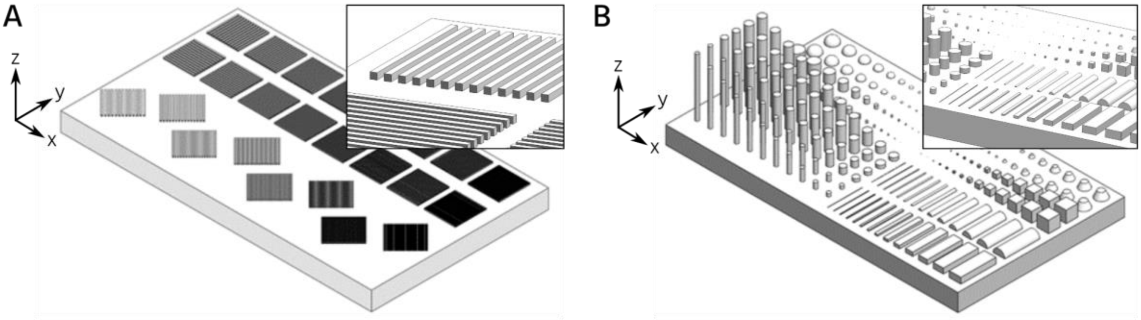

Figure 3.1 Designs of 3D-printed specimen to characterize the resolution of the 3D printing process. (**A**) Arrays of rectangular microchannels of uniform height with widths and gaps in between channels ranging from 25-200 µm (from right to left) were used to quantify the *XY* resolution. (**B**) Features of various shapes with heights ranging from 25 µm to 2 mm were used to characterize the *Z* resolution.

(v1.53f51). For characterization of the resolution in *Z*, PDMS cross-sections were used. Quantification and statistical analysis were performed in MATLAB.

3.1.5 Surface measurements

Surface roughness measurements on 3D-printed parts were performed using a confocal laser scanning microscope (Keyence). Surface roughness values were calculated by the proprietary microscope software (VK Analyzer, v.3.8.0.0, Keyence). Statistical analysis was conducted using a custom-written MATLAB script. Measurements were conducted on three independently fabricated specimens ($N = 3$).

Water contact angle measurements were conducted by depositing a drop of 10 µL of MilliQ water on the planar surface of a 3D-printed test block (area: 10 mm x 10 mm, height: 5 mm, printing layer thickness: 100 µm). Images of the water drop on the surface have been taken with a digital camera (SX620 HS, Canon, Japan) from the side, focusing on the interface between the water drop and the 3D-printed surface. Measurements of three independently fabricated test blocks have been performed ($N = 3$).

3.1.6 Preparation of material eluates

The biocompatibility of the different printing resins was assessed indirectly based on ISO 10993-5:2009 and ISO 10993-12:2009.[240,241] The norm provides a rough guideline to evaluate a material's *in vitro* cytotoxicity indirectly by first creating an eluate of material in normal cell growth medium and then using this eluate as the culture medium for the cells. If inoculation of the cells with the material eluate for a defined period (typically 24 h) leads to a more than 30% lower cellular viability compared to untreated controls, the material is considered cytotoxic.

Sample design. For the generation of the material eluates, circular samples of each printing resin were prepared. To evaluate the effect of potentially insufficient penetration of the UV light during post-exposure through the whole volume of the sample, and thus, potentially toxic uncured monomers and resin additives remaining in the bulk material, circular specimens of different heights were designed (**Figure 3.2**). The samples were designed to have a diameter of 8 mm and a height of 4 mm and 8 mm for the thin and thick designs, respectively. These dimensions yielded a surface area of 1.51 cm^2 and 3.02 cm^2 for the thin disc and thick cylinder, respectively. These are important since ISO 10993-12:2009[241] precisely regulates the ratio of the sample's surface area to the volume of the cell growth medium for the generation of the material eluate. For polymeric materials, the norm requires the surface-to-volume ratio to be 6 cm^2/mL.

Preparation of 3D-printed samples for testing. In a first experiment, samples of the different printing resins were 3D-printed, cleaned, and post-processed as described above, followed by 8 h extraction in ethanol since this has been shown to improve the biocompatibility of 3D-printing resins in previous studies.[206,238] In a second experiment, the impact of UV light post-exposure and chemical extraction on the resins' biocompatibility were also evaluated. For this, parts were either post-exposed to 2-times 2000 flashes or not post-exposed at all. If chemical extraction was performed, parts were immersed for 8 h in ethanol (EtOH), followed by 24 h in deionized (DI) water. In between, parts were allowed to dry for 30 min at room temperature. Before use for cell experiments, samples were sterilized for 1 h using 254 nm UV light (NK-Optik).

Test setup and workflow. The *in vitro* cytotoxicity of the materials was assessed for more and less sensitive cell types, human iPSCs and NIH3T3s respectively, using an indirect test setup. For this, post-processed specimens were incubated in the respective cell type's growth medium at the required surface-to-volume ratio (6 cm^2/mL) in a humidified atmosphere at 37 °C and 5% CO_2 for a defined extraction period. For the first tests using NIH3T3s and human iPSCs, the extraction period was 24 h (short-term extraction). For the second round of testing, an extended extraction period of 5 days (long-term extraction) was used to evaluate whether longer extraction might cause toxic species to leach out of the printed parts. 24-48 h before the

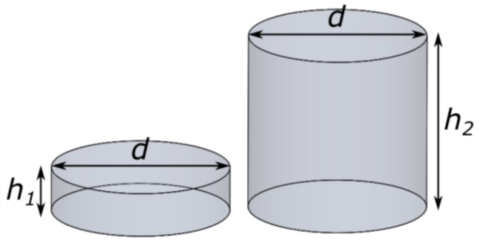

Figure 3.2 Design of circular specimens for indirect biocompatibility testing. Both samples had the same diameter (*d*) of 8 mm. The height of the thin disc (h_1) was 4 mm, while the thick cylinder had a height (h_2) of 8 mm.

inoculation of NIH3T3s and human iPSCs with material eluates, the cells were detached using the same method as in routine passaging, resuspended in fresh growth medium at a concentration of 1.0 x 10^5 and 2.5 x 10^4 cells/mL, respectively, and seeded as a single cell solution in 96-well plates. Human iPSC culture media was supplemented with ROCK inhibitor (Y-27632; Apexbio Technology, TX, USA) for the first 24 h, but removed for subsequent culture. When cells had reached about 80% confluency, the growth medium was replaced by 100 µL of the material eluates. *In vitro* cytotoxicity was assessed at different time points after inoculation (24 h, 48 h, 96 h) using the WST-8 assay.

Indirect biocompatibility experiments using short-term extraction were performed twice independently for NIH3T3s ($N = 2$) and once for human iPSCs ($N = 1$), while the long-term extraction test was performed once for human iPSCs ($N = 1$). All experiments were conducted with at least three technical replicates.

3.1.7 Preparation of monolithic microwell inserts

To assess the feasibility of 3D-printed microfluidic chips for 3D human stem cell culture applications, a simplified test setup using a monolithic microwell insert that fits into the well of a 48-well plate (**Figure 3.3A**) was developed. The test setup aimed to investigate whether the 3D-printed insert allows for the homogeneous formation of 3D human stem cell cultures as well as their long-term culture without comprising the aggregates' viability.

Sample design. The monolithic insert contained 121 straight or 155 conic-shaped microwells with a diameter of 300 µm at the top and a height of 450 µm (**Figure 3.3B**, **C**). The microwells were designed as through-holes for optical accessibility of the aggregates using an inverted microscope to facilitate viability analyses.

Printing and post-processing of 3D-printed microwells for testing. Microwell inserts were printed with the GR-10 resin with the opening attached to the building platform and a printing layer thickness of 25 µm. Supports were added to the design in the Asiga composer software (v1.2.9) with a contact width of 500 µm and an overshoot of 1 mm. After printing, parts were carefully removed from the platform, cleaned with 2-propanol, and post-processed using different combinations of the steps outlined in **Table 3.2**. Additionally, some inserts were surface-activated using air plasma (40 W at 0.4 mbar for 30 s) to enhance the wettability of the 3D-printed microwells. Following post-processing, microwells were sealed by bonding the insert to either glass or polystyrene using a double-sided adhesive foils. Alternatively, microwells were directly sealed by the same or another, only single-sided adhesive foil (**Table 3.3**). Before being used for cell culture experiments, the insert was wetted with 150 µL of Dulbecco's phosphate-buffered saline (DPBS; Sigma-Aldrich) and coated with the same volume of 10% Pluronic F127 (Sigma Aldrich) overnight at 4 °C to minimize cell attachment. Pluronic was then washed with DPBS and inserts were sterilized for 1 h using 254 nm UV light (NK-Optik).

UV post-exposure	Chemical extraction	
	99.9% EtOH	DI water
-	-	-
2x2000 flashes	2h	2h
2x4000 flashes	24h	24h

Table 3.2 Overview of post-processing steps applied on 3D-printed microwell inserts. Different combinations of post-exposure and chemical extraction have been investigated in direct biocompatibility testing.

Name	Manufacturer	Double-/ single-sided?	Adhesive type	Thickness	Certified as biocompatible?
ARcare 90445Q	Adhesives Research	Double-sided	Acrylic	80 µm	yes
9795R	3M	Single-sided	Silicone acrylic/acrylate	100 µm	yes

Table 3.3 Adhesive tapes used for sealing of microwell inserts. Double-sided tapes were used for bonding to glass and polystyrene substrates as well as for direct sealing. The single-sided tape was only used for direct sealing.

Test setup and workflow. Before seeding cells, DPBS in the inserts was replaced by the cell culture medium, followed by incubation of the inserts in a humidified incubator at 37 °C and 5% CO_2 for 30 min to allow for equilibration. Human iPSCs were seeded as a single-cell suspension at a concentration of 500 cells/microwell in a total of 40 µL of growth medium per insert (~ 6-8 x 10^4 cells/insert). The cell suspension was added inside the inner rim of the insert to enhance gravity-assisted trapping of the cells inside the microwells. After 10 min of settling time, another 100 µL of growth medium was added to the recess of the insert and the cells were incubated in a humidified atmosphere at 37 °C and 5% CO_2. For cell seeding, the growth medium (mTeSR$^+$ + 1% penicillin-streptomycin) was supplemented with 1‰ of ROCK inhibitor. 24 h after seeding and in the following every other day, the medium was replaced by 150 µL of fresh growth medium without the addition of ROCK inhibitor.

To assess the viability of the cell aggregates, a WST-8 assay was performed on days 1, 3, and 7 after seeding, and an additional live/dead staining on day 7. Additionally, representative brightfield images of the inserts were acquired on the same days as the assays to track cell aggregate formation and growth. Experiments were conducted three times independently with 2-3 technical replicates per sample (N = 2-3).

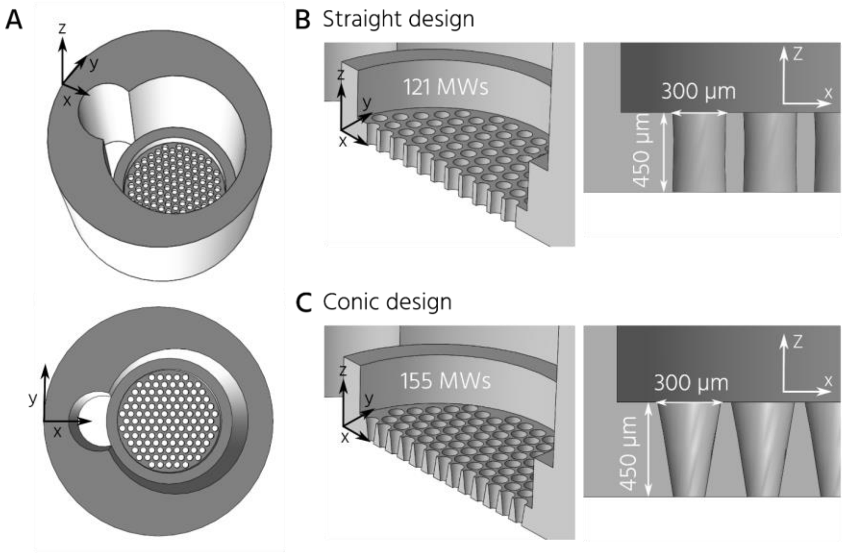

Figure 3.3 Design of a 48-well plate insert integrating straight or conic-shaped microwells for 3D cell cultures. (**A**) 3D rendering of the insert with straight microwells. The 1 mm high rim around the microwell array facilitated seeding of the cells in minimal volume (40 µL) directly on top of the microwells, minimizing dead volume. The recess on the left is used for medium change without disturbance of the cells. (**B**) For the straight design, one insert comprises 121 microwells (MWs), each with a diameter and height of 300 µm and 450 µm, respectively. (**C**) For the conic design, one insert comprises 155 microwells (MWs) with a diameter of 300 µm at the larger top of the MW and a height of 450 µm.

3.1.8 WST-8 assay

Cellular viability was measured using a colorimetric assay that is based on the 2-(2-methoxy-4-nitrophenyl)-3-(4-nitrophenyl)-5-(2,4-disulfophenyl)-2H-tetrazolium monosodium (WST-8) salt.[242] In the presence of an electron mediator, cellular dehydrogenases reduce the WST-8 to a water-soluble formazan dye. The amount of formazan dye produced is directly proportional to the number of viable cells and can be quantified by colorimetry. Impaired metabolic activity of the cells or cell death due to cytotoxic species present in the culture leads to diminished dehydrogenase activity and thus, reduced amounts of the formazan dye. Comparison of cell cultures with impaired metabolic activity to healthy control with equivalent initial cell numbers allows for quantification of the cytotoxic effect.

To perform the assay, the WST-8 stock solution of the cell counting kit was mixed with growth medium at a 1:10 ratio, added to the cell culture, and incubated for 2 h in the dark in a humidified incubator. Afterward, the absorptions of the solutions were measured on a photometer (Varioskan Lux, Thermo Fisher) using a 450 nm and 620 nm filter and analyzed using custom-written MATLAB scripts. The viability of the cells was calculated with

$$viability = \frac{A - A_{blank}}{mean(A_{Ctrl} - A_{blank})}$$

where A is the absorption of the extracts ($N = 3$ per material), A_{Ctrl} is the absorption of the control samples ($N = 3$ per material), and A_{blank} is the absorption of the blank WST-8 growth medium mixture (no cells, $N = 3$).

3.1.9 Live/dead staining

To determine the viability of cells qualitatively, cell aggregates were stained with two different fluorescent dyes using a commercial staining kit (ReadyProbes^{TM} Cell Viability Imaging Kit Blue/Green; Thermo Fisher). In this kit, the nuclei of all cells are stained with one reagent, while the other reagent only stains the nuclei of dead cells with compromised plasma membranes. In short, 2 drops each of the live and dead cell staining reagents were added per 1 mL of growth medium to prepare the staining solution. Then, the medium surrounding the 3D cell cultures was aspirated, an appropriate volume of staining solution was added, and cell aggregates were incubated for 30-60 min in a humidified incubator in the dark. Afterward, aggregates were imaged on an epifluorescent microscope (Evos M5000, Thermo Fisher). Live cells were detected with a standard DAPI filter (excitation/emission maxima: 360/460 nm) and dead cells with a GFP filter (excitation/emission maxima: 504/523 nm).

3.1.10 Microscopy and statistical analysis

Bright-field images were acquired with 2.5x and 10x objectives (Plan-Apochromat) on an Axiovert inverted microscope (Zeiss, Germany). An epifluorescent microscope (Evos M5000, Thermo Fisher) was used to record the fluorescent images. Image analysis and statistical evaluation were performed using custom-written macros and scripts in ImageJ and MATLAB, respectively. Given values are mean ± SD unless stated otherwise. Testing for normal distribution was done by Shapiro Wilk's test[243] in MATLAB. Statistical analysis was also performed in MATLAB using a one-way ANOVA test with an accepted statistical significance (p-Value) less than 0.05 unless stated otherwise.

3.2 Results and discussion

3.2.1 Printing resolution

The resolution of 3D printing depends on several factors such as the resolution of the pixel grid of the printer, optical precision, UV light exposure time, as well as characteristics of the printing resin, *e.g.* the concentration of photoinitiator additives or resin viscosity.[35,44,216] While 3D printers have often been optimized for specific proprietary resins, yielding similar resolutions with custom resin formulations or printing resins from other manufacturers is often laborious.[216] Therefore, a 3D printer that allows using proprietary resins from different manufacturers with a reasonable nominal resolution was chosen. The Pico2HD (Asiga) provides a DLP-based, open material system and an *XY* pixel size of 27 µm. Since the actual lateral resolution of SLA printers sometimes differs by as much as 70% from the nominal resolution[202], the first step to evaluating the suitability of 3D printing for microfluidics comprised the characterization of the dimensional accuracy and minimal feature size of three commercially available printing resins: Freeprint Mould (Detax), GR-10 (pro3dure), and PlasGRAY (Asiga). For this, a test mold comprising patterns of extruding rectangular channels with heights of 200 µm and widths varying between 25-200 µm was printed for all materials with a *Z*-layer thickness of 50 µm; the distance between the channels was equal to their widths (CAD model displayed in **Figure 3.1A**). Besides surface measurements conducted on the 3D-printed molds, cross-sections of PDMS layers cast from the molds were used for the characterization of the printing resolution in the lateral direction (*XY*). Printing of individual channels with at least 80% of their nominal height was considered successful.

Channels with widths and distances of 50 µm or below could not be printed in any of the materials. The smallest printable *XY* dimension was 75 µm for PlasGRAY and 100 µm both for Freeprint Mould and GR-10 (**Figure 3.4**). These dimensions are about three to four times the pixel size of the 3D printer. In the literature, channel widths of 2 px have been reported for DLP printers with similar pixel sizes and custom resin formulations, which have been optimized for printing resolution.[35,44] Pattern dimensions larger than 100 µm produced properly resolved channels for all materials with significantly ($p < 0.01$) different lateral accuracy of the 3D-printed channels (**Figure 3.5A**). Channel patterns printed in Freeprint Mould and GR-10 were on average 1% and 11% larger than in the design, while they were 23% smaller when printed in PlasGRAY. Other DLP resins have been reported to cause a similar deviation of the designed and actual channel width, typically ranging between 7% and 25%.[37,44] In contrast to the dimensional decrease of the PlasGRAY molds, however, the printed features are commonly larger than the nominal width. A possible explanation for this might be the insufficient duration of the exposure as it has been observed that feature widths become smaller if the exposure time was decreased.[217] This characteristic might also be exploited as a possibility for the miniaturization of microfluidic channels.

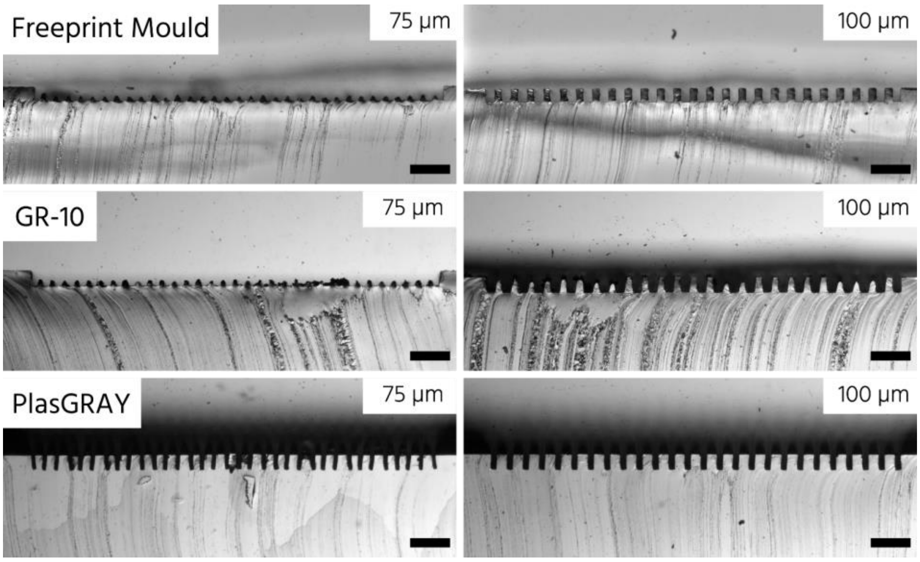

Figure 3.4 PDMS cross-sections of 3D-printed sample molds to characterize the lateral printing solution. Molds made of Freeprint Mould, GR-10, and PlasGRAY have been 3D-printed and subsequently used to cast PDMS. Channels with designed widths and gaps of 75 µm and 100 µm were only printed in PlasGRAY with sufficient height. Channels in Freeprint Mould and GR-10 could not be resolved properly. Scale bar: 500 µm.

PDMS casting of the 3D-printed molds resulted in significantly ($p < 0.01$) wider channels for all materials (**Figure 3.5B**). PDMS channel widths were on average 105%, 119%, and 82% of the nominal width for Freeprint Mould, GR-10, and PlasGRAY respectively. Lateral expansion of the channel is likely due to the thermal expansion of the 3D-printed mold during PDMS curing. This expansion is counteracted by PDMS shrinkage due to curing at elevated temperatures. For a curing temperature of 80 °C, which was used here, PDMS is known to shrink by approximately 1.5% to 1.9% compared to the mold dimensions.[244,245] To ensure that the orientation of the channel patterns did not influence the resolution of the prints, separate patterns running either along the *X* or the *Y*-axis of the printer were designed and evaluated. No significant differences were detected in any of the materials (**Figure A.1**).

Besides the lateral resolution, the *Z* resolution of the printer was characterized using another test mold comprising various extruding features such as rounded bumps, and rectangular and half-rounded channels with heights ranging from 15 µm to 2 mm (CAD model displayed in **Figure 3.1B**). Additionally, the design included pillars with diameters between 600-1250 µm and heights up to 10 mm to investigate the manufacturability of aspect ratios between 1:1 and 17:1 (height : diameter). All test molds were printed with the smallest possible layer thickness, which was 10 µm for all printing resins. Attempts to print and characterize test molds using the GR-10 resin were not successful due to the destruction of the liquid tank bottom during printing arising from instability and break-off of the high aspect ratio pillars. For Freeprint Mould and PlasGRAY, high aspect ratio pillars (17:1) were printed successfully. Recently, even higher aspect ratios have been demonstrated for DLP printed channels using a PEG-DA-258-based resin formulation.[35] After optimization of the resin, microfluidic channels with aspect ratios up to 37:1 have been fabricated successfully in the study. Characterization of the *Z* resolution of

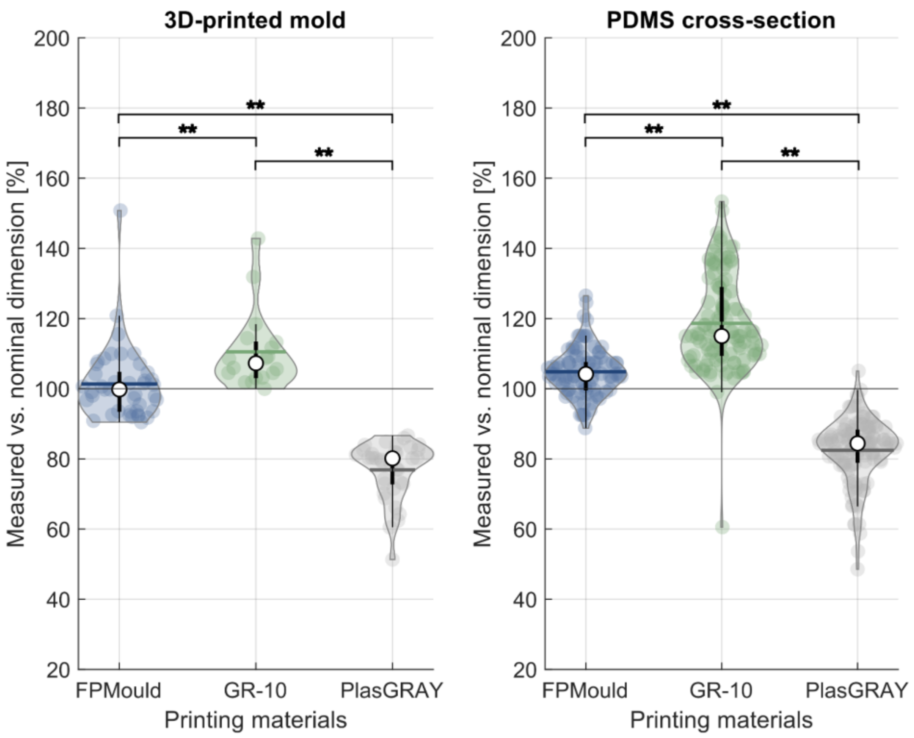

Figure 3.5 Printing resolution in *XY* direction for different printing resins. (**A**) The mean channel widths on the 3D-printed molds varied between 101%, 111%, and 77% of the nominal dimension for Freeprint Mould (FPMould), GR-10, and PlasGRAY, respectively. $N = 2$ individually printed molds for FPMould and PlasGRAY, $N = 1$ for GR-10. ** $p < 0.01$ using one-way ANOVA (**B**) The mean channel widths in the PDMS cross-section varied between 105%, 119%, and 82% of the nominal dimension for FPMould, GR-10, and PlasGRAY, respectively. Displayed are the individual data points (colored points), probability density (colored structure), mean (colored line), median (white dot), and interquartile range (black bars) for the different printing resins. $N = 2$ individually cast PDMS layers. ** $p < 0.01$ using one-way ANOVA.

the two printing resins here was performed using PDMS cross-sections instead of the 3D-printed molds due to the large height variation of the test mold. The smallest possible feature heights to be printed were 25 µm for Freeprint Mould and 50 µm for PlasGRAY (**Figure 3.6**), which are comparable to previously achieved resolutions for DLP printing.[34,37] Features above these sizes printed well for any of the shapes tested. Overall, printed features were on average 14% and 10% smaller than their nominal height for Freeprint Mould and PlasGRAY, respectively (**Figure 3.7A**). Considering equal thermal expansion of the mold in every direction and assuming a similar dimensional offset between the 3D-printed mold and PDMS cross-section as measured in the *XY* direction, this suggests a relative error of 18% and 15% of the 3D-printed features for Freeprint Mould and PlasGRAY, respectively. The deviation of the feature height from the nominal dimension was more pronounced and variable for smaller heights (**Figure 3.7B**). For dimensions above 1 mm, measured heights converged to a plateau of 95% and 97% of the nominal dimension for Freeprint Mould and PlasGRAY, respectively.

Overall, these results highlight the suitability of 3D printing for microfluidic applications in the intermediate size range which is required for organ-on-a-chip applications incorporating 3D cell cultures with dimensions above 100 µm. This size range fits well with the minimum

XY and *Z* resolution of 75 µm and 25 µm, respectively, for the DLP printer and printing resins presented here.

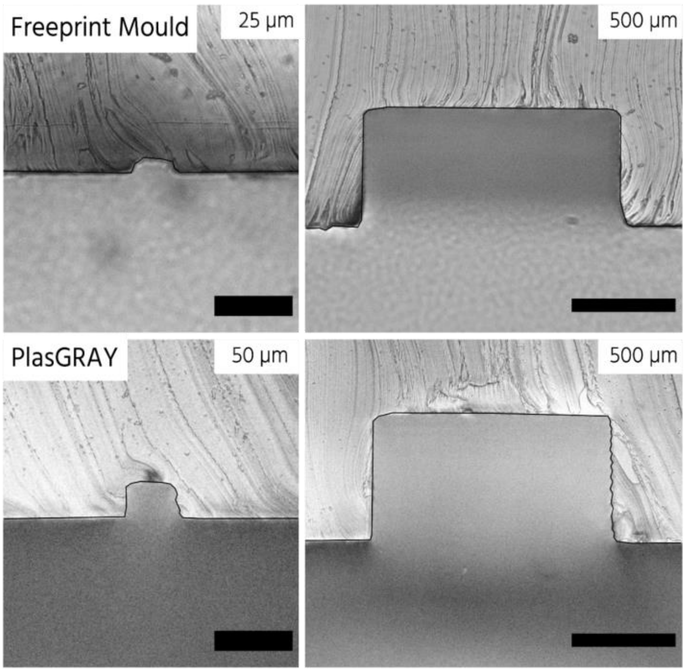

Figure 3.6 PDMS cross-sections of 3D-printed sample molds to characterize the printing resolution in *Z*. The smallest channel height printed was 25 µm for Freeprint Mould and 50 µm for PlasGRAY. In comparison 500 µm high rectangular channels are shown for both materials as reference. Scale bars: 100 µm for the left, 200 µm for the right images.

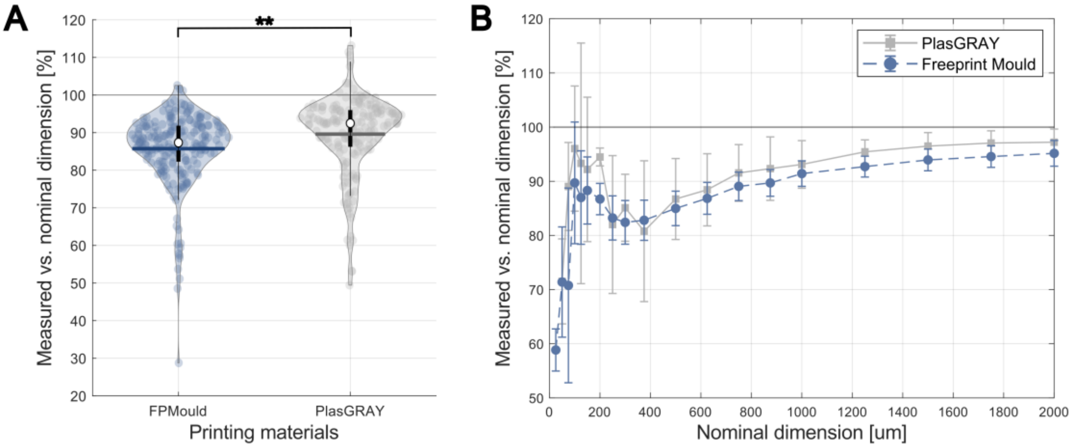

Figure 3.7 Printing resolution in *Z* for different printing resins. (**A**) Overall dimensional accuracy of PDMS cross-sections cast from the 3D-printed molds in *Z* compared to the nominal dimension of the design. Displayed are the individual data points (colored points), probability density (colored structure), mean (colored line), median (white dot), and interquartile range (black bars) for the different printing resins. $N = 2$ individually printed molds with one layer of PDMS cast from each. $**p < 0.01$ using one-way anova. (**B**) Dimensional accuracy of the PDMS cross-sections shown separately for each nominal height of the design. $N = 2$ individually printed molds with one layer of PDMS cast from each.

3.2.2 Surface roughness

The surface roughness of a 3D-printed part is a critical parameter for the application of the technique for microfluidic chip fabrication. Surfaces of high roughness have been associated with reduced transparency[37], poor bonding of PDMS layers to glass[37,220], higher wall friction, and thus hydrodynamic resistances[246,247], large variations in the shear rate near the channel's surface[248], and altered cellular adhesion[249,250]. Surface roughness values (*i.e.* arithmetic mean roughness, R_a) of the different printing resins were obtained using the same test molds as for the characterization of the lateral printing resolution. For this, five planar areas were measured on the top side of the mold, *i.e.* in the *XY* plane of the mold. Obtained values varied significantly between 3.69 µm (SD = 0.66 µm) and 5.88 µm (SD = 1.53 µm) for PlasGRAY and GR-10, respectively, while Freeprint Mould molds had a surface roughness of 4.87 µm (SD = 1.20 µm), which was not significantly different from any of the other materials (**Figure 3.8**). These values are slightly higher than previously reported values for SLA resins, which range between 0.35 and 3.65 µm.[37,202,248] In comparison, the surface roughness of silicon wafers and SU-8 patterns traditionally used for microfluidic chip fabrication is significantly lower at 0.01 µm and 0.11 µm, respectively.[36] To enhance the quality of 3D-printed surfaces coating with PDMS[251] or an omniphobic lubricant as well as projection lens oscillation[224] and optimization of the resin formulation[252] have been exploited. Overall, the presented results underline the variability of the surface characteristics of different printing resins and suggest the usage of PlasGRAY for microfluidic applications which require minimal surface roughness.

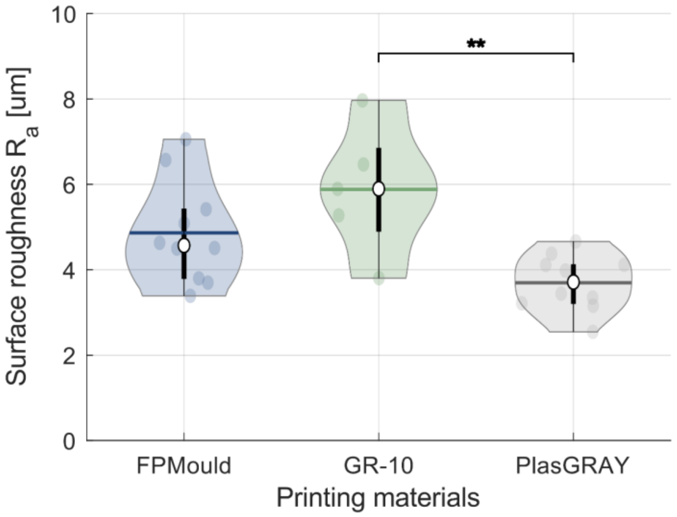

Figure 3.8 Surface roughness of the different 3D-printing resins. Freeprint (FP) Mould and GR-10 had a mean surface roughness of 4.87 µm and 5.88 µm, respectively, while PlasGRAY had a significantly lower mean roughness of 3.69 µm. Displayed are the individual data points (colored points), probability density (colored structure), mean (colored line), median (white dot), and interquartile range (black bars) for the different printing resins. *N* = 3 for FPMould,PlasGRAY, *N* = 2 for GR-10. ** $p < 0.01$ using one-way ANOVA.

3.2.3 Indirect biocompatibility evaluation using material eluates

Biocompatibility of photopolymer resins presents one of the major challenges for the adoption of 3D printing technology for microfluidics. While many of the materials used in FDM printing such as ABS or PLA are biocompatible[205,218], the cytotoxicity of most DLP printing materials is largely unknown as their compositions are proprietary.[239] Further, different studies investigating the biocompatibility of SLA printing resins showed highly varying or even contradicting results for the same resin.[233,234] Opposing findings of different studies can arise from differences in post-treatment of the 3D-printed specimens, the cell types in use, and the biological assay employed for the quantification of the cellular response, all of which have been shown to influence biocompatibility[44,215] and generally hinder study comparison. To increase the reproducibility of the results, the norms ISO 10993-5 and ISO 10993-12 aim to provide a rough guideline for testing the cytotoxicity of materials *in vitro*.[240,241] Biocompatility tests performed in this work also followed this guideline. To more broadly investigate material biocompatibility, two different cell lines have been used: the more robust NIH3T3 fibroblast cell line and human iPSCs, which represent a highly sensitive cell type. Further, to decorrelate effects due to surface characteristics of the printing resins, *e.g.* surface roughness, and leaching of potentially toxic species out of the material, an indirect test setup was chosen. In brief, circular specimens of each resin were prepared as outlined in chapter 3.1.6. The specimens were then used to create an eluate of each material by incubation of them in the normal cell growth medium for 24 h (short-term extraction) or 5 d (long-term extraction) at a defined surface-to-volume ratio (6 cm^2/mL) in a humidified atmosphere at 37 °C and 5% CO_2. The extract was then used as a growth medium for the cells. Finally, cellular viability was assessed after a defined period (typically between 24 h and 72 h) by a colorimetric assay based on the 2-(2-methoxy-4-nitrophenyl)-3-(4-nitrophenyl)-5-(2,4-disulfophenyl)-2H-tetrazolium monosodium (WST-8) salt.[242]. The WST-8 salt is reduced by cellular dehydrogenases to a water-soluble orange formazan product that can be analyzed by colorimetry and is directly proportional to the number of viable cells. To quantify the cellular viability, cells that were incubated with the material eluate are compared to cells cultured in normal growth medium (*i.e.* no presence of material leachables). If the cellular viability of the former is found to be below 0.7-fold of the control's viability, the material is considered cytotoxic.

For a short-term extraction, the viability of NIH3T3 fibroblasts 24 h after being in contact with the material was about the same as the control for all materials (**Figure 3.9A**). After an incubation of 48 h, the viability of cells in contact with PlasGRAY was 1.2-fold the control's viability and significantly higher than any of the other conditions ($p < 0.05$ for Freeprint Mould, $p < 0.01$ for the other conditions). In comparison, cells in contact with Freeprint Mould and GR-10 showed a 1.07- and 1.04-fold higher viability than the control, respectively. Another 48 h later (*i.e.* at 96 h), cells showed a similar trend than before even though PlasGRAY samples varied not significantly ($p > 0.05$) from Freeprint Mould and GR-10. Similar results have been observed for human iPSCs, when in contact with material eluates (short-term

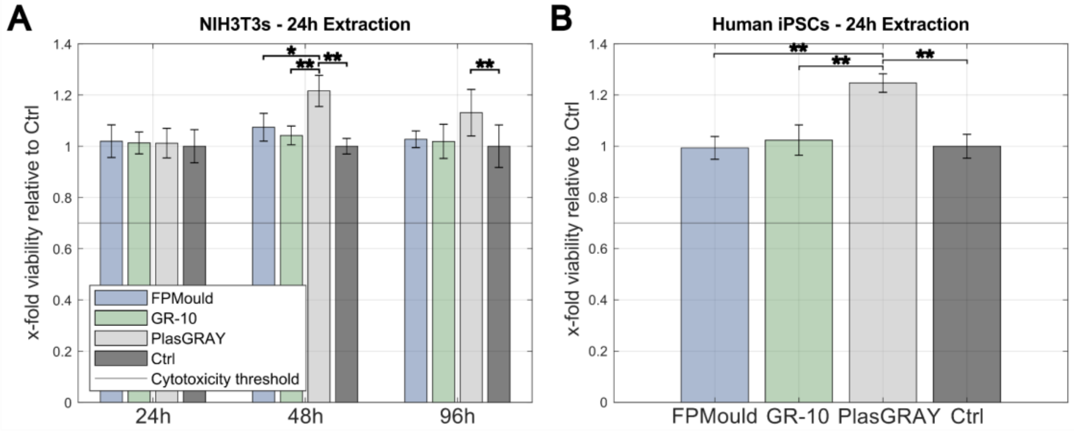

Figure 3.9 Biocompatibility of printing resins after short-term extraction. (**A**) Viability of NIH3T3 fibroblasts when in contact with material eluates for 24 h, 48 h, and 96 h compared to the untreated control at the same respective timepoints. The black line indicates the lower limit of viability for a material to be considered non-cytotoxic. Displayed are the mean ± SD. Ctrl – control. $N = 2$ independent experiments for 24 h, $N = 1$ for 48h and 96h, each with at least three technical replicates. $*p < 0.05$, $**p < 0.01$ using two-way ANOVA. (**B**) Viability of human iPSCs when in contact with the material eluates for 24 h compared to the untreated control. The black line indicates the lower limit of viability for a material to be considered non-cytotoxic. Displayed are the mean ± SD. $N = 1$ experiment with three technical replicates for all materials. $**p < 0.01$ using one-way ANOVA. Ctrl – control.

extraction) for 24 h (**Figure 3.9B**). For this cell type, incubation with the PlasGRAY extract caused significantly ($p < 0.01$) higher viability than for any other material as well as compared to the control. Overall, none of the tested materials showed cytotoxic cellular response upon a short-time extraction in the cell growth medium, and are thus considered biocompatible according to ISO 10993-5.

To investigate the effect of post-processing of the 3D-printed samples on their *in vitro* cytotoxicity in more detail, another round of experiments with Freeprint Mould and GR-10 was performed. Since PlasGRAY is non-transparent and would thus only be applicable for molding, it has been omitted from further testing. Specimens of both other materials comprised circular discs as used in the last experiment (thin condition) as well as thicker cylindrical samples (thick condition) to further investigate the effect of bulk volume. Additionally, the extraction period has been increased to 5 days (long-term extraction) to ensure that longer exposition of the material to the cell culture medium does not cause any detrimental effects such as material degradation or leaching of additional compounds not anticipated before. This time, only iPSCs were used for testing due to their higher sensitivity. Overall, post-processing by UV post-exposure and pre-extraction in ethanol (labeled '+UV +EtOH') yielded the highest cell viabilities across all conditions tested (**Figure 3.10**). For Freeprint Mould, for example, cell viabilities were 1.3 and 2.0-fold the viability of the control at 24 h for the thick and thin specimen, respectively (**Figure 3.10A**). Viabilities for GR-10 at the same time point and in the same sample groups were 1.5 and 1.8 (**Figure 3.10C**), respectively, and not significantly different (**Table A.1**). The higher viability in the treatment groups compared to the control suggests a higher proliferative or metabolical activity of the respective cells. One possible

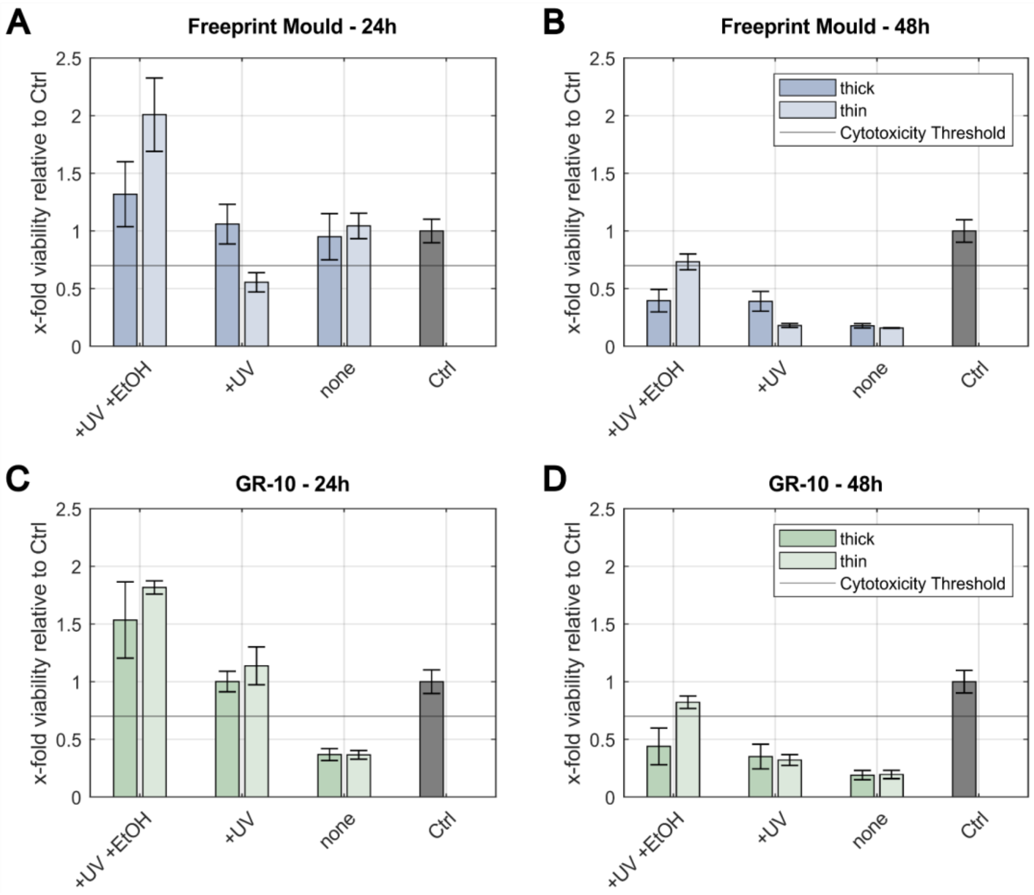

Figure 3.10 Biocompatibility of printing resins after long-term extraction for 5 days. (**A**,**B**) Viability of human iPSCs when in contact with Freeprint Mould eluates for 24 h (A) and 48 h (B) compared to the untreated control at the same respective timepoints. The black line indicates the lower limit of viability for a material to be considered non-cytotoxic. Displayed are the mean ± SD. *N* = 1 experiment with three technical replicates. (**C**,**D**) Viability of human iPSCs when in contact with GR-10 eluates for 24 h (C) and 48 h (D) compared to the untreated control at the same respective timepoints. The black line indicates the lower limit of viability for a material to be considered non-cytotoxic. Displayed are the mean ± SD. *N* = 1 experiment with three technical replicates.

explanation for this is the presence of some kind of cell growth or metabolism-promoting agents in the material eluate. In comparison, only UV post-exposure without ethanol extraction (labeled '+UV') yielded significantly ($p < 0.05$) lower cell viabilities both for Freeprint Mould and GR-10, but were still considered non-cytotoxic except for the thin Freeprint Mould specimen, whose viability was only 0.6 (**Figure 3.10A**). While no post-processing of 3D-printed specimens (labeled 'none') led to viabilities approximately the same as the control for Freeprint Mould, cells incubated with eluates of non-treated GR-10 specimens showed a 0.6-fold decreased viability than the control (**Figure 3.10C**) suggesting the necessity for post-processing of GR-10 for cell studies. Interestingly, thin samples of the Freeprint Mould resin, which have only been treated with UV, showed lower viability than the thick sample, which was generally the other way round for the other conditions. A possible explanation for this is the presence of residual ethanol in the samples due to insufficient drying and extraction with water, which was released into the eluate.[44] Data obtained at 48 h, showed cytotoxic effects (viability < 0.7) of all material eluates except for the thin samples which have been post-treated by UV and ethanol (labeled '+UV +EtOH') both for Freeprint Mould (**Figure 3.10B**) and GR-10 (**Figure 3.10D**) further underlining the need of post-processing workflows. For this condition, cell viabilities were 0.73- and 0.82-fold the viability of the control, respectively. Incubation periods longer than 48 h have not been tested because the growth medium is typically refreshed every 24-48 h in routine cell culture to maintain cellular self-renewal and pluripotency.

Overall, these results highlight the necessity of post-processing 3D-printed specimens to render them biocompatible. UV post-exposure as well as ethanol pre-extraction both caused significant ($p < 0.05$) differences among sample groups (**Table A.1**), which is comparable to outcomes of other studies.[206,239] Further, minor differences between different volumes (thick or thin) of the 3D-printed specimen could be observed, which were, however, not significant ($p > 0.05$). These differences are likely attributable to penetration depth limits of the UV light during post-exposure, which might not be able to penetrate the whole volume of larger samples with the settings used here. To mitigate this effect in the future, for example when culturing cells in 3D-printed microfluidic devices, extended durations of UV post-exposure of the 3D-printed device or adjustments of the design to minimize bulk volume should be considered. Compared to Freeprint Mould and PlasGRAY, cells in contact with GR-10 reliably showed more similar behavior (cell growth and viability) to the control for both short-term and long-term extraction.

3.2.4 Direct biocompatibility evaluation using monolithic microwell inserts

Despite employing 3D printing technology for the fabrication of PDMS replica molds[36,197,253], direct printing[35,43,234] of organ-on-a-chip devices constitutes a potential field of application for 3D printing for microfluidics. As highlighted in chapter 3.2.1, 3D printing still faces some constraints in terms of resolution, limiting the adoption of the technique for 2D cell culture-based microfluidic devices. For 3D cell cultures, however, lateral printing resolutions in the 100 µm range are applicable due to their larger dimensions. However, the suitability of 3D-printed monolithic devices in general for the direct culture of human stem cells is still a matter of debate in the literature and has therefore been investigated in this work.

For this, an insert that fits into the well of a 48-well plate and contains more than 100 microwells for the formation and culture of iPSC aggregates was designed (**Figure 3.11**). Microwells are a commonly used technique for the formation and culture of cellular aggregates. They have been applied by various groups, *e.g.* for 3D human stem cell cultures, and can be generated for example by PDMS soft lithography or hydrogel stamping.[13,14,254] A design that has recently been shown by Brandenberg *et al.*[14] facilitated the automated and high-throughput analysis of thousands of individual gastrointestinal organoids. Instead of stamping the

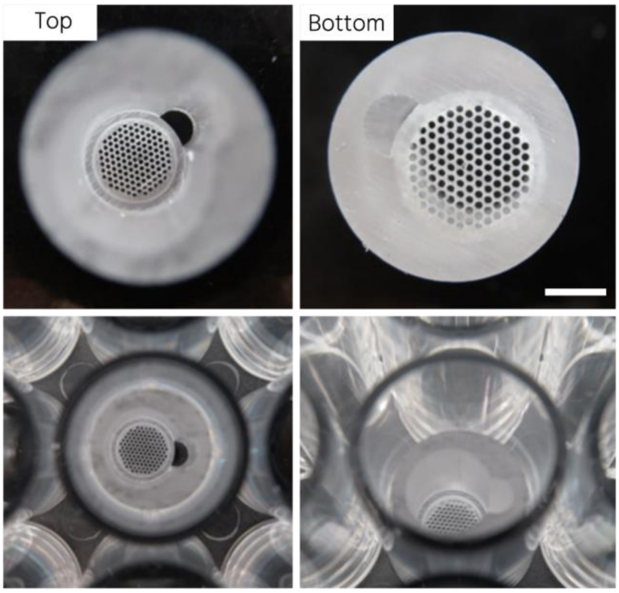

Figure 3.11 3D-printed microwell inserts for 48-well plate in GR-10 resin. The insert contains 121 straight microwells with a diameter of 300 µm and a recess on the side for exchange of cell growth medium. Scale bar: 2 mm.

microwell array into a hydrogel as has been done in their study, the approach presented here exploited 3D printing for the fabrication of such a monolithic microwell array. For this, the orientation of the inserts on the building platform and support structure configuration have first been optimized to successfully print inserts in GR-10. GR-10 was chosen as a printing resin due to its transparency, good biocompatibility, and lower fabrication time compared to Freeprint Mould, where the same design takes about 40% longer. Since the surface roughness of 3D-printed parts does not allow for high-quality imaging of the aggregates from below, *e.g.* when using an inverted microscope, microwells were designed as through-holes. To seal the microwells, the inserts were bonded either to the well plate bottom, which is made of polystyrene, or a cover glass using the double-adhesive tape ARcare 90445Q. To enhance the seal, the area surrounding the microwell array was designed with an offset compared to the microwell bottom. This offset matched exactly the thickness of the tape and yielded a tight seal in between individual microwells and the substrate. Additionally, some inserts have been directly sealed using the same tape or the single-sided tape 9795R. In this case, there was no offset between the surrounding area and the microwell array bottom. To investigate the suitability of the 3D-printed microwell insert for the formation, long-term culture, and analysis of human iPSCs, different post-processing conditions (**Table 3.2**) have also been tested.

Before seeding cells, the inserts were coated overnight with 10% Pluronic F-127 to minimize attachment of the cells to the substrate and enhance self-aggregation (**Figure 3.12**). The next day, cells were seeded as a single cell suspension at a concentration of 500 cells/microwell in a total volume of 40 µL. After allowing the cells to settle down for 10 min, another 100 µL of fresh culture medium was added to the recess of the insert to minimize cellular disturbance.

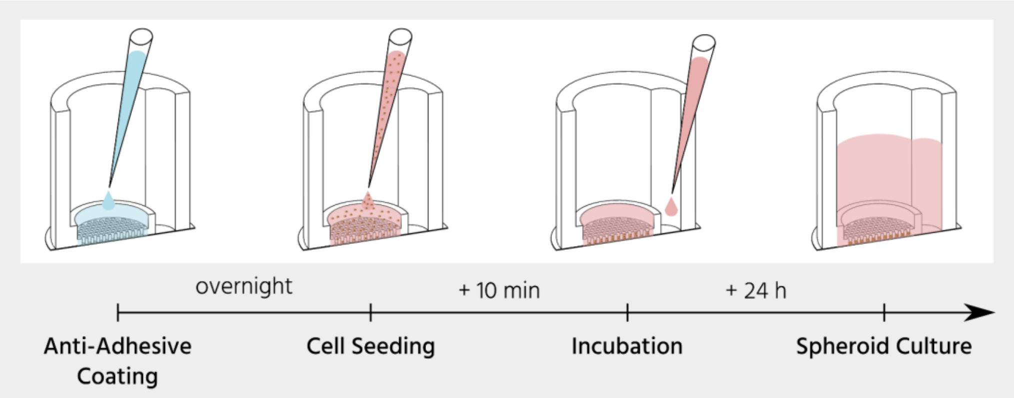

Figure 3.12 Workflow for the formation of 3D cell cultures in microwell inserts. Before seeding, microwell inserts are coated with Pluronic F-127 overnight to minimize cell attachment. Seeding of the single cell suspension directly above the microwells enhances gravity-assisted trapping of the cells. After 10 min of settling time, additional growth medium is added to the recess of the insert to minimize disturbance of the cells. Within 24 h of incubation cells self-aggregate to form 3D cell cultures.

After incubation for 24 h, the formation of 3D cell cultures was confirmed for all conditions except for the glass substrate due to leakage between the microwell array bottom and the glass. While sometimes more than one aggregate had formed in the straight microwells, the conic microwells contained only single aggregates (**Figure 3.13**). This is due to better focusing of the cells within a narrow spot after seeding and has been observed by other groups as well.[255] Accordingly, inserts with conic microwells were preferred for all following experiments. The mean diameters of iPSC aggregates formed in the microwell inserts were on average 80 µm ± 11 µm (**Figure 3.14A**) and did not vary significantly ($p > 0.05$) between different post-curing protocols (2x4000 flashes or 2x2000 flashes). The kind of substrate used for sealing the microwell inserts also yielded no significant ($p > 0.05$) differences in the aggregates' diameter except for glass, where no spheroids had formed due to leakage. Plasma activation of the inserts before sealing drastically enhanced wettability due to increased hydrophilicity. Aggregates formed in plasma-activated microwells were on average 7 ± 11 µm smaller than control aggregates (**Figure 3.14B**). This might be because a larger proportion of cells are attached to the substrate and surrounding microwell walls, as it has recently been demonstrated that hASCs cultured on an oxygen plasma activated poly(l-lactide) acid (PLLA) polymer film maintained their fibroblast-like morphology and did not form spheroids.[256] Interestingly, in the same study human MSCs did acquire spheroid conformation independent of the surface plasma treatment highlighting cell type-specific differences.

Next, differences in the aggregate size depending on the presence and duration of an ethanol pre-extraction were measured. Similar to the results observed in the indirect biocompatibility testing (see **Figure 3.10**), ethanol pre-extraction of the 3D-printed parts was crucial for the formation of 3D cell cultures (**Figure 3.14C**). Pre-extraction of microwell inserts in ethanol for 2 h and 24 h yielded aggregate diameters of 72 µm ± 16 µm and 83 µm ± 13 µm, respectively. During the culture of the aggregates for up to three days, changes in their size

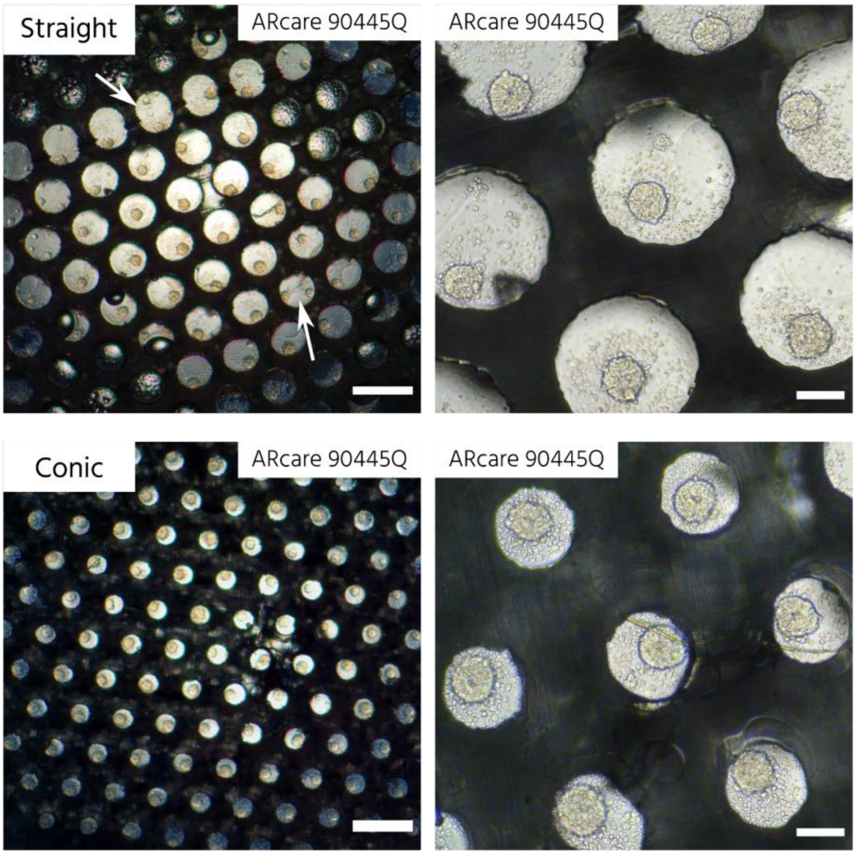

Figure 3.13 3D cell cultures of human iPSCs formed in microwell inserts 24 h after seeding. Both straight (top) and conic (bottom) microwells were suitable for the formation of cellular aggregates. While sometimes more than one aggregate would form in straight microwells (indicated by white arrows), conic microwells only contained single aggregates. Both microwell inserts were sealed with the double-side adhesive tape ARcare 90445Q. Left: brightfield image of the whole insert; right: close-up of one insert. Scale bars: 500 µm (left side), 100 µm (right side).

were used as an indicator for cellular viability (**Figure 3.14D**). The iPSC aggregates' size increased from 24 h to 48 h by 13% and 14% for the 2 h and 24 h pre-extraction conditions, respectively, indicating cell proliferation and viability. After 72 h, however, aggregates cultured in the inserts pre-extracted for 2 h in ethanol had reduced in size by 12% compared to day 2, while the diameter of aggregates of the 24 h pre-extraction condition increased by 2%. These results suggest that a pre-extraction of the 3D-printed microwell inserts for 24 h provided suitable conditions for 3D human stem cell cultures for a minimum of three days while cultures in 2 h pre-extracted microwell inserts showed compromised viability on the third day.

After having confirmed the suitability of 3D-printed microwell inserts for the formation and culture of human iPSC aggregates for up to three days, another experiment culturing the cells for up to seven days was conducted. To confirm their viability throughout the experiment, aggregate size was tracked by brightfield imaging. Additionally, live/dead stainings of the iPSC aggregates and viability assays based on the WST-8 assay were performed on days 1, 3, and 7 after seeding to evaluate whether 3D-printed microwell inserts allowed for these kinds of analyses. For this, inserts were pre-extracted for 24 h with ethanol and sealed with either PS

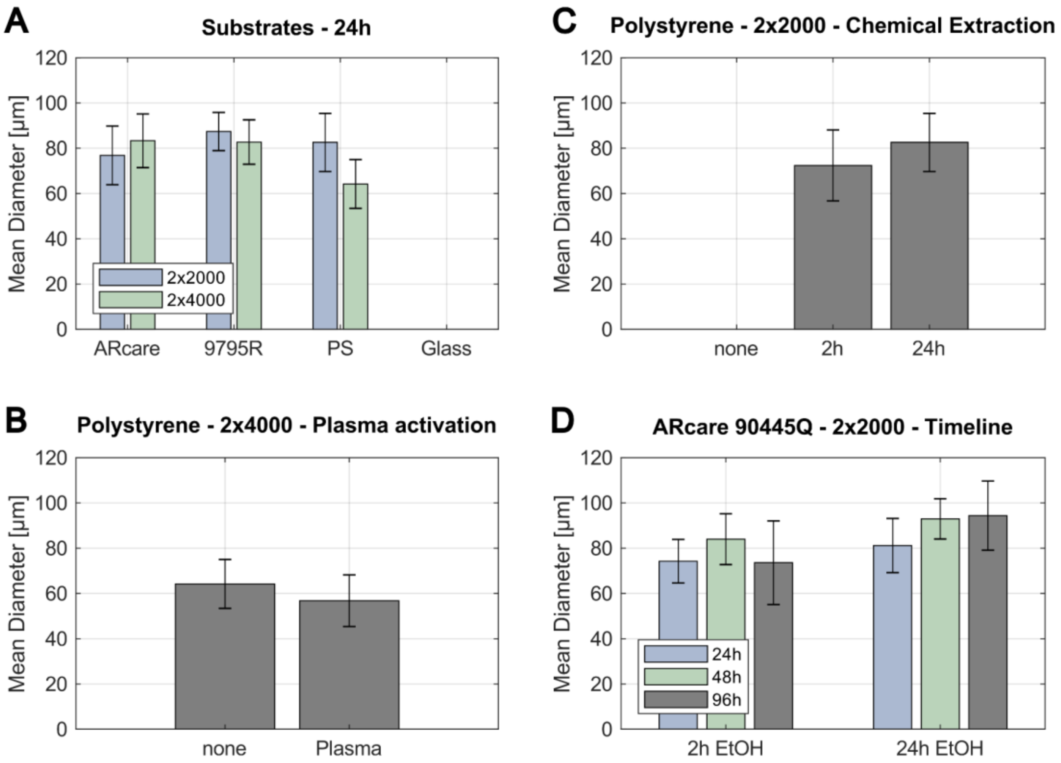

Figure 3.14 Mean diameters of human iPSC aggregates formed in 3D-printed microwell inserts. (**A**) Comparison of different substrates for sealing the microwell insert. Inserts had undergone UV post-exposure either with 2x2000 or 2x4000 flashes. PS - polystyrene. Shown are mean ± SD. *N* = 3 independently conducted experiments with three technical replicates. (**B**) Influence of plasma activation of the microwell insert's surface using air plasma (after UV exposure with 2x4000 flashes). Inserts were bonded to polystyrene. Shown are mean ± SD. *N* = 1 with three technical replicates. (**C**) Comparison between no, a 2 hour, and a 24 hour pre-extraction of microwell inserts in ethanol (after UV exposure with 2x2000 flashes) with a polystyrene (PS) substrate. Shown are mean ± SD. *N* = 2 for 2 h and 24 h, *N* = 1 for none, each with three technical replicates. (**D**) Evolution of the aggregate diameter over time for different pre-extraction periods in ethanol (after UV exposure with 2x2000 flashes). Inserts have been sealed with the ARcare adhesive foil. Shown are mean ± SD. *N* = 1 with three technical replicates.

(48-well plate) or the double-sided adhesive foil ARcare 90445Q. Human iPSCs were seeded as described above. Initial spheroid diameters were 80 µm ± 13 µm and 73 µm ± 12 µm for PS and ARcare sealed microwell inserts, respectively. Three days after seeding, cells had already grown larger than the opening of the microwells at the bottom such that measuring their diameter was not possible and thus omitted in the analysis. Live/dead staining of aggregates inside microwell inserts at the same time point revealed high autofluorescence of the 3D-printing material in the DAPI channel (405 nm), interfering with the live-cell signal in the same channel (**Figure 3.15A**). To circumvent this effect in the next analysis on day 7, as many aggregates as possible have been retrieved after staining and imaged inside a normal tissue culture plate. Likely due to the adhesive on the ARcare substrate, significantly fewer aggregates could be retrieved than from the inserts sealed with PS. Aggregates that have been retrieved showed good viability with few dead cells surrounding the aggregates (**Figure 3.15B**). These results were also confirmed by the WST-8 assay (**Figure 3.15C**). Compared to day 1, absorbance on day 7 was significantly ($p < 0.05$) increased. Absorbances were 8- and 10-fold the absorbance of day 1 for PS and ARcare substrates, respectively.

Overall, these results highlight the feasibility of the 3D-printed microwell insert for the formation and culture of human iPSC aggregates for up to seven days. The insert facilitated homogeneous aggregate sizes and ease of use. Analysis of aggregates inside the microwell insert for example by live/dead staining was difficult due to the high autofluorescence of the GR-10 printing resin. This needs to be optimized in the future for example by the use of custom-made resins or retrieval of aggregates for further downstream analyses. While the results shown here served as a proof-of-principle for monolithic microfluidic devices and application of these for 3D human stem cell cultures, further characterization of the 3D-printing material, as well as the cellular aggregates on a molecular and genotypic level, are required to ensure that there is no detrimental interference between both components.

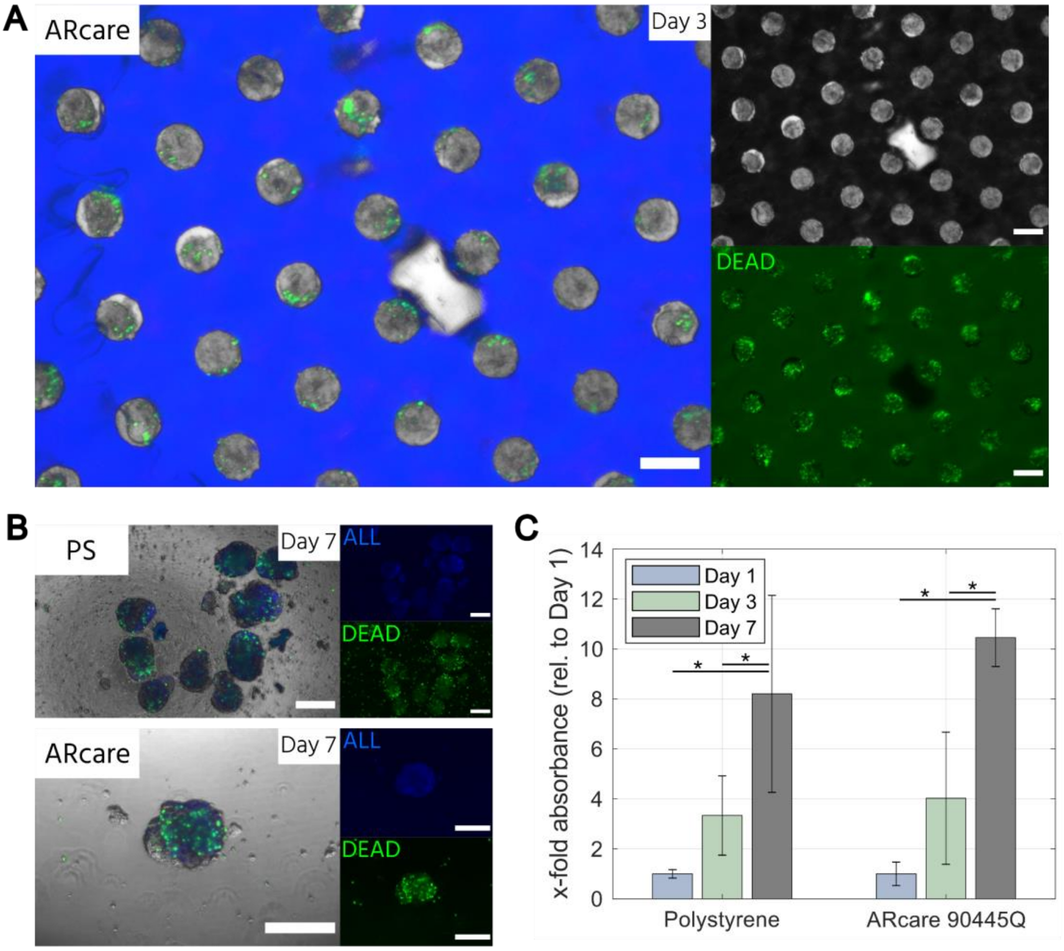

Figure 3.15 Viability of human iPSC 3D cell cultures in 3D-printed microwell inserts. (**A**) Live/dead staining of the aggregates on day 3 inside the insert sealed with ARcare 90445Q. High autofluorescence of the 3D-printed insert interferes with live cell signal (blue color). Scale bar: 200 µm. (**B**) Retrieved aggregates on day 7 after live/dead staining inside the 3D-printed inserts. iPSC aggregates showed good viability. Scale bars: 200 µm. (**C**) Mean absorbance measured by WST-8 assay relative to day 1 for polystyrene and ARcare substrates. $N = 1$ experiment with three technical replicates. $*p < 0.05$ using n-way anova.

4. Upscaling of pneumatic membrane valves for the integration of 3D cell cultures on-chip[a]

Microfluidic large-scale integration (mLSI) enables the automation of cell culture processes in a highly parallel manner, with precise spatiotemporal control of the cellular microenvironment.[21,62,178] mLSI platforms have been utilized for various cell culture processes, including high-throughput single-cell analysis[22], standardized stem cell differentiation[257], protein signaling analysis[177], conditional transcriptomics[189], and cell-to-cell interaction analysis[26]. To date, the majority of mLSI applications utilize traditional two-dimensional (2D) monolayer cell cultures, which provide robust, cost-effective, and repeatable access to cell screening assays. The channel design elements and corresponding chip production technology for the integration of 2D cell cultures rapidly evolved because the working dimensions of microfluidics (tens of microns) matched the needs of the 2D cell culture. With the increasing progression of cell culture technology, three-dimensional (3D) cell cultures have gained more attention because of their close similarity to *in vivo* tissue microenvironments.[114,258,259] Although mLSI chip platforms have recently been used for the analysis of 3D cell cultures on-chip[32], the technology is hampered because of a lack of production methods for scaling up flow channel heights above 100 µm and, thus, to sizes required for processing 3D cell cultures.

Multi-layer soft lithography[33] with polydimethylsiloxane (PDMS) has evolved as the preferred fabrication strategy for mLSI chips. It comprises photolithography processes for the fabrication of replica molds, which are subsequently used for casting separate chip layers with PDMS. However, photolithographic techniques only enable the production of rectangular channel profiles. To yield half-rounded cross-sectional shapes, photoresists were reflowed at increased temperatures in the post-processing step. Only positive photoresists can be subjected to a reflow process.[191] However, this material property is accompanied by several limitations regarding the chemical and thermal stabilities restricting achievable channel heights to a maximum of a few tens of micrometers in traditional processes.[34,192,194] Therefore, the fabrication of replication molds for complex mLSI chip platforms that incorporate various channel heights and cross-sectional geometries is limited by the inherent material properties of available photoresists.[34] The channel height limitation of the photolithography production method for mLSI chips has been addressed by manufacturing PDMS casting molds using *e.g.* backside photolithography[191], deflection of flexible membranes[192], or micro-milling[32]. However, design alterations, prolonged production times, and the availability of high-precision mills restrict these approaches. Thus, new production methods are required to enable the accessibility of mLSI technology for 3D cell culture, including organoids and whole tissue

---

[a] This chapter is based on the publication: "Compera, N., Atwell, S., Wirth, J., Wolfrum, B. & Meier, M. Upscaling of pneumatic membrane valves for the integration of 3D cell cultures on-chip. *Lab Chip,* **21**(15), 2986–2996 (2021)"[97]

structures with sizes higher than 50 µm.[34,191,192]

Additive production technology is an attractive alternative fabrication method for soft lithography replica molds[183,195,222] because of its high design flexibility, rapid prototyping, and achievable aspect ratios of up to 37:1[35]. Standard commercial 3D printers in the digital light processing (DLP) mode achieve *X/Y* pixel resolutions of 25– 40 µm, which makes them applicable for microfluidic mold fabrication[196,197,260] and direct printing of functional components, such as PMVs[183,199,210]. In contrast to the direct printing approach, 3D printing of molds provides numerous advantages of 3D printing technology while maintaining the desirable material properties of PDMS, such as biocompatibility and oxygen permeability. Early development has focused on the implementation of single-layered PDMS-based microfluidic devices with 3D-printed molds.[195,197] Despite all the technological advances achieved by DLP 3D printers, the mutual dependence on the building size and pixel resolution remains. While 3D printers, based on two-photon polymerization, exhibit sub-micrometer pixel resolution, their building sizes are low. In summary, for intermediate resolutions attributed to microfluidic chip technologies for 3D cell culture studies, optimization of 3D printing processes is required.

In this study, we developed an additive production process for fabricating mLSI casting molds. This process enables the upscaling of PMVs for channels with heights higher than 50 µm. To do this, we first established robust soft-lithography workflows to produce multi-layer mLSI chips using 3D-printed molds, including surface coatings. Surface staircase effects due to the inherent layer-printing processes with limited *Z* resolutions of DLP printers diminished the operating range of the PMVs. By systematically investigating grayscale light exposure for acrylate-based printing resins and a reflow process for wax-based molds, the staircase effect was reduced. The closing pressure and leakage rates of the PMVs fabricated from acrylate and wax molds were systematically characterized. In the following, the upscaled PMVs are exploited to design mLSI unit operations for the formation, trapping, retrieving, and fusing of 3D cell cultures.

4.1 Materials and methods

4.1.1 Master mold fabrication

Flow master molds were 3D-printed using a DLP stereolithography printer (Pico2HD, Asiga, Australia). Molds were printed with the commercially available resins PlasGRAY or SuperWAX (Asiga, Australia), with printing parameters (e.g. light intensity, exposure time) according to the manufacturer’s material file. The printing layer thickness and post-processing protocols were adjusted to achieve optimal PDMS molding results with each of the two resins. PlasGRAY molds were printed as negative molds (extruding channels) with a layer thickness of 10 µm. For post-processing, the PlasGRAY parts were cleaned with isopropyl alcohol and cured in a flash-curing device (Otoflash G171, NK-Optik, Germany), according to the manufacturer's recommendations.

SuperWAX molds were printed as positive molds (intruding channels) with a layer thickness of 25 µm, which was the minimal possible layer thickness for the resin. The SuperWAX molds were cleaned to remove the residual uncured resin by sonication in prewarmed isopropyl alcohol (30–35 °C) for 20 s, followed by rinsing with distilled water. Once dried, the molds were placed on a hotplate set to 50 °C for 3 min to reflow the channels. Subsequently, a negative mold was manufactured by casting Durosil® (Detax GmbH & Co. KG, Germany) using a SuperWAX mold. Durosil silicone was cured for 24 h at room temperature before being released from the SuperWAX mold.

Master molds for the control layer of the mLSI chips were fabricated according to the standard SU–8 (SU–8 3050; Microresist Technology, Germany) photolithography protocols.[33] To prevent PDMS adhesion onto PlasGRAY, Durosil®, or SU-8 molds, their surfaces were permanently coated with CYTOP™ (AGC Chemicals, Japan), which is an amorphous inert fluoropolymer. Molds were either spin-coated (SU-8 molds) or dip-coated (Durosil® and PlasGRAY molds) on the surface with a thin film of Cytop (<1 µm). The Cytop-coated SU-8 mold was heated to 160 °C for 1 h, while the Cytop-coated PlasGRAY and Durosil® molds were incubated on a hotplate for 8 h at 80 °C to evaporate the Cytop solvent.

4.1.2 Chip fabrication

All mLSI platforms were fabricated using multilayer soft lithography[33] using 3D-printed flow and SU-8 silicon control molds. The upper flow layer was manufactured by casting a thick PDMS (Sylgard® 184, Dow Corning, MI, USA) layer (ratio 5:1 of base material to curing agent) onto the 3D-printed mold, while the lower control layer was fabricated by spin-coating a thin PDMS layer (20:1 ratio) onto the SU-8 mold. Both layers were partially cured for 20 min at 80 °C. The flow layer was released from the mold and aligned with the control layer. The assembled mLSI device was post-baked for 45 min at 80 °C to enable off-ratio PDMS bonding. Finally, the mLSI device was sealed with a cover glass after oxygen plasma activation and baked for another 60 min at 80 °C.

4.1.3 Surface measurements

Surface measurements on 3D-printed flow master molds were performed using a confocal laser scanning microscope (VK-X250; Keyence, Japan). Confocal images were then analyzed using MATLAB (R2019a; MathWorks, MA, USA) to obtain the flow channel profiles.

4.1.4 PMV design and characterization

The PMVs consisted of two orthogonally intersecting channels separated by a thin PDMS membrane. For this purpose, the PMVs were designed in the push-up configuration. While channels on the upper flow layer had widths and heights of 400 and 200 µm (aspect ratio height to width of 1:2), the channels on the lower control layer had widths and heights of 600 and 100 µm, respectively. The PMV closing pressures decrease with increasing channel cross-section.[178] Therefore, the control channels are scaled by a factor of 1.5 compared to the flow channels. The closing pressures of the PMVs were determined by measuring the fluid flow rates under the defined driving pressures. The control channel lines were filled with water and connected through tubing to individual solenoid valves. The solenoid valves were pressurized with defined air pressures (p_{ctrl}) between 0 and 200 kPa. The flow inlet ports were connected through Tygon tubing (ND 100-80; Proliquid, Germany) to gas-tight bottles filled with deionized water. Each water bottle was pressurized with air (p_{fluid}) using a flow control unit (Flow EZ$^{\mathrm{TM}}$; Fluigent, France). The outlet port was connected to an 80-cm-long tubing (inner diameter: 0.508 mm), which was maintained at atmospheric pressure. The PMV closing pressure was determined by incrementally increasing p_{ctrl}, typically by 50 kPa. Concomitantly, the flow rate in the fluid channel was measured using two different methods to screen a large range of flow rates. Flow rates ≥ 20 µL/min were measured using a flow sensor (Flow Unit L, Fluigent). Flow rates < 20 µL/min were determined by measuring the distance traveled by the meniscus of the liquid in the connected tubing for a specific period. The corresponding volumetric flow rate was then calculated using $Q = \frac{dA_{Tube}}{t}$. Here, Q denotes the flow rate (µL/min), d is the distance traveled by the liquid [mm], A_{Tube} is the cross-section of the tubing (0.20268 mm^2), and t is the time (typically 30 min) between the start and end of the measurement. The readout accuracy of the flow sensor was ±1.5 µL/min, while the readout error of the distance measurement was calculated relative to the flow rate ($\Delta\, Q=0.04*Q+0.002$ µL/min), ranging from 0.002 µL/min to 0.8 µL/min for flow rates from 0 µL/min to 20 µL/min. The measurements of each valve were performed independently, at least in triplicate ($N = 3$). Before the start of each measurement, the PMVs were opened and closed at least once to avoid bias due to the remaining pressure in the device.

4.1.5 Flow analysis of the mLSI cell trapping unit

Flow characterization of the cell trapping unit was performed with the help of a particle tracking experiment. Therefore, 2.55 µm polystyrene beads (PS-F-B237-1; microParticles GmbH, Germany) were flushed through the unit chamber of the mLSI chip. The trapping valve pressure was increased incrementally, typically in steps of 6.9 kPa, and the particle flow was recorded on an AxioObserver, with a frame rate of 728 fps. Prior to each measurement, the PMVs were opened and closed at least once to avoid bias due to the remaining pressure in the device. A constant fluid forward pressure of 25, 35, or 45 mbar was applied during the measurements. Recorded data were subsequently analyzed in ImageJ (v1.52p), using the TrackMate[261] plugin and exported to MATLAB (R2019a; MathWorks, MA, USA) for visualization and flow rate calculations.

4.1.6 3D cell culture on-chip

Prior to use in cell experiments, the chip was coated with 10% Pluronic F127 (Sigma Aldrich, MO, USA) for at least 24 h to minimize cell attachment to the PDMS. The cell culture medium was introduced 30 min before seeding to allow for equilibration. To seed cells, 3–5 × 10^6 cells in approximately 50 µL of the respective culture medium were transferred as a single-cell suspension on-chip. For the fibroblasts, we first seeded mCherry-labeled NIH3T3s in formation chamber row 1, followed by actuation of the trapping valves in row 1 and a medium rinse of all fluidic channels containing the cell material. We then seeded the Venus-labeled NIH3T3s in row 2, actuated these trapping valves, and cleaned all channels of the remaining, non-trapped cells. When hiPSCs or hASCs were used, we seeded them successively in formation chamber rows 1 and 2, before actuating the trapping valves and rinsing all channels with medium. The control pressure for the trapping valves was set to 207 kPa to minimize cell loss during rinsing. Trapped cells were allowed to rest and aggregate for 4 h before the first feeding cycle. During the first feeding, the trapping valve (140–170 kPa) and fluid forward pressure (ranging from 25 to 45 mbar) were adjusted manually based on visual inspection of the cell-trapping site to ensure fluid passage while keeping the spheroid trapped. Thereafter, these parameters were kept constant, and cells were automatically fed every 2–4 h for 10 s, depending on the cell type, using a custom-written MATLAB script. Media bottles were replenished every 24 h. Fluorescently labeled 3T3s were cultivated in DMEM + 10% fetal bovine serum (Corning, NY, USA). Human iPSC culture media (mTeSR^{TM} Plus (StemCell Technologies, Canada) and 1% penicillin-streptomycin) was supplemented with ROCK inhibitor (Y-27632; Apexbio Technology, TX, USA) for the first 24 h, but removed for subsequent maintenance. Human adipose-derived adult stem cells (hASCs) were seeded and maintained in a subcutaneous preadipocyte growth medium (PM-1; ZenBio, NC, USA).

4.1.7 Microscopy and image analysis

Bright-field images were acquired with 2.5× and 10× (Plan-Apochromat) objectives on a Zeiss AxioVert. An epifluorescent microscope (AxioObserver, Zeiss) was used to record the fluorescent images. Image analysis and statistical evaluation were performed using ImageJ and MATLAB. Values are represented as mean ± SD for three independent experiments ($N = 3$) unless stated otherwise.

4.2 Results and discussion

4.2.1 Upscaling PMVs by soft lithography using 3D-printed master molds

A central requirement for soft lithography using 3D-printed molds is to enable the curing and release of PDMS from mold surfaces. During the direct soft-lithography prototyping of PDMS, using 3D-printed molds, contact inhibition of PDMS curing was observed in this study and previous studies.[36,197,219] This problem originates from the non-crosslinked monomers on the surface and in the bulk of the mold.[197,203] Postprocessing steps, including bulk material heating and temporary surface coating with anti-adhesive agents, improved the soft lithography of PDMS using the 3D-printed molds. The anti-adhesive coating did not fully overcome the PDMS release problem because molds require frequent re-coating.[196,219,220] Thus, we evaluated a simple fluoropolymer surface coating to overcome the contact inhibition of PDMS curing on 3D-printed parts. CYTOP^{TM}, an epoxy-based amorphous fluoropolymer, has been developed for coating silicon wafers to enable long-term usage [262] and has been successfully applied as a releasing agent for PDMS.[263,264] Plasma activation and subsequent dip-coating of the 3D-printed molds in a 2% solution of CYTOP^{TM} (CTL-809M diluted in CT-SOLV180) increased the water contact angle, compared to the non-coated surface from 76° to 88° (**Figure A.2**). The increased surface hydrophobicity of the CYTOP-coated 3D-printed molds enabled complete polymerization and easy removal of the PDMS casts. Notably, the first PDMS cast from the CYTOP-coated mold could not be plasma-bonded. Repetitive usage of the same mold for PDMS casting and demolding up to 30 times led to no noticeable wear-off of the surface coating.

The second challenge in manufacturing mLSI chips using 3D-printed molds is the inherent layering nature of DLP printers. The flow channels on mLSI chips require a half-rounded channel profile to be closed by PMVs. DLP printers applicable to microfluidics exhibit *Z* resolutions of approximately 5–50 µm.[199] At these *Z*-printing resolutions, the channels on the molds exhibit a step-like rather than a perfectly half-rounded profile (**Figure 4.1A**). Printed features are discretized in slices with defined thicknesses, resulting in the staircase effect on the printed feature surface.[36,203,220,262] To investigate whether the staircase effect impaired the PMV function (**Figure 4.1B**), we produced a two-layered microfluidic chip with one straight flow channel and three consecutive PMVs (width: 400 µm, length: 600 µm) in the push-up configuration. Bright-field images of the valve compression area at control pressures of 50, 100, and 200 kPa are shown in **Figure 4.1C**. At 50 kPa, the valve membrane closed the flow channel only at the center of the compression area (**Figure 4.1C**, indicated by the red arrow). Meanwhile, at 200 kPa, only thin lines at the sidewalls (**Figure 4.1C**, indicated by white bars) of the channel remained. These lines indicate openings induced by the staircases on the channel surface. A similar observation during the production of sieve valves has been reported, which are PMVs incompletely closing flow channels with a squared channel profile.[21]

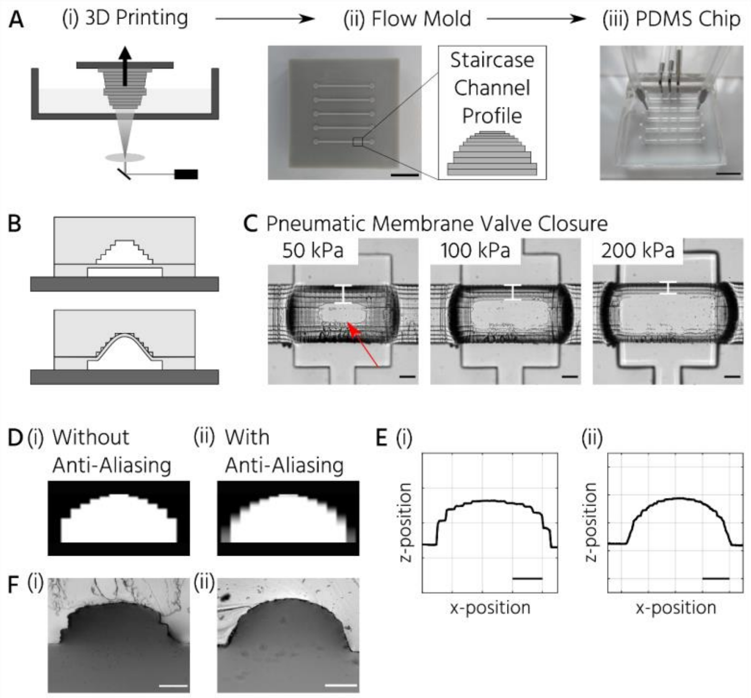

Figure 4.1 Optimization of 3D printing workflows for the upscaling of PMVs, using an acrylate-based printing resin. (**A**) PMV fabrication process using a 3D-printed negative mold for soft lithography. The inherent layering of the 3D printing process causes an approximation of rounded features on the flow mold, leading to a staircase effect on the flow channel's surface. Scale bars: 5 mm. (**B**) Open (top) and closed (bottom) states of a push-up valve for the staircase flow channel profile. (**C**) Valve closure on a staircase flow channel for increasing control pressures. The red arrow and white bars indicate sufficient and insufficient membrane sealings, respectively. Scale bars: 100 µm. (**D**) Slicing images of an extruding half-rounded flow channel (i) without and (ii) with grayscale light exposure (anti-aliasing). (**E**) Surface profile of the flow channel on a mold printed (i) without or (ii) with anti-aliasing. Scale bars: 100 µm. (**F**) PDMS channel cross sections casted from molds that were printed (i) without and (ii) with anti-aliasing. The staircase effect is significantly decreased on molds printed with grayscale light exposure. Scale bars: 100 µm.

To investigate and mitigate the staircase effect on PMV closure, we used two strategies: (1) reducing the staircase edges by grayscale light exposure (anti-aliasing) during the 3D printing process[228,265] and (2) an alternative wax-based printing resin, which can be reflowed in a postprocessing step analogous to positive photoresists in traditional photolithography[178], to obtain perfectly rounded flow channels. Anti-aliasing is a method of encoding individual pixels of a DLP printing slice in grayscale values (**Figure 4.1D** (ii)) instead of the black and white pixels (**Figure 4.1D** (i)). This method leads to a rounding effect on the features during printing. Using anti-aliasing, the flow channel surface was significantly smoothed on the 3D-printed molds (**Figure 4.1E**). Consequently, the staircase effect was minimized (**Figure 4.1F**).

An alternative manufacturing process for upscaled PMVs and removal of the staircase effect is to implement a reflow process analogous to the post-processing of positive photoresists. The acrylate-based printing resin exhibits a glass transition temperature of 84 °C. However, post-backing acrylate 3D-printed parts above their glass transition temperature led only to warpage and deformation of the parts without the reflow of staircases. Therefore, we evaluated the performance of the wax-based printing resin for the fabrication of PDMS replica molds. Wax resins have melting temperatures between 40 and 60 °C (SuperWAX, t_{melt} = 50 °C) and are, thus, applicable for a reflow process.

To test this approach, we printed a negative mold with a wax resin (SuperWAX, Asiga) and then placed the wax molds (total thickness: 3 mm) for 3 min at 50 °C onto a glass slide to reflow the channels (**Figure 4.2A** (i)–(ii)). Therefore, the printed features faced upward. Indeed, the reflow process resulted in half-rounded channel geometries without an apparent staircase effect (**Figure 4.2B**). However, casting of PDMS using the 3D-printed wax molds was not possible because of the contact curing inhibition reaction between the wax and PDMS. The CYTOP coating of the wax mold did not overcome this problem, presumably owing to the rapid exchange of wax molecules between the bulk and surface areas. Therefore, a double-casting process was introduced (**Figure 4.2A**). First, a positive mold was printed using SuperWAX. The mold was thermally reflowed to remove the staircase effect (**Figure 4.2C**) and then replicated with silicone (Durosil®), which was cured on the wax mold at room temperature for 24 h. The negative silicone mold was then coated with CYTOP and subsequently used to cast the PDMS.

Next, we characterized and compared the closing behavior of upscaled PMVs fabricated using either the anti-aliased acrylate-based or reflowed wax-based molds. Bright-field images of the valve compression area acquired with an increase in the actuation pressure are shown in **Figure 4.3A**. While the PMVs fabricated from the reflowed wax mold visibly closed the flow channel at 50 kPa, the PMVs fabricated from the anti-aliased acrylate mold closed the flow channel at a pressure of 200 kPa. The pressure dependence of the PMV closing state was determined using flow rate measurements (**Figure 4.3B**). The mean flow rates within an

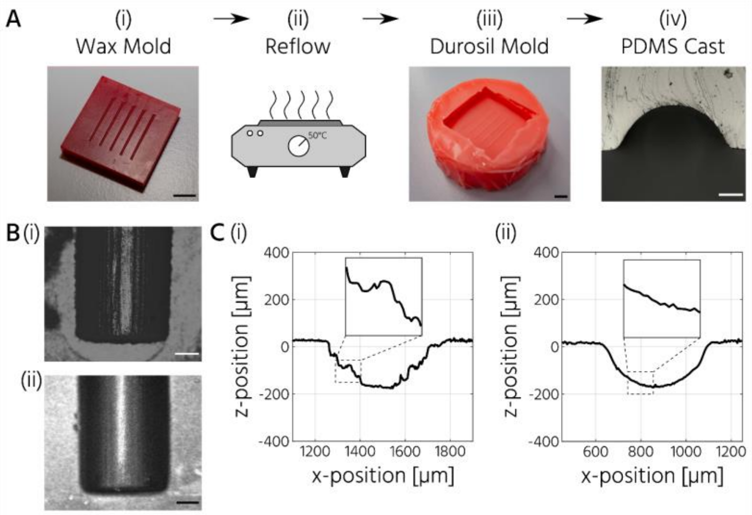

Figure 4.2 Generation of flow channels without staircase effect using 3D-printed wax molds. (**A**) Double casting workflow to obtain PDMS replicate from 3D-printed wax molds: (i) 3D-printed SuperWAX mold with intruding flow channels. (ii) Reflow of the mold at 50 °C to remove the staircase effect. (iii) Durosil® negative of the reflowed wax mold. (iv) Cross-section of the PDMS layer cast using the Durosil® mold. Scale bars: 5 mm (i, ii), 100 µm (iv). (**B**) Extruding flow channel on a 3D-printed wax mold (i) before and (ii) after the reflow. Scale bars: 100 µm (**C**) Profile of an intruding flow channel (i) before and (ii) after the reflow of the SuperWAX mold. The thermal reflow step removed the staircase effect on the casting mold.

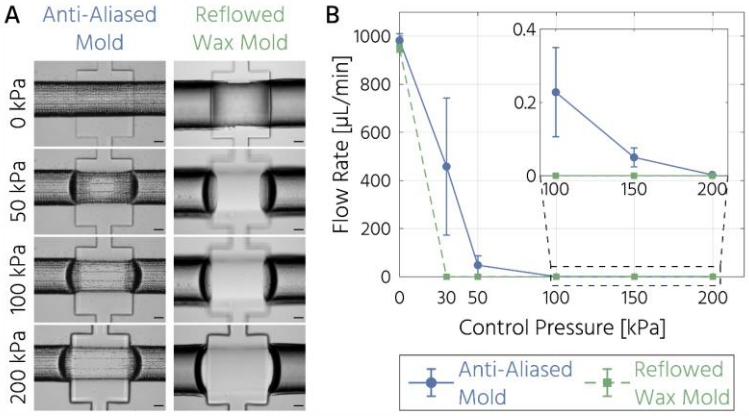

Figure 4.3 PMV closing pressure characterization. A fluid forward pressure of 14 kPa was applied to characterize the rates of flow through PMVs, which were either fabricated by a 3D-printed anti-aliased flow mold or a reflowed wax mold. (**A**) Bright-field images of the closure of both valves for applied control pressures of 0, 50, 100, and 200 kPa. Scale bars: 100 µm. (**B**) Flow rates through PMVs for increasing control pressures.

unrestricted channel cast from an anti-aliased and reflowed wax mold at a driving pressure of 14 kPa were 982 and 949 µL/min, respectively. These flow rates evoke flow velocities of about 250 mm/s in the fluidic channel, which are at least one order of magnitude higher than those generally required for mLSI cell culture devices.[101,266,267]

The closing pressure of the PMVs for a flow channel with a semi-half-round profile, cast from the reflowed wax mold, was 30 kPa at a counteracting flow pressure of 14 kPa. This measured value is slightly higher than the theoretical closing pressure, which can be approximated using a thick spring model.[178] Assuming a Young's modulus of 750 kPa[268] for the PDMS membrane (10:1 ratio), the thick spring model predicts a closing pressure of 20.5 kPa. The slight offset can be explained by the boundary conditions of the model, which was developed using the data of mLSI chips with smaller channel dimensions.[178] In comparison, the PMVs actuated with a control pressure of 30 kPa on channels with a minimized staircase profile only decreased the flow rate by a factor of 2 (458 µL/min; **Figure 4.3B**) but did not reach a closed state. Only upon increasing the control pressure to 200 kPa, a closing state with a reduction in the flow rate by a magnitude of 10^5 compared to the open state was achieved. Thus, at actuation pressures of 200 kPa or higher, the leakage of the PMV fabricated from an anti-aliased mold is negligible, and the valve can be considered fully closed.

4.2.2 PMV-assisted formation of 3D cell cultures on mLSI chip platforms

To demonstrate the integration of the upscaled PMVs for 3D cell culturing on mLSI platforms, we first designed and characterized a functional unit cell for the formation, culturing, and trapping of 3D cell cultures. Unit cells can be arrayed for parallel processing on mLSI chips, with standard multiplexing design elements. Pneumatic structures have been exploited for the formation, culturing, and trapping of 3D cell cultures before. The prominent examples for this purpose are U-shaped PMVs[83,269], microwells[270], or bar-shaped gate structures[85]. Common in all designs is that they either show a complex operational process or have low application flexibility upon integration into multilayered PDMS platforms. To offer an alternative workflow for handling 3D cell cultures on mLSI, the sieve-like closing behavior of PMVs on channel profiles, with residual staircase profiles, when actuated with pressures below the closing state has been exploited. **Figure 4.4A** shows the working principle of the unit cell design. The unit cell comprises three bifurcating flow channels and two upscaled PMVs for separating a cell culture volume of 0.1 µL. While the two side channels had widths and heights of 100 µm and 50 µm, respectively, the center channel had a width and height of 300 µm and 200 µm. The cell culture volume of the unit cell and the cell density of the seeding solution determine the diameter of the resulting 3D cell culture. Here, to avoid quiescent or necrotic zones in the center[271,272], the unit cell structure was designed to initiate 3D cell cultures with diameters below 200 µm. For the 3D cell culture formation step, a high-density single-cell suspension (6 x 10^7 cells/mL) is flushed through the unit cell until the center channel is filled. Subsequently, the trapping PMVs are fully closed, and non-trapped cells in the side channels are rinsed out. 3D cell cultures are then formed by self-aggregation. For the long-term culturing process, the control pressure of the PMVs is decreased, and the sieve-like behavior of the trapping valves enables feeding under low shear stress conditions. The open state of the PMVs allows for retrieval of the 3D cell culture.

In a first step, the flow velocity profile across the cell-trapping site was measured by particle tracking to characterize the unit cell design. **Figure 4.4B** shows the flow profile within the trapping site at changing actuation pressures of the trapping valves and constant fluid pressure. In the PMV open state, a fluid forward pressure of 25 mbar or 45 mbar evoked a mean flow rate at the cell trapping site of 0.6 µL/s or 0.7 µL/s, respectively (**Figure 4.4C**, (i)). At a control pressure of 140 kPa, the flow rate was reduced by approximately 40% (**Figure 4.4C**, (iii)). The closed state was reached at a closing pressure of above 200 kPa.

Thereafter, the homogeneity and reproducibility of the 3D cell culture formation process in the unit cell were investigated using three different cell types: NIH3T3 fibroblasts, human iPSCs, and hASCs. All used cell types showed self-aggregation within the first 2–4 h after seeding (**Figure 4.4D**) and formed a compact, spherical morphology with distinct borders within 24 h. Upon reducing the actuation pressure of the trapping PMV (< 170 kPa), dead cells were removed, and cell feeding was achieved with the reinstated flow. This process resulted in few to no residual dead cells inside the trapping region (**Figure 4.4D**, **E**).

With the chosen channel dimensions, 3D cell cultures of NIH3T3s cells, hiPSCs, and hASCs have been produced reliably. A boxplot of all spheroid sizes across several technical and biological repetitions is presented in **Figure 4.4F**. The mean diameter of the NIH3T3 spheroids was 125 ± 33 µm (mean ± standard deviation). In comparison, hiPSC and hASC spheroids exhibited mean diameters of 136 ± 22 µm and 124 ± 15 µm, respectively. In addition to the somewhat larger interquartile range for NIH3T3s, the inter-chip variation of the achieved 3D

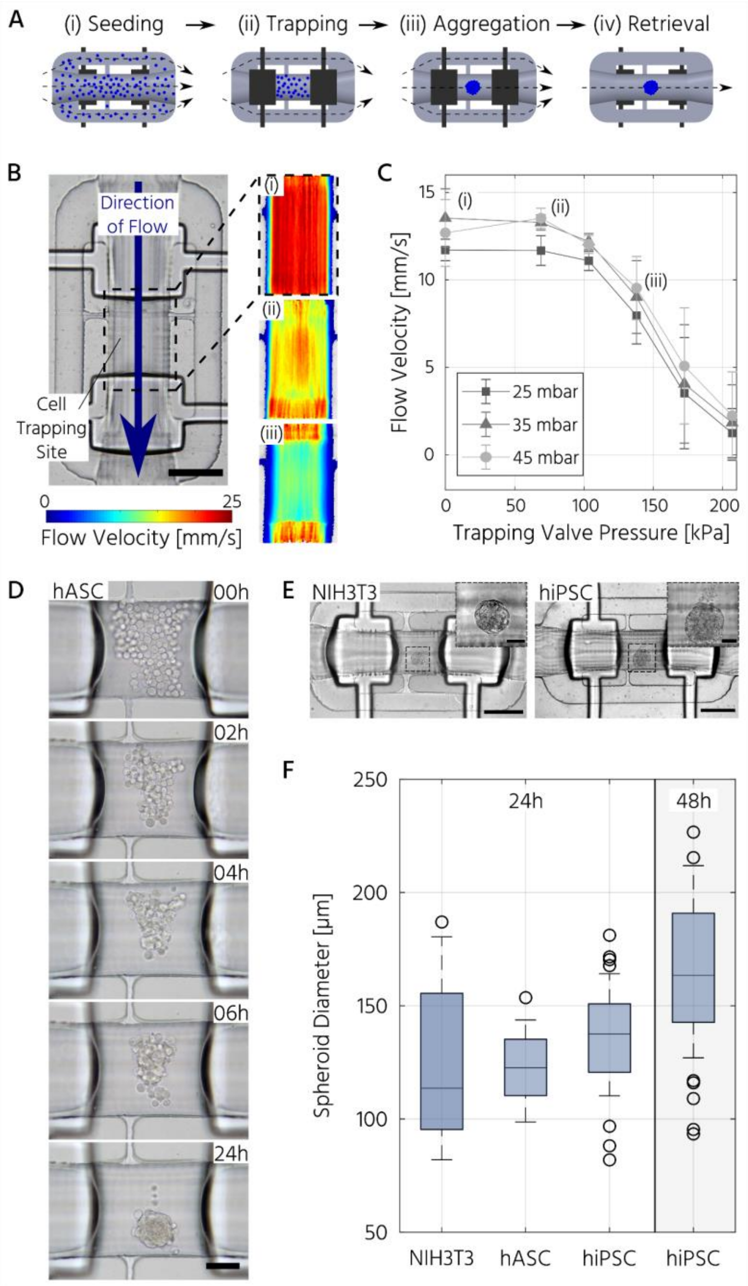

Figure 4.4 PMV-assisted formation of 3D cell cultures on mLSI chip platforms. (**A**) 3D cell culture formation principle: Single cells are introduced and trapped upon actuation of the two trapping valves. Rinsing of residual cells on the sides ensures localized 3D cell culture formation in the trapping region, and then cells start to self-aggregate. To release the formed aggregate, actuation of the trapping valves is stopped. (**B**) Flow analysis of the cell trapping site by particle tracking velocimetry (PTV). Varying the control pressure of the trapping valves between (i) 0, (ii) 69, and (iii) 138 kPa allows for adjusting the flow velocity profile within the cell trapping site. Scale bar: 250 µm. (**C**) Flow rate inside the trapping region for increasing control pressures of the trapping valves and varying fluid forward pressures based on the PTV data. (**D**) Representative brightfield images of the self-aggregation of human adipose-derived adult stem cells (hASC) inside the trapping region for different time points after seeding. Scale bar: 100 µm. (**E**) Brightfield images of 3D cell cultures of NIH3T3s and human-induced pluripotent stem cell (hiPSC) 24 hours after seeding. Scale bars: 250 µm, 50 µm (insets). (**F**) Diameters of 3D cell cultures of different cell types formed on-chip 24 and 48 hours after seeding. The middle line in the boxes marks the median diameter, while the bottom and top edges of the boxes indicate the 25th and 75th percentile values. Outliers (> 1.5 × interquartile range) are presented as circles.

cell culture size, 24 h after seeding, was less than 4% and 15 % for the hiPSCs and hASCs, respectively. Further, extending the culture process for the iPSC led to an increase in the 3D cell culture by approximately 20% within the next 24 h, demonstrating cell growth and viability (**Figure 4.4F**). In summary, we designed a functional unit cell for arraying on an mLSI platform to form 3D cell cultures reliably with homogeneous sizes.

4.2.3 Fusion of 3D cell cultures on an mLSI chip

Upon successfully characterizing the unit cell operation for 3D cell cultures, we built an mLSI platform, in which the unit cell was arrayed eight times. The layout of the platform is shown in **Figure 4.5A** (left side). The primary function of the chip was to form 3D cell cultures in the first step and merge two different 3D cell cultures in the second step. For the implementation of the two operational steps, the unit cell was arrayed in a 3 × 8 (row/column) matrix format. While unit cells in the first two rows were allocated for the formation and cultivation of individually addressable 3D cell cultures, unit cells in the third row were allocated for the fusing operation of 3D cell cultures generated in the upper rows of the same column (**Figure 4.5A**, right side). A multiplexer structure was used to address single-column elements, and individual PMVs were used to address the row elements.

To prove the *in vitro* fusion operation on the chip platform, two fluorescent reporter cell lines were used: mCherry- (red) and Venus-labeled (green) NIH3T3 cells. For cell seeding and formation of the 3D cell cultures, the cells were separately introduced into the first and second-row elements (**Figure 4.5B**, (i)). Further, 24 hours after seeding, each column was addressed successively to flush the 3D cell culture sequentially into the unit cell chamber of the third row (**Figure 4.5B**, (ii)-(iii)). To trap both 3D cell cultures, the entry-trapping PMV was opened while maintaining the PMV at the outlet side in a sieve-like valve state (actuation pressure < 170 kPa). **Figure 4.5C** highlights the progression of fusion, based on one representative example. All 3D cell cultures fused within 24 h and exhibited an elongated elliptical morphology over the time frame of 65 h.

Cell aggregate fusion has been described by the differential adhesion hypothesis wherein the individual surface tensions of the 3D cell cultures in pairs determine cellular rearrangement.[273] Based on this, the fusion process has been characterized by an analogy to the coalescence of highly viscous liquid droplets, where coalescence is driven by surface tension and resisted by viscosity.[271,272,274] The progression of fusion can then be quantified by the evolution of the interfacial area (πr^2) between the fusing partners, normalized by the initial average cross-sectional area of the aggregates (πR^2) over time[274], which is the squared ratio of the radii $(r/R)^2$. Additionally, morphological changes during fusion have been characterized by the overall aggregate length.[275,276] As the aggregate length decreased, the squared ratio of the radii increased during the 3D cell culture fusion process (**Figure 4.5D**). Both parameters converged to their respective minimal/maximal levels after 60 h. This slow rate is in accordance

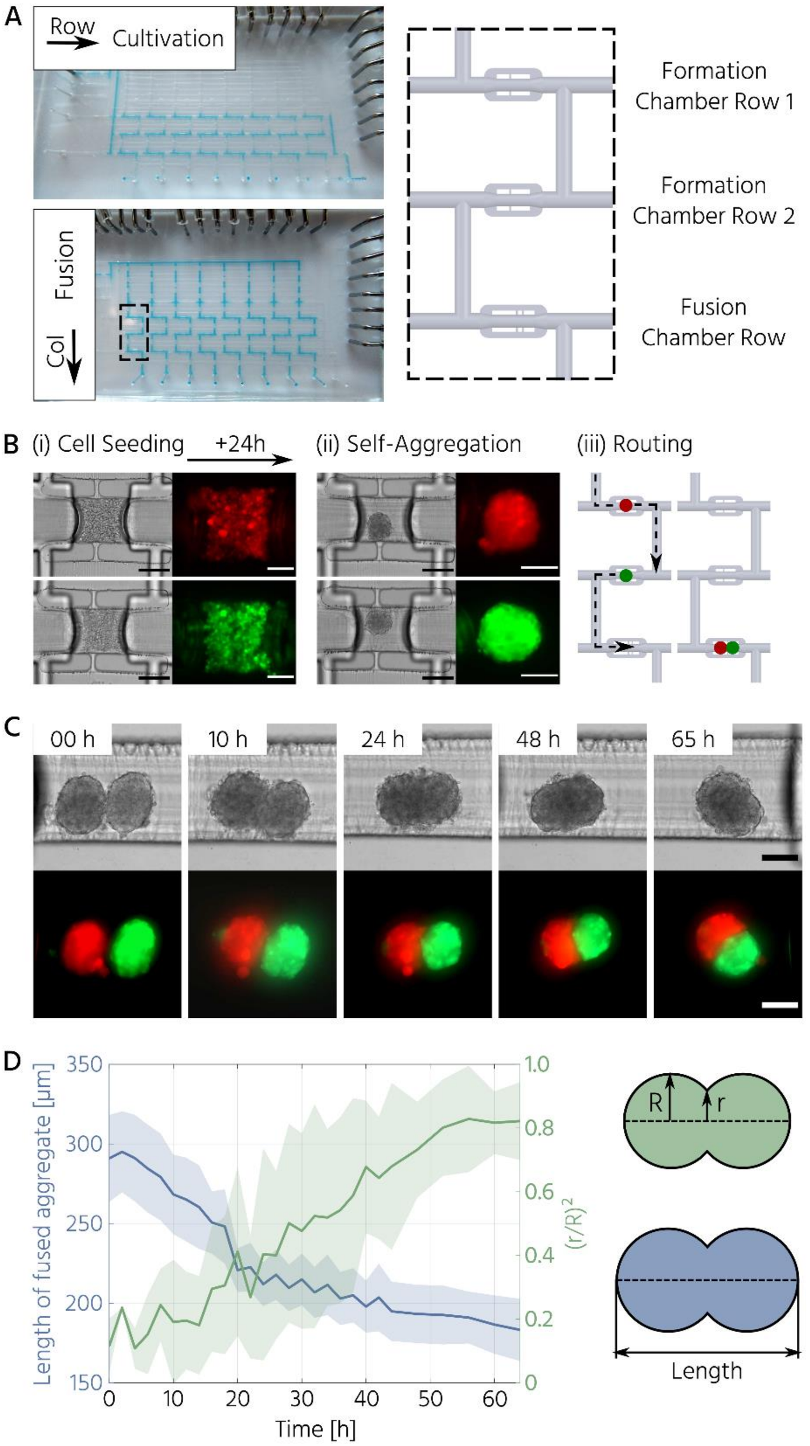

Figure 4.5 mLSI chip platform for the fusion of 3D cell cultures. (**A**) Microfluidic device that can be operated row-wise for cultivation or column-wise for fusion. The right picture depicts one of eight parallel columns. (**B**) Formation and cultivation of two differently fluorescently labeled NIH3T3s before on-chip fusion. (i) Seeding of mCherry-labeled (red, 1st row) and Venus-labeled (green, 2nd row) NIH3T3 fibroblasts. (ii) Within 24 hours, cells self-aggregated. (iii) After both 3D cell cultures were formed, they were flushed into the fusion chamber (3rd row). Scale bars: 200 µm (brightfield images), 100 µm (fluorescence images). (**C**) Progression of the fusion of fluorescently labeled NIH3T3s. Scale bars: 100 µm. (**D**) Quantification of morphological changes during the fusion of 3D cell cultures. The overall length of the fused aggregates (blue curve) as well as the squared ratio of the radii $(r/R)^2$ (green line) are plotted as a function of time. The neck radius r is normalized by the average radius R of the 3D cell culture in pairs. Shown are the mean (darker line) and standard deviation (lighter area) for both parameters of one experiment across all on-chip replicates.

with the values determined for fusing 3D cell cultures of dermal fibroblasts[276] and chondrocytes[275] and illustrates high internal cellular cohesive forces. Notably, the two labeled NIH3T3 cell populations did not mix within the given time frame. This finding is consistent with the differential adhesion hypothesis as both populations arise from the same cell type and should, thus, have similar surface tension.

Overall, upscaled PMVs ensured unrestricted and non-destructive handling of 3D cell cultures. In the future, mLSI applications that comprise interaction studies of various heterogeneous tissues to assist in *in-vitro*-modeling of more complex developmental processes, such as human embryogenesis[114], organogenesis[50], and brain development[277] are envisioned.

5. Adipose microtissue-on-chip: A 3D cell culture platform for differentiation, stimulation, and proteomic analysis of human adipocytes[b]

Adipose tissue is linked to a multitude of metabolic and endocrine functions in both healthy and diseased states, including adipokine and cytokine secretion, and lipid storage and release. In obesity, adipocyte hypertrophy and hyperplasia are the main drivers for the expansion of white adipose tissue, which leads to alterations in adipokine secretion and eventually disrupts the whole-body metabolism.[278,279] However, the underlying molecular and functional mechanisms of adipose tissue in normal and pathological conditions are still a matter of debate. For longitudinal studies, it would be of substantial interest to engineer *in vitro* adipose tissues to model patient intervention studies. The murine preadipocyte cell line 3T3-L1[280], primary adipocytes[104,281], and human adipose tissue-derived stem cells (hASCs)[52,282] have been used to replicate the physiology of fat tissue *in vitro*. hASCs are a convenient choice, as they are easy to maintain in routine cell culture formats, are proliferative, model depot-specific subtypes of adipocytes, and provide good translatability[281,283]. To obtain mature fat tissue, hASCs must be differentiated into adipocytes before they display the phenotypic characteristics of their *in vivo* counterparts. Notably, *in vitro*-generated adipocytes resemble a premature adipose cell type, as indicated by their multilocularity, smaller lipid droplet diameters, and lower adipokine secretion.[281] However, this cell type is preferred for *in vitro* engineering because of the obstacles encountered in handling mature primary adipocytes with their high buoyancy and mechanical fragility.[284] 3D cell culture formats, instead of traditional monolayer culture [136,285,286] have been suggested to enhance the maturation and differentiation of hASCs.[52,287,288] Compared with monolayer culture formats, 3D cell cultures represent the organotypic microenvironment of native adipose tissue.[282] For 3D culture, approaches such as embedding hASCs in Matrigel[289] or other hydrogels[52,281], low-attachment well plates[282], hanging drops[57], magnetic levitation systems[290], permeable membranes[291], and microfluidic systems[104,292] have all been exploited.

Microfluidic techniques for modeling adipose tissue physiology *in vitro* have recently gained attention as they offer dynamic control of chemicals in the cell microenvironment during long-term differentiation[104], a reduced surface-to-volume ratio, and the possibility of automation of complex culture conditions. The integration of functional adipocytes or adipose microtissue-on-chip allows to assay insulin response[198,293], sampling of glycerol secretion at high temporal resolution[294,295], and the mimicking of interstitial flow conditions.[52] The majority of on-chip integrated adipose tissues use scaffolding hydrogels, which closely mimic the native

---

[b] This chapter is based on the publication: "Compera, N., Atwell, S., Wirth, J., von Toerne, C., Hauck, S., & Meier, M. Adipose microtissue-on-chip: A 3D cell culture platform for differentiation, stimulation, and proteomic analysis of human adipocytes. *Lab Chip*, **22**(17), 3172–3186 (2022)."[322]

extracellular matrix (ECM) environment[283] but generally lack chemically defined conditions[282]. Furthermore, hydrogel microenvironments complicate downstream analysis because of the high background signals generated by the scaffolds.[296] The presence of confounding proteins in scaffolding hydrogels together with low levels of analyte are the main reasons why mass spectrometry analysis of organ-on-chip platforms is underrepresented. However, increasing the sensitivity of mass spectrometry brings proteome, secretome, and metabolome analysis of organ-on-chip models within reach, as recently demonstrated for a liver-on-a-chip.[168] The demand for high sample numbers comes with the trade-off of requiring higher multiplexing degrees.

Microfluidic large-scale integration (mLSI) technology is considered an enabling platform for cell culture processes with high levels of automation and multiplexing capabilities. To date, mLSI platforms have mainly been integrated into 2D cell culture formats including adipocyte cultures.[23] Only recently mLSI technologies for automated 3D cell culture and analysis became available.[24,32,97] While a dimensional incompatibility of traditional mLSI fabrication techniques and 3D cell cultures has hampered progression of the technology, 3D-printing-based fabrication approach overcome this problem.[97] 3D printing fabrication enable unit operations for handling 3D cell cultures on-chip as for example sample retrieval without destruction. However, the throughput of these platforms is far below that required for high-throughput proteomic studies of adipose tissue *in vitro*.

Here, we address this shortcoming by exploiting a previously developed fabrication protocol[97] for the development of a higher-throughput mLSI platform for 3D cell culture formats. By integrating traditional and upscaled pneumatic membrane valves (PMVs), the core functional unit of the mLSI technique, an mLSI platform comprising 32 fluidically individually addressable cell culture chambers enabled the formation, long-term culture, and non-destructive retrieval of 96 3D cell cultures in a highly controllable manner. Furthermore, scaffold-free 3D on-chip adipogenesis of hASCs was conducted in an automated and reproducible manner. The generated adipocyte 3D cell cultures resembled phenotypically mature adipocytes, which was confirmed by lipid droplet staining of cryo-sectioned aggregates and detection of upregulated key adipocyte markers by proteomic analysis. To investigate whether differentiated adipocytes in a 3D cell culture format could serve as an *in vitro* adipose tissue-on-chip model, we subjected them to glucose restriction post-differentiation by decreasing the concentration of glucose in the maintenance medium, and then analyzed the induced changes at the proteome level. We also retrieved minimal cell sample volumes from the mLSI chip and acquired unbiased proteomes using mass spectrometry. We successfully investigated different glucose feeding regimes in parallel on a single platform and characterized the phenotype of the differentiated adipose aggregates in detail.

5.1 Materials and methods

5.1.1 Master mold and PDMS chip fabrication

The master mold for the mLSI flow layer was designed in SolidWorks (version 2018-2019; Dassault Systèmes, France) and 3D-printed using a DLP stereolithography printer (Pico2HD, Asiga, Australia). The mold was printed as a negative using PlasGRAY resin (Asiga). The thickness of the printed layer was 10 µm. All other printing parameters (e.g., light intensity and exposure time) were kept at their default values according to the manufacturer's instructions. After printing, the flow mold was cleaned with isopropyl alcohol, flash-cured (Otoflash G171; NK-Optik, Germany) with 2000 flashes on each side, and then coated with a 2% solution of CYTOP^{TM} (CTL-809M; AGC Chemicals, Japan), in accordance with the previously developed protocol[97], to prevent adhesion of PDMS. A negative control layer was fabricated according to the standard SU-8 (SU-8 3050; Microresist Technology, Germany) photolithography protocols[33]. Similar to the flow mold, the control mold was permanently coated with CYTOP^{TM} to facilitate PDMS release. A thin film of CYTOP^{TM} was spin-coated on the wafer (20 s at 500 rpm, then 30 s at 3000 rpm) and incubated for 1 h at 160 °C to evaporate the CYTOP^{TM} solvent. The first PDMS cast from the CYTOP-coated molds was discarded to ensure proper bonding of the succeeding PDMS casts.

The mLSI platform was fabricated by multilayer soft lithography[33] using a 3D-printed flow and a SU-8 silicon control mold. In short, the upper flow layer was manufactured by casting a thick layer (approx. 5 mm) of PDMS (ratio 5:1 of base material to curing agent; Sylgard® 184, Dow Corning, MI, USA) onto the flow mold, while for the lower control layer, PDMS (20:1 ratio) was spin-coated onto the wafer at 500 rpm for 15 s (acceleration 518 ms), followed by spinning at 1250 rpm for 30 s (acceleration 2220 ms). Both layers were partially cured for 20–25 min at 80 °C and the flow layer was released from the mold and aligned with the control layer. The assembly was again incubated for 45 min at 80 °C to enable off-ratio PDMS bonding. Next, the inlet and outlet ports for both layers were punched using a 20 gauge and 14 gauge needle, respectively. Finally, the mLSI device was sealed with a cover glass after oxygen plasma activation (20 W at 0.9 mbar for 25 s) and incubated for further 60 min at 80 °C.

5.1.2 Flow characterization of the cell culture chamber

To analyze fluid flow within the cell culture chamber, a particle-tracking experiment was conducted. To achieve this, 2.55-µm polystyrene beads (PS-F-B237-1; microParticles GmbH, Germany) were flushed through the cell culture chambers of the mLSI chip. The actuation pressure of the trapping PMVs was increased incrementally in steps of 0.7 bar (10 psi), and the particle flow was recorded on an AxioObserver (Zeiss, Germany) with a frame rate of 300 fps. Prior to each measurement, the trapping PMVs were opened and closed at least once to avoid error due to the residual pressure in the system. During the measurement, constant fluid forward pressures of 35, 50, 100, and 125 mbar were applied. Recorded data from five culture chambers were subsequently analyzed in ImageJ (v1.53f51) using the TrackMate[261] plugin and exported to a custom-written MATLAB (version R2019a; MathWorks, MA, USA) script for visualization and flow rate calculations.

5.1.3 Chip preparation for cell experiments

The control lines of the mLSI chip were directly connected to the solenoid valves (LVM155RHY-5A-Q; SMC, Japan) with Tygon tubing (ND 100-80; Proliquid, Germany) and operated using a custom-written MATLAB script. The control lines for the trapping PMVs were operated by a separate manual pressure regulator (LRP-1/4-4; Festo, Germany) to regulate their actuation pressure independent of the other valves on-chip. All other valves on the mLSI platform were operated at a control pressure of 2.2 bar. Reagents were filled in gas-tight, light-proof bottles and connected to the flow inlet ports through the Tygon tubing. The forward fluid pressure used to pressurize the bottles was controlled by a flow control unit (Flow EZ^{TM}; Fluigent, France). The outlet ports were connected to the Tygon tubing and maintained at atmospheric pressure. The mLSI chip was placed in a microscope stage-top incubator (STX; Tokai Hit®, Japan) to ensure a constant humidified atmosphere of 37 °C and 5% CO_2. Prior to seeding the cells on the chip, the fluidic network was coated with 10% Pluronic® F127 (Sigma-Aldrich, MO, USA) in phosphate-buffered saline (PBS; Sigma-Aldrich) for a minimum of 20 h to reduce cell attachment to the PDMS. The chip was rinsed with PBS to remove the Pluronic® and then pre-incubated with the cell culture medium for 30–60 min to equilibrate.

5.1.4 3D cell culture and adipogenic differentiation on-chip

Human adipose tissue-derived stem cells (hASCs; ASC-F-ZB) were purchased from ZenBio (NC, USA) and maintained in routine 2D cell culture using subcutaneous preadipocyte growth medium (PM-1; ZenBio) according to the supplier's protocol. hASCs at passages 6–8 were used for the experiments. To seed cells on-chip, hASCs were detached from the culture flask using 0.25% trypsin-EDTA (Sigma-Aldrich), centrifuged at 280 × *g* for 5 min, and resuspended at a concentration of approximately 3.5×10^5 in 30 µL of PM-1. Using Tygon tubing, the single-cell suspension was then transferred on-chip, where we filled four chambers simultaneously until all on-chip chambers were visually seeded with an equal number of cells. The actuation pressure of the trapping PMVs was then slowly increased at a rate of approximately 1 psi/s, up to a closing pressure of 32 psi. Non-trapped cells were then safely rinsed from the fluidic network at a fluid forward pressure of 25 mbar. The trapped cells were undisturbed for 4 h before the first feeding cycle. The trapping valve and fluid forward pressures varied between 25–28 and 35–50 mbar, respectively. Pressures were kept constant throughout the experiment, and cells were automatically fed every 4 h for 15 s, unless stated otherwise, using a custom-written MATLAB script.

Differentiation of hASCs was initiated on day 1, 24 h after seeding when aggregates had formed, by switching from the standard growth medium to the commercially available differentiation induction medium DM-2 (ZenBio). On day 8, the medium was changed to adipocyte maintenance medium (AM-1; ZenBio) and the cultures were maintained until day 15 to obtain fully matured adipocytes. Aggregates fed only PM-1 were used as the non-differentiated controls (Ctrl). Media bottles were maintained at room temperature (RT) and replenished every 3–4 days.

5.1.5 Glucose treatment of differentiated adipocyte aggregates on-chip

For the glucose treatment experiments, we prepared a customized maintenance medium in which the basal media constituted a 1:1 mixture of DMEM without glucose (Thermo Fisher Scientific, MA, USA) and Ham’s F-12 Nutrient Mix (Thermo Fisher Scientific) supplemented with 10% fetal bovine serum (FBS; Corning, NY, USA) and 1% penicillin-streptomycin. Depending on the required composition, glucose (Thermo Fisher Scientific) and human insulin (Sigma-Aldrich) were added to the basal medium to complement the customized maturation media. The low-glucose (LoGlu) medium contained a basal glucose concentration of 5 mM and was supplemented with insulin to a final concentration of 20 nM. High-glucose (HiGlu) medium was supplemented with both glucose and insulin to a final concentration of 25 mM and 1.7 µM, respectively.

Before glucose treatment, 3D cell cultures of hASCs underwent adipogenic differentiation for 14 days as described previously. Matured adipocyte aggregates on-chip were then either fed permanently or intermittently with customized maintenance media for a further 7 days, forming three sample groups: 1) feeding with HiGlu medium only (serving as the control), 2) feeding with LoGlu medium only, and 3) alternating feeding with HiGlu and LoGlu media. All of the sample groups were perfused every 6 h for 15 s at a fluid pressure of 50 mbar. The trapping valves were actuated at a controlled pressure of 28 psi.

5.1.6 Aggregate retrieval off-chip

To retrieve 3D aggregates from the mLSI chip, a pipette tip was connected to the outlet port, and the medium was directed to flow from the inlet port through the multiplexer into the culture chamber and out via the outlet. Before retrieval, the aggregates were extensively washed on-chip with PBS. To release trapped aggregates, the trapping PMVs were slowly deactivated at a rate of approximately 10 psi/min to minimize the movement of aggregates within the other culture chambers. Once the aggregates were flushed out of the chamber into the pipette tip, the activation of the trapping PMVs was restored to their previous control pressure. Retrieved aggregates were then transferred from the pipette tip into V-bottom 96-well plates (Santa Cruz Biotechnology, TX, USA) for cryosectioning, or into 1.5-mL Eppendorf tubes for mass spectrometry. Occasionally, a few aggregates were attached to the PDMS; these were detached using trypsin and retrieved as single cells.

Depending on the downstream analysis requirements, aggregates from at least four chambers on-chip (technical replicates) were retrieved at the following time points: for cryosections on days 1, 8, and 15, and for mass spectrometry on days 1, 15, and 22 (14 days differentiation + 7 days treatment).

5.1.7 Cryosections and immunofluorescent analysis

The aggregates were washed with PBS twice before fixing for 1 h at RT using 4% (w/v) paraformaldehyde (PFA). Next, the aggregates were dehydrated at RT using a sucrose gradient of 10% (w/v) and 30% (w/v) for 2 h, followed by overnight incubation in a 1:1 mixture of 30% sucrose and tissue freezing medium (Leica, Germany) at 4 °C. The next day, the aggregates were transferred to cryomolds and embedded in tissue freezing medium on dry ice. The frozen aggregates were stored at −80 °C until cryosectioning, for which they were cut into 10-µm slices on a cryostat at −30 °C.

For immunofluorescent staining of aggregate cryosections, frozen slices were pre-warmed to RT and washed in a Coplin jar containing PBS. After washing, they were permeabilized with 0.1% Triton^{TM} X-100 (Sigma-Aldrich) in PBS for 30 min at RT, followed by incubation in blocking buffer (PBS, 0.2% Tween 20 (Carl Roth, Germany) and 10% donkey serum (Abcam, UK)) for 1 h at RT. The slides were then incubated for 2 h in the dark at RT with DAPI (1:500; Sigma-Aldrich) and BODIPY 493/503 (10 µg/mL; Thermo Fisher Scientific) diluted in blocking buffer. Subsequently, the slides were washed extensively with 0.2% Tween 20 in PBS and mounted using Vectashield (Vector Laboratories, CA, USA).

5.1.8 Microscopy and image analysis

Bright-field images of the 3D aggregates on-chip were acquired with 2.5× and 10× objectives (Plan-Apochromat) on an Axiovert inverted microscope (Zeiss). A confocal microscope (LSM-880, Zeiss) and a 20× objective were used to record immunofluorescent and bright-field images of the stained cryosections. Image analysis and statistical evaluation were performed using custom-written macros and scripts in ImageJ and MATLAB software, respectively.

5.1.9 Sample preparation for mass spectrometry

After the retrieval of aggregates, as much PBS as possible was aspirated from the Eppendorf tubes before freezing the samples at −80 °C until further processing. The whole aggregate pellets were processed by tryptic digestion using the PreOmics iST Kit (Preomics GmbH, Martinsried, Germany) according to the manufacturer’s specifications. After drying, the resulting peptides were resuspended in 2% acetonitrile (ACN) and 0.5% trifluoroacetic acid.

5.1.10 Mass spectrometric measurements

Liquid chromatography-tandem mass spectrometry (LC-MS/MS) analysis was performed in data-dependent acquisition (DDA) mode. MS data were acquired on a Q-Exactive HF-X mass spectrometer (Thermo Scientific), coupled online to a nano-RSLC (Ultimate 3000 RSLC; Dionex). Tryptic peptides were automatically loaded onto a C18 trap column (Acclaim

PepMap100 C18, 300 µm inner diameter (ID) × 5 mm, 5 µm, 100 Å, LC Packings) at a flow rate of 30 µL/min. For chromatography, a C18 reversed-phase analytical column (nanoEase MZ HSS T3 column, 100 Å, 1.8 µm, 75 µm × 250 mm, Waters) at 250 nL/min flow rate in a 95 min non-linear acetonitrile gradient from 3–40% in 0.1% formic acid was used. The high-resolution (60 000 full width at half-maximum) MS spectrum was acquired with a mass range from 300 to 1500 *m*/*z* with an automatic gain control target set to 3×10^6 and a maximum injection time of 30 ms. From the MS prescan, the 15 most abundant peptide ions were selected for fragmentation (MS/MS) if at least doubly charged, with a dynamic exclusion of 30 s. MS/MS spectra were recorded at 15 000 resolution with an automatic gain control target set to 5×10^2 and a maximum injection time of 50 ms. The normalized collision energy was 28, and the spectra were recorded in profile mode.

5.1.11 Data processing – protein identification

Proteome Discoverer 2.5 software (Thermo Fisher Scientific; version 2.5.0.400) was used for peptide and protein identification via a database search (Sequest HT search engine) against the SwissProt human database (Release 2020_02, 20432 sequences), considering full tryptic specificity, allowing for one missed tryptic cleavage site, precursor mass tolerance of 10 ppm, and fragment mass tolerance of 0.02 Da. Carbamidomethylation of Cys was used as a static modification. Dynamic modifications included deamidation of Asn and Gln, oxidation of Met, and a combination of Met loss with acetylation on the protein N-terminus. Percolator algorithm was used to validate peptide spectrum matches and peptides, accepting only the top-scoring hit for each spectrum and satisfying the cutoff values for FDR < 1% and posterior error probability < 0.05. The Sequest HT Xcorr filter was set to 1, removing identifications below this threshold. The final list of proteins complied strictly with the parsimony principle.

5.1.12 Data processing – label-free quantification

Protein quantification was based on the abundance values of unique peptides. Abundance values were normalized to the total peptide amount to account for sample loading errors. Protein abundances were calculated by summing the abundance values for admissible peptides. Proteins identified in only one replicate of a sample group, as well as contaminants from Bos taurus and keratin proteins, were excluded from the analysis. Differential protein expression analysis was performed using the DEP Bioconductor package[297] in R (RStudio version 1.4.1717; MA, USA). Subsequent functional enrichment analysis and visualization were performed using the STRING database [298] and customized Python (version 3.9) scripts.

5.1.13 Statistical analysis

Experiments were conducted at least twice (*N* = 2) with a minimum of four independent on-chip chambers as technical replicates unless otherwise stated. Extracted quantitative data (*e.g.*, flow rate, equivalent diameter, and retrieval rate) are represented as the mean ± SD unless otherwise stated. Statistical significance was set at $p < 0.05$. Normal distribution was tested using the Shapiro–Wilk test[243] in MATLAB R2019a.

5.2 Results and discussion

5.2.1 3D-printing enables the integration of upscaled and standard sized PMVs on an mLSI chip

Non-destructive and automated handling of 3D cell cultures on mLSI platforms is required to enable the use of organ-on-chip technology for higher-throughput applications. In general, PMVs, the central functional element for controlling fluid flow on mLSI chips, can close microchannels with a semi-round channel geometry and dimensions of 2–50 µm in height.[33] We have recently shown that PMVs can be scaled to close fluidic channels, with heights of up to a few hundreds of micrometers, by using a 3D-printing approach for the production of soft-lithography molds.[97] This enabled the successful integration of 3D cell cultures on mLSI chips. The work presented here builds on this advance and exploits the high level of design flexibility of the 3D printing process to fabricate an mLSI chip for cultivating 96 3D cell cultures within 32 fluidically individually addressable unit cells (**Figure 5.1A**). The overall footprint of the mLSI chip was 29 mm x 52 mm. The parallelization degree on the mLSI chips produced remains limited because of the relatively small building platform of generally available high-resolution 3D printers. To increase the parallelization degree by an order of magnitude, as achieved for 2D cell cultures[25,177,186,299] on mLSI chips, a new 3D printer generation is required. Despite the current limitations, the design flexibility of 3D printers to integrate microsystem design features to handle 3D cell culture within channel networks with heights of several hundred microns was exploited to design a cell culture chamber (**Figure 5.1B**) that was based on the previously presented unit cell design and facilitated 3D cell culture formation by self-aggregation from single cells, automated medium exchange for long-term culture, and retrieval of the 3D cell culture sample. While the central region of the cell culture chamber exhibited a height and width of 200 µm and 300 µm respectively (**Figure 5.1C**), the two bypassing channels bifurcating at the entry of the cell culture chamber had a cross-section of 30 µm x 100 µm. Bypassing channels are required for rinsing the fluidic network of non-trapped cells. Each cell culture chamber can be compartmentalized into three consecutive regions by actuation of PMVs designed in a push-up configuration and herein termed trapping PMVs (**Figure 5.1D**). These were operated in one of the following three pressure states (**Figure 5.1E**): i) a fully closed state to trap a single cell suspension, ii) a sieve state for perfusion of 3D cell cultures after formation, and iii) an open state for retrieval of the cell material. The sieve state was achieved by making use of the 3D-printing–induced staircase effect on the fluidic channel profile.[97] Within the pressure regime, states between 0.5 bar and 2.0 bar caused the deflected PDMS membrane to close the half-rounded channel imperfectly such that small gaps on the staircase profile remained open. Larger objects, including 3D cell cultures or single cells, were trapped and could not pass through the trapping valve in the sieve state (**Figure 5.1E**). With the assisted self-aggregation mechanism in the cell culture chamber and retrieval of 3D cell cultures in a non-destructive manner, we added two new features to the mLSI design

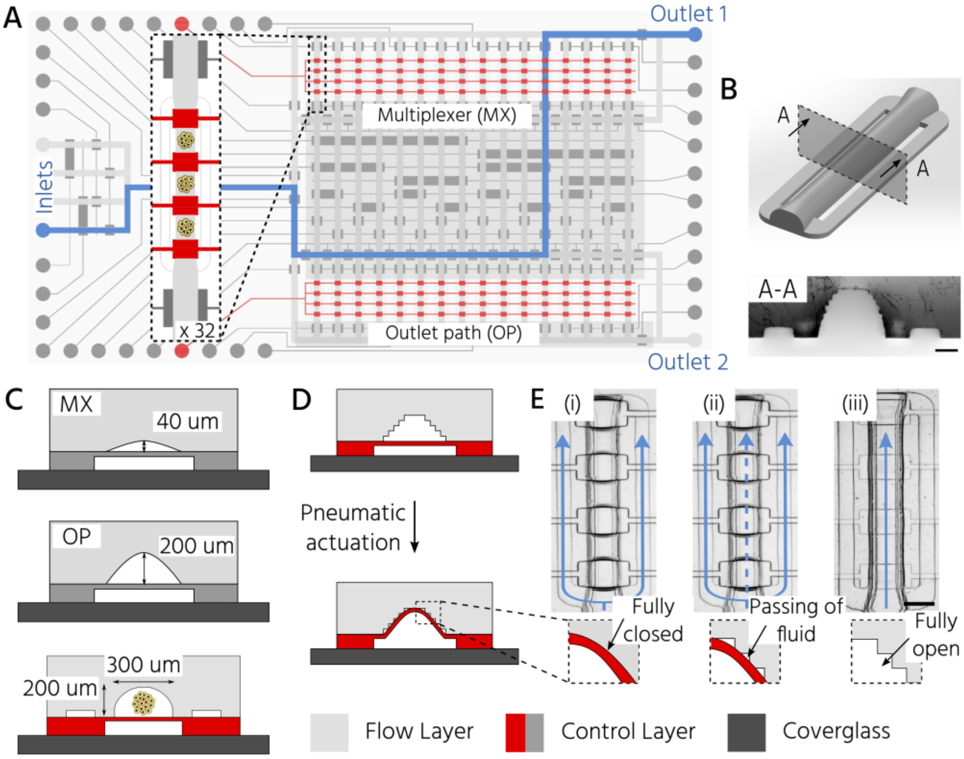

Figure 5.1 Microfluidic large-scale integration platform for the automated formation of 3D cell cultures, long-term parallel culturing process, and individual retrieval of cell cultures. (**A**) Schematic layout of the two-layer mLSI chip design. Flow channels up and down stream of the cell culture chamber are shown (multiplexer (MX) and outlet path (OP)). Inset shows in detail one unit cell of the 32 culture chambers. (**B**) 3D model (top) and cross-section of the PDMS layer (bottom) of the cell culture chamber. Scale bar: 100 µm. (**C**) Schematic cross-section of different chip areas with indicated flow channel heights. (**D**) Operating principle of the trapping PMVs (highlighted in red) by pneumatic actuation. (**E**) Operating states of the trapping PMVs. The main paths of fluid flow are indicated in blue. (i) Closed state: cells are introduced as single-cell suspensions and safely confined at respective sites upon fully closing the trapping PMVs. (ii) Sieve state: perfusion of self-aggregated 3D cell cultures. Due to the staircase effect on the 3D-printed flow master mold, trapping PMVs allow for the passing of fluid while safely keeping the 3D aggregates in place. (iii) Open state: 3D aggregates can be retrieved by deactivation of the trapping PMVs. Scale bar: 250 µm.

toolbox.[24,97] Flow channels upstream (multiplexer area) and downstream (outlet path) of the cell culture chamber had heights of 40 and 200 µm, respectively (**Figure 5.1C**). The lower height of the upstream channels was chosen to minimize the dead volume of the channel network and to ensure the fully closed state of the PMVs at an actuation pressure of 2 bar, despite the staircase effect. This concomitantly reduced the number of cells required to fill the cell culture chambers during the cell-seeding process (see below). Since cells were seeded as a single-cell solution, they could be routed through 40-µm high channels without affecting cell integrity. Non-destructive retrieval of 3D cell cultures from the cell culture chambers required the downstream channels towards the outlet port to be at least equally high as the 3D cell culture chamber. To address the cell culture chambers individually, a standard $2\log_2 N$-multiplexer was included. The multiplexer divided the cell culture chamber area into two blocks of 16 chambers each. All PMVs were controlled with an actuation pressure of 2.2 bar, with the exception of the trapping PMVs, since they require adjustable pressure application to achieve the sieve state.

In a first step, the fluid flow within the cell culture chamber depending on the actuation state of the trapping PMVs has been characterized by particle tracking to prove the functionality of the unit cell for cell trapping. In the open state of the trapping PMVs (**Figure 5.2A**, top), the flow velocity in the main channel was 0.21 µL/s at a constant fluid forward pressure of 100 mbar (**Figure 5.2A**, **B**). The flow velocity in the side channels was 7.0 nL/s, demonstrating that approximately 94% of the volumetric flow passed through the main channel (**Figure 5.2A**, **C**). This was expected because of the channel size difference, where the theoretical fluidic resistance based on the Hagen–Poiseuille approximation was approximately three orders of magnitude larger in the side channels than in the main channel. Upon increasing the actuation pressure of the trapping valves, the flow velocity decreased in the main channel and increased in the side channels. At an actuation pressure of 2 bar, the mean flow velocity in the main channel was 0.014 µL/s (for a fluid forward pressure of 100 mbar), which is 15-fold lower than

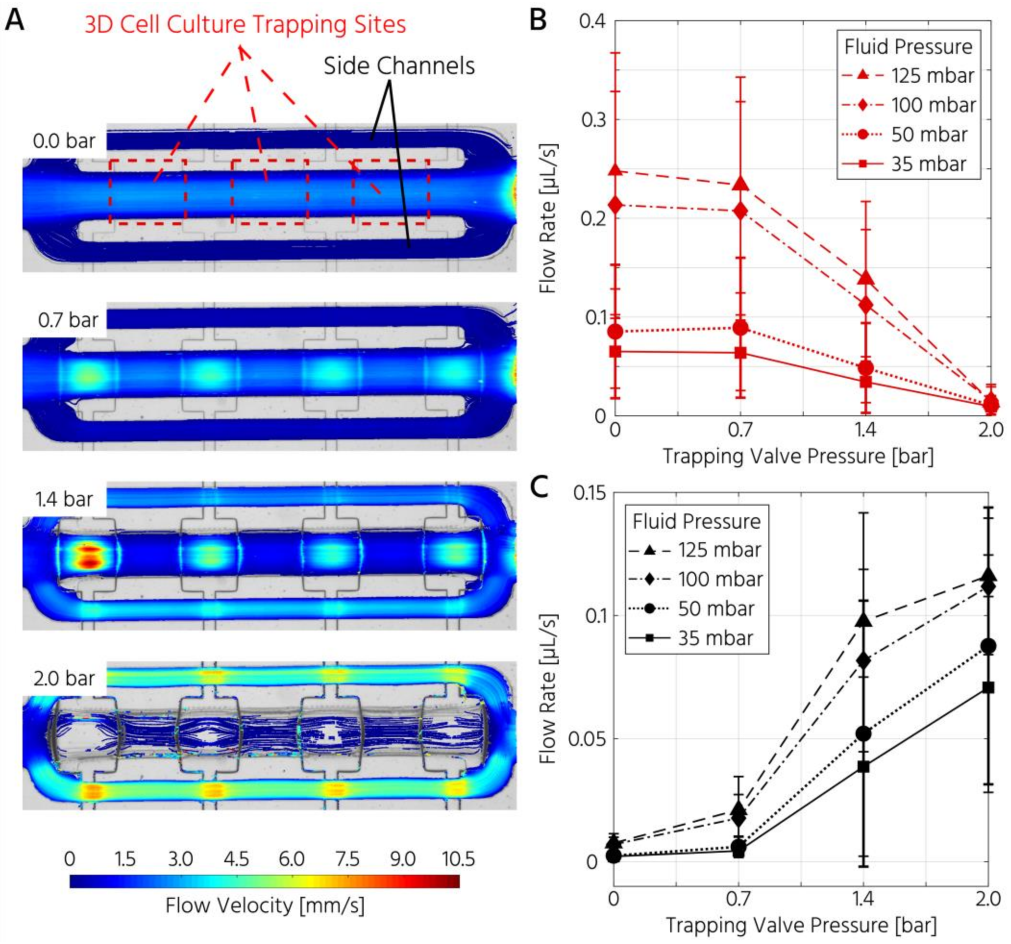

Figure 5.2 The actuation pressure of the trapping valve controls the flow-path and -rate in the cell culture chamber of the mLSI chip. (**A**) Actuation of the trapping PMV leads to a change of flow velocity and path from the main to the side channels at a constant fluid forward pressure of 100 mbar. (**B**, **C**) Plots show the mean (± SD) flow velocities inside the trapping region (B) and the side channels (C) relative to the fluid forward and actuation pressure of the trapping PMVs. *n* = 5 chambers on one chip.

that of the open trapping valve state and is defined as the closed state (**Figure 5.2B**). Conversely, the mean flow rate in the side channels increased from 7.0 nL/s to 0.11 µL/s at a PMV actuation pressure from 0 to 2 bar, respectively. The same trend was observed upon decreasing the forward fluid pressure (**Figure 5.2B**, **C**). In summary, it was demonstrated that the flow rate inside the trapping site could be adjusted by both the fluid forward pressure and the control pressure of the trapping PMVs.

5.2.2 Formation, long-term culture, and scaffold-free 3D differentiation of hASCs into adipocytes on the mLSI platform

To test whether the developed platform allows for the robust and reproducible formation, maintenance, and retrieval of 3D cell cultures, the homogeneity of the self-aggregation process of hASCs was first investigated. For this, a single-cell suspension with a cell concentration of 3.5×10^5 in 30 µL was seeded into the cell culture chambers, where the trapping valves were set to their open state. Subsequently, the cells were trapped by setting the trapping PMV to the closed state, and the remaining cells in the fluidic network were rinsed through the side channels towards the outlet (**Figure 5.3A**). Self-aggregation of the hASC was observed within the first 4 h. At this time point, the trapping valves were set to the sieve state, and feeding was initiated by exchanging the media solution in the cell culture chamber for 15 s at a flow rate of 1.5 µL/min every 4 h. In the next 24 h, further compaction of the cell clusters to round hASC 3D cell cultures occurred, with only a few single cells remaining in the trapping areas. To quantitatively evaluate 3D cell culture formation and growth, the equivalent diameter, which is the diameter of a circle with an area equivalent to that of the 3D cell culture, was measured. On average, the 96 hASC 3D cell cultures formed on the mLSI chip exhibited an equivalent diameter of 143 ± 5 µm 24 h after seeding (**Figure 5.3B**). The chip-to-chip variability of the 3D cell culture formation process across six independent chips was low (**Figure 5.3C**). Their mean equivalent diameters varied by 14% compared with the overall mean, thus yielding high reproducibility. Notably, this size deviation was explained by minor differences in cell seeding density. The 3D cell cultures were stable for 15 days on-chip, and their average size varied only minimally (**Figure 5.3D**). During the cultivation period, the hASC 3D cell cultures did not show any signs of diminished cellular viability, such as disaggregation or necrosis. Nevertheless, aggregates were, on average 7% smaller than their initial size on day 1, suggesting that compaction occurred, as observed previously.[282,300] Next, the retrieval efficiency of 3D cell cultures with preserved spatial integrity for further off-chip analyses was determined. For this purpose, the trapping valves were set to the open state and fluidically-addressed chamber by chamber. Overall, 88.6% of 3D cell cultures were recovered through the outlet port (**Figure 5.3E**). During the retrieval process, the micro-macro connection at the outlet port was the main source of cell loss (**Figure 5.3E**). Other, not mLSI-based, microfluidic designs which offer the reversible trapping of 3D cell cultures, such as the U-shaped pneumatic

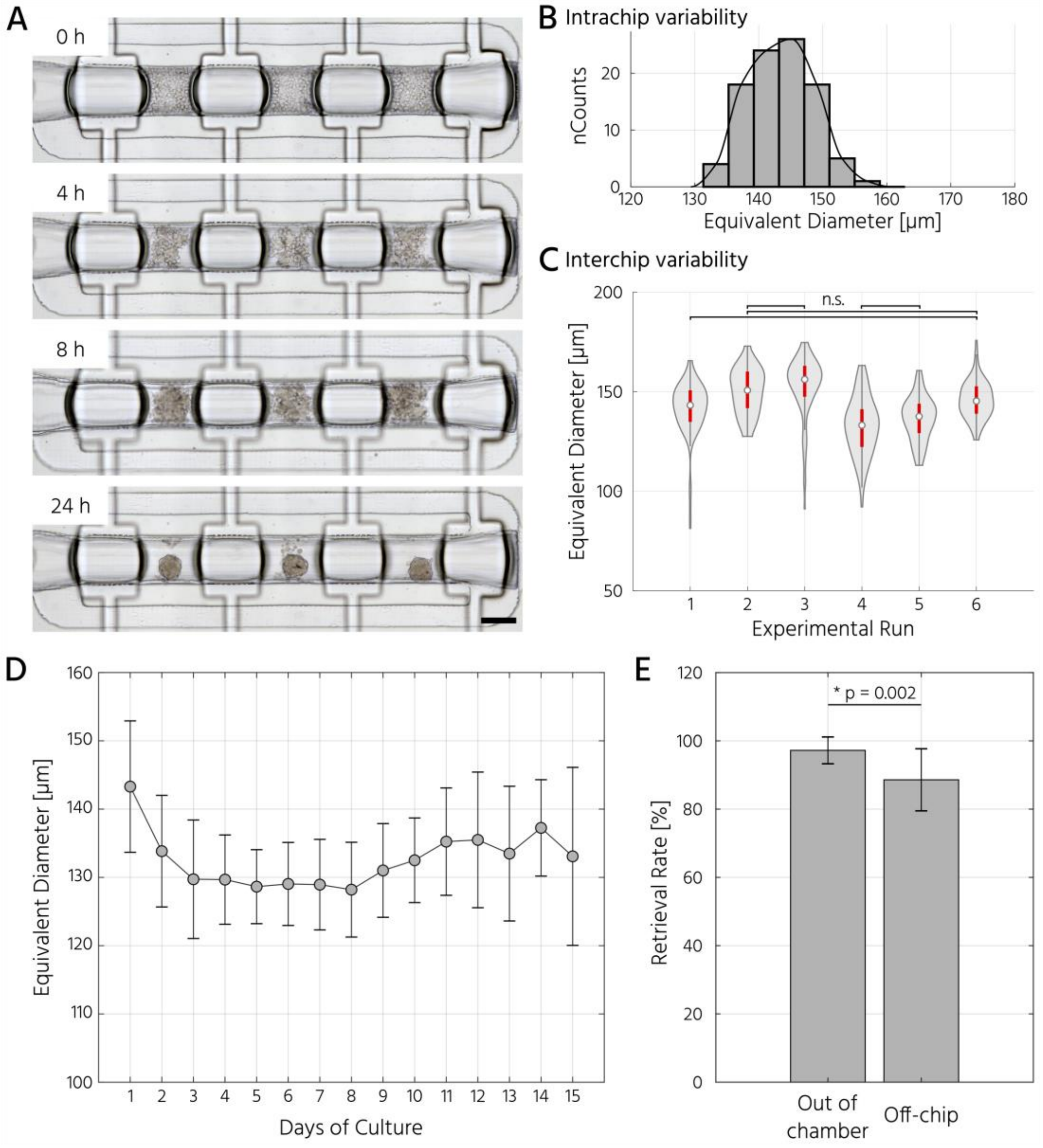

Figure 5.3 Parallel formation and cultivation of human adipose tissue-derived adult stem cells in 3D on-chip. (**A**) Timeline of hASC self-aggregation in the cell culture chamber. Scale bar: 250 µm. (**B**) Intrachip variability of the equivalent diameter of the 3D cell cultures. *n* = 6 biological repeats. (**C**) Interchip variability of the equivalent diameter of formed hASC 3D cell cultures. *n* = 96 technical replicates per chip, all comparisons exhibited a $p < 0.05$ (one-way ANOVA) except for n.s. = not significant. (**D**) Equivalent diameter of the hASC 3D cell cultures during on-chip culture. *n* = 4-12 technical replicates. (**E**) Rates of successful retrieval of the hASC 3D cell cultures from the cell culture chambers. *n* = 3 biological replicates, $*p < 0.05$ (one-way ANOVA).

structures proposed by Liu *et al.*[83], showed similar recovery rates.

In the next step, the developed mLSI platform was sought to be applied to differentiate hASCs into adipocytes in a 3D culture format. hASCs provide a valuable source for the mimicking of adipose tissue *in vitro* as they have been shown to accurately recapitulate adipogenesis[282] and to acquire browning capabilities[301–303]. Recently, the group of Lauschke[282] demonstrated that 3D differentiated adipocyte cultures resemble the molecular and cellular phenotypes of freshly isolated mature adipocytes more closely than conventional 2D cultures.

To mimic the adipocyte organotypic microenvironment even more closely and investigate the adipose tissue's endocrine functionality in a more detailed and dynamic manner, microfluidic chips have been proposed.[292] Several groups have emulated human adipose tissue on a microfluidic chip to investigate adipogenesis[52,100], insulin resistance[109], inflammation in general[105], and the crosstalk between adipocytes and macrophages in specific[136]. However, most 3D adipogenesis techniques in the literature rely on scaffold-based cultures in matrigel[289] or other hydrogels[52,281], despite a poor chemical definition of these conditions.[282,304] Since matrix embedding might complicate sample retrieval and interfere with analytical techniques such as mass spectrometry, a scaffold-free approach was employed here. For this, 96 hASC 3D cell cultures were formed under the above-described conditions within 24 h on-chip. On the first day after seeding, the cell cultures were perfused with adipocyte induction medium, followed by maturation medium each for 7 days (**Figure 5.4A**). During the differentiation phase, progressive darkening of the 3D cell cultures was observed (**Figure 5.4B**), indicating the accumulation of lipid droplets.[305,306] This assumption was confirmed by immunofluorescent staining of lipid droplets in the retrieved 3D cell cultures on days 1, 8, and 15 (**Figure 5.4C**). The mean equivalent diameter of the 3D cell cultures during adipogenesis was constant, with increasing variation at later timepoints across the six independent experiments (**Figure 5.4D**). A slight expansion in size from day eight of the differentiation onwards is likely due to the accumulation of intracellular lipids and less likely due to cell proliferation as suggested by Shen *et al*.[282], who measured stable levels of ATP, an indicator for viable cell count, during the 3D differentiation of hASCs. Nuclei counts of hASCs, preadipocytes, and adipocyte 3D cell cultures confirmed this trend (**Figure 5.4E**), where the average number of nuclei in the center region of a 3D cell culture varied non significantly ($p < 0.05$) between 35 ± 14, 56 ± 18, and 50 ± 11, between day 1, 8, and 15 respectively. While the number of nuclei per 3D cell culture was constant during the differentiation, the number of lipid droplets increased significantly as the cells within the 3D cell culture matured into adipocytes (**Figure 5.4E**). Along with the number of lipid droplets, the lipid droplet volume increased from the preadipocyte to the adipocyte stage (see **Figure 5.4C**). Differentiated adipocytes showed multi- and paucilocular lipid droplet formation and thus, morphologically resemble a premature stage of white adipocytes present *in vivo*, which are typically characterized by unilocular lipid droplets.[282] Maturation of hASC-derived adipocyte aggregates with unilocular lipid droplet formation can be enhanced in the future by extension of the differentiation protocol to 30 days as Shen *et al*.[282] have recently shown that terminal differentiation of adipocytes in 3D takes substantially longer than conventional 2D culture protocols. Overall, the results presented here highlight the generation of an adipose tissue-like organ model in a highly reliable and parallel manner by scaffold-free differentiation of hASC aggregates on the developed mLSI platform.

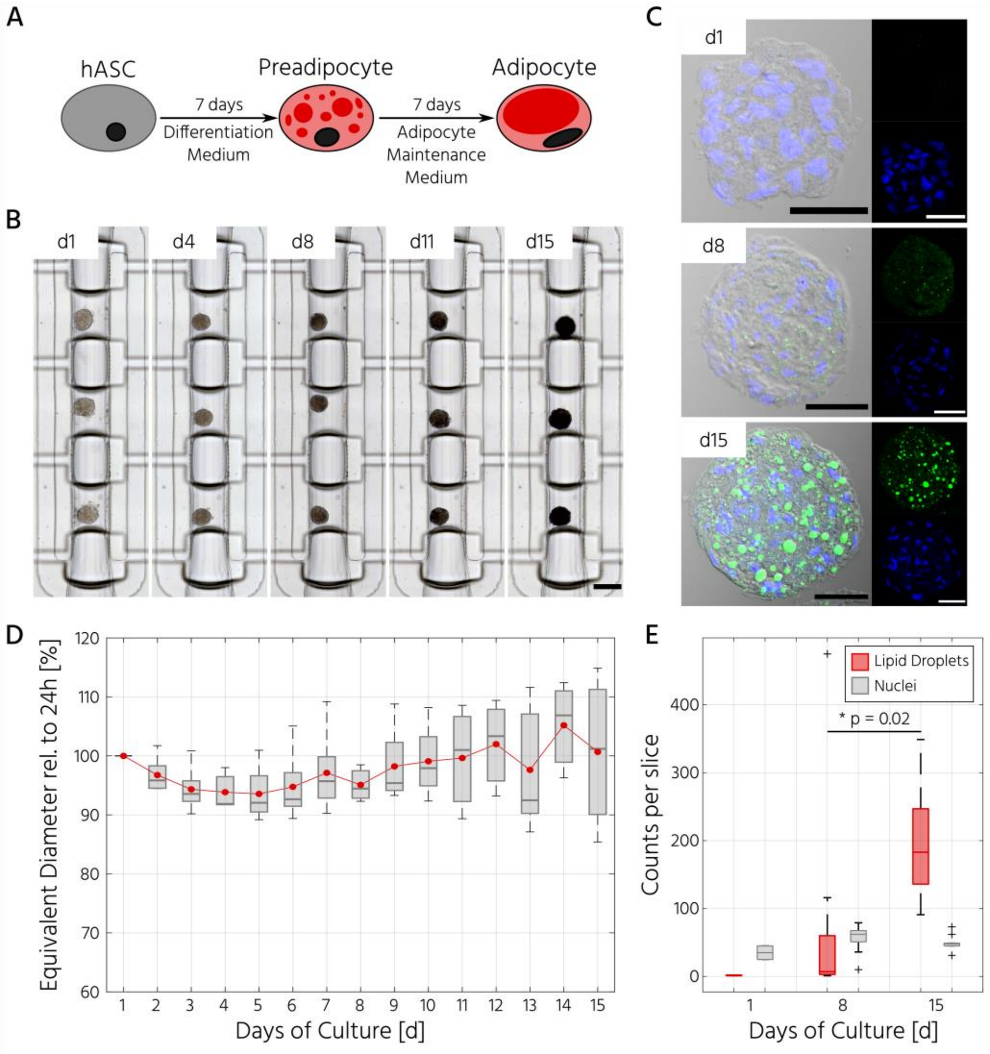

Figure 5.4 Adipocyte 3D cell cultures derived by scaffold-free differentiation of hASCs on-chip exhibit mature adipocyte characteristics. (**A**) Overview of the experimental setup for the differentiation of hASCs towards adipocytes. (**B**) Brightfield images of one representative cell culture chamber along the adipogenic differentiation pulse fed every 4 h. Scale bar: 250 µm. (**C**) Validation of adipogenic maturation by lipid droplet staining (BODIPY, green) of cryosections prepared after retrieval of the 3D cell cultures from the chip. Nuclei were counterstained with DAPI (blue). Scale bars: 50 µm. (**D**) Equivalent diameter of the 3D cell culture during the adipogenic differentiation relative to the aggregate size on day 1. *n* = 4 biological replicates. (**E**) Lipid droplet and nuclei counts over the course of differentiation quantified from the middle section of the 3D cell cultures. *n* = 2 for day 1, *n* = 12 for day 8, *n* = 10 for day 15, **p* < 0.05 (one-way ANOVA).

5.2.3 Proteomic landscape of differentiated adipocyte aggregates changes upon glucose stimulation

Combining microfluidics and quantitative proteomic analysis has recently proved advantageous to identify key drivers for the enhanced maturation of hepatocytes that have been differentiated in a confined microfluidic environment.[168] However, such detailed characterization has not been done for the adipogenic differentiation on-chip. To address this, proteomic analysis of adipocyte aggregates differentiated on-chip was conducted in addition to the morphological analysis to elucidate the underlying molecular mechanisms of the on-chip adipogenesis and provide a more comprehensive characterization of the adipose tissue-on-a-chip model. The scaled number of cell cultures on the mLSI chip platform requires bioanalytical workflows to subject complex tissue mimetics. Fluorescence imaging is a state-of-the-art method for analyzing 3D cell cultures on mLSI chips. The option for sample retrieval enabled the acquisition of complete proteomic information using mass spectrometry analysis. In this experiment, conditioned 3D cell cultures were retrieved and the proteomes of the on-chip–differentiated adipocytes by mass spectrometry were determined. Before comparing the proteomic landscapes of hASCs and differentiated adipocytes, the number of 3D cell cultures required to obtain stable proteomic readouts was quantified (**Figure 5.5A**, Exp1). In contrast to DNA sequencing-based analytics, where signal amplification overcomes sensitivity thresholds for analytes, the proteomic analysis required pooling of cell culture chambers to obtain complex proteomes. For this, cell material from two, four, and eight chambers, which corresponded to 6, 12, and 24 3D cell cultures, were pooled. Following cell lysis and protein digestion, for the three samples, average peptide concentrations of 0.29, 0.32, and 0.33 µg/µL, respectively, were obtained. These results are in line with the reported sensitivity thresholds. Upon pooling the cell material from four or eight chambers the proteome quantification became comparable with approximately 2600 proteins across 2-3 technical replicates (**Figure 5.5B**; $N = 2$ for eight chambers, $N = 3$ for four chambers). The proteome of hASC material pooled from only two chambers showed a lower count, with an average of 1731 proteins. Although the peptide concentration was similar in all three samples, the proteome complexity clearly differed. To minimize the cell samples required for individual 3D cell cultures and to empower the mLSI chip fully, a mass spectrometric sample preparation workflow, including cell lysis and digestion, will need to be integrated onto the chip, similarly to immunofluorescence sample preparation. Based on these results, subsequent mass spectrometry experiments were performed with the material pooled from four cell culture chambers of the mLSI chip.

Next, proteomic differences between the start and endpoints of the hASC differentiation as described above were investigated (**Figure 5.5A**, Exp2). Principal component analysis of the proteomes revealed distinct profiles in both sample groups (**Figure 5.5C**). Interestingly, the two biological replicates of the differentiated sample clustered apart in the second principal component, but this was not observed in the non-differentiated group. This suggests that differentiation results in heterogeneity between the generated adipocytes (PC2 is 7.0% compared to 91.8% in PC1). Analysis of the expression patterns of significantly up- and down-regulated proteins ($p < 0.05$) across both conditions highlighted their overall distinct protein expression profiles (**Figure 5.5D**). The hASCs and adipocytes proteome was successfully delineated, with key proteins of both cell types abundantly expressed in the respective dataset. Among the most significantly upregulated proteins in the differentiated adipocytes in 3D cell culture were well-known adipocyte marker proteins, including fatty acid-binding protein 4 (FABP4), perilipin (PLIN4), adiponectin (ADIPOQ), and fatty acid synthase (FASN) (**Figure**

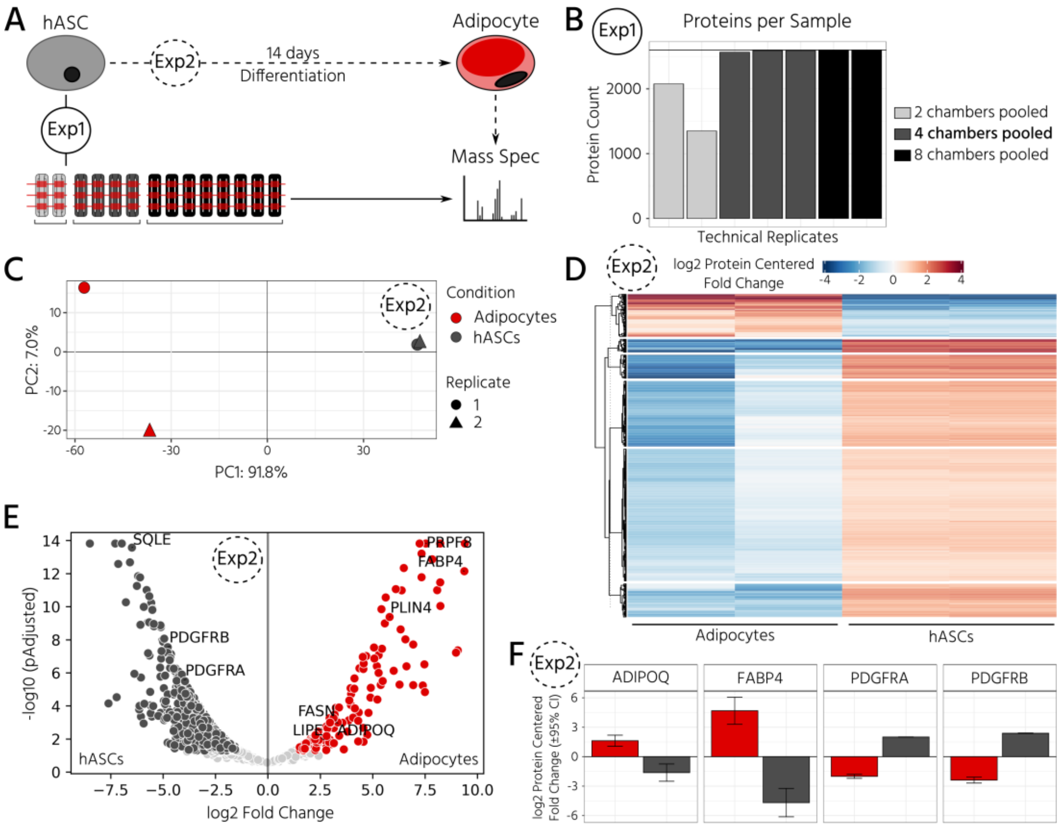

Figure 5.5 Proteomic mass spectrometry analysis of 3D hASC and differentiated adipocyte cell cultures on-chip. (**A**) Overview of the experimental setup. During differentiation 3D cell cultures were pulse fed every 4h. (1) For determining the required quantity of cell sample material for robust preparation of proteomes by mass spectrometry different numbers of 3D cell cultures were pooled as indicated. (2) Proteome analysis of hASC differentiation into adipocytes. (**B**) Number of proteins identified per technical replicate of hASC cell material pooled from either 2, 4, or 8 cell culture chambers. (**C**) Principal components analysis of normalized protein abundances of adipocytes and hASCs. $n = 2$ biological replicates. (**D**) Heatmap representation of k-means clustering of all significant differentially expressed proteins. (**E**) Volcano plot of differentially expressed proteins for hASCs and adipocytes. Proteins with $p < 0.05$ and fold change > 1.5 are highlighted in respective colors: dark gray for the hASCs, red for the adipocytes. (**F**) Mean expression levels of adipocyte and pre-adipocyte protein markers.

5.5E, **F**). Transcription factors such as peroxisome proliferator-activated receptor gamma (PPARγ) and CCAAT/enhancer-binding protein alpha (CEBPα) could not be detected, however, their concertation is generally thousand-fold lower than the other markers.[307] In contrast, pre-adipocyte protein markers, including platelet-derived growth factor receptors alpha and beta (PDGFRα and PDGFRβ), were significantly downregulated in adipocytes and highly expressed in hASCs. Taken together, the proteomic profiles confirmed successful adipocyte differentiation on-chip.

Simulating blood glucose oscillations after periodical food intake *in vitro* requires dynamically controlled cell culture methods. The developed mLSI platform facilitates this kind of study and was exploited to investigate proteomic changes in adipocyte 3D cell cultures in response to different nutritional culture conditions induced by defined long-term feeding protocols. Glucose oscillation with a frequency of 12 h over longer periods has been poorly investigated, and no studies exploring these oscillations at a 6-h frequency have been performed thus far. Therefore, hASCs were first differentiated over a time course of 14 days on the chip, as described above. Subsequently, the adipocyte 3D cell cultures within the cell chambers were fed every 6 h with a maintenance medium containing either (i) a high glucose concentration of 25 mM, (ii) a low glucose concentration of 5 mM, or (iii) alternating between (i) and (ii) (**Figure 5.6A**). For comparison, 25 mM is the glucose concentration contained in the maturation media during the second week of adipocyte differentiation, and thus, the basal medium for the cell type. After being subjected to the glucose regimes for seven days, the conditioned 3D cell cultures were retrieved from the chip and analyzed by mass spectrometry following the same procedure as described previously. Adipocyte proteomes exhibited a total of 1844 proteins, of which 92.6% of the measured proteins were identified in all three sample groups and 6.2% in at least two of the three conditions (**Figure 5.6B**). Under all three conditions, we observed a differentially expressed protein pattern (**Figure 5.6C**).

To investigate the influence of the glucose concentration on the adipocyte proteome, the protein fold changes in the low and alternating conditions, as compared to those in the high glucose condition, were calculated. Adipocytes under the low glucose condition showed the upregulation of proteins associated with overcoming energy restriction and dysregulation of inflammatory signals. The most significantly upregulated proteins under the low glucose conditions are shown in **Figure 5.6E** and included hydrolases such as pancreatic triglyceride lipase (PNLIP), chymotrypsin-C (CTRC), and chymotrypsin-like protein (CTRL). The activity of PNLIP and other lipases have been shown to continuously hydrolyze adipose triglyceride and generate free fatty acids even under adverse environmental conditions such as long-term nutritional deficiency[130] and ongoing inflammation[308]. Proteins known to be involved in dysregulation of inflammatory signals, such as ABCA10[309] and S100A7, known as psoriasin, were also upregulated. Downregulation of FBN1, the precursor protein for the adipokine asprosin, and of complement factor D has also been reported in this and other studies investigating nutritional restrictions[310–312]; our findings thus concur with those previously noted. Upregulated proteins in the alternating feeding regime (**Figure 5.6F**) were the mitochondrial creatine kinase CKMT2, which is highly expressed in tissues with large fluctuating energy demands[313,314], and inositol monophosphatase 1 (IMPA1), which protects the cells from the osmotic stress induced by the highly osmotic glucose-6-phosphatase[315]. CKMT2 is typically expressed at higher levels in beige- and brown-fat mitochondria[313,314] and thus indicates upregulated metabolic turnover. A direct comparison of the adipocyte proteomes under alternating and low-glucose conditions (both plotted versus the high-glucose condition) showed that they shared the majority of differentially regulated proteins (**Figure 5.6D**). For example, the nucleosome-binding protein, HP1BP3, which regulates cell survival and proliferation, was downregulated under both conditions. In general, the proteome acquired for adipocytes in the alternating high/low glucose perfusion regime correlated closer to the high-glucose regime (Pearson correlation of *r* between 0.68 and 0.87) than to the low-glucose regime (*r* between 0.38 and 0.66), showing that the high glucose interval partly compensated the 6 h of low glucose concentration. The closest *in vitro* references to our work investigated the effect of oscillating glucose at high and low glucose concentrations in conjunction with saturated fatty acid.[316] While the study found a sustained inflammatory effect even once the treatment was halted, this effect was attributed to saturated fatty acid treatment rather than the oscillating

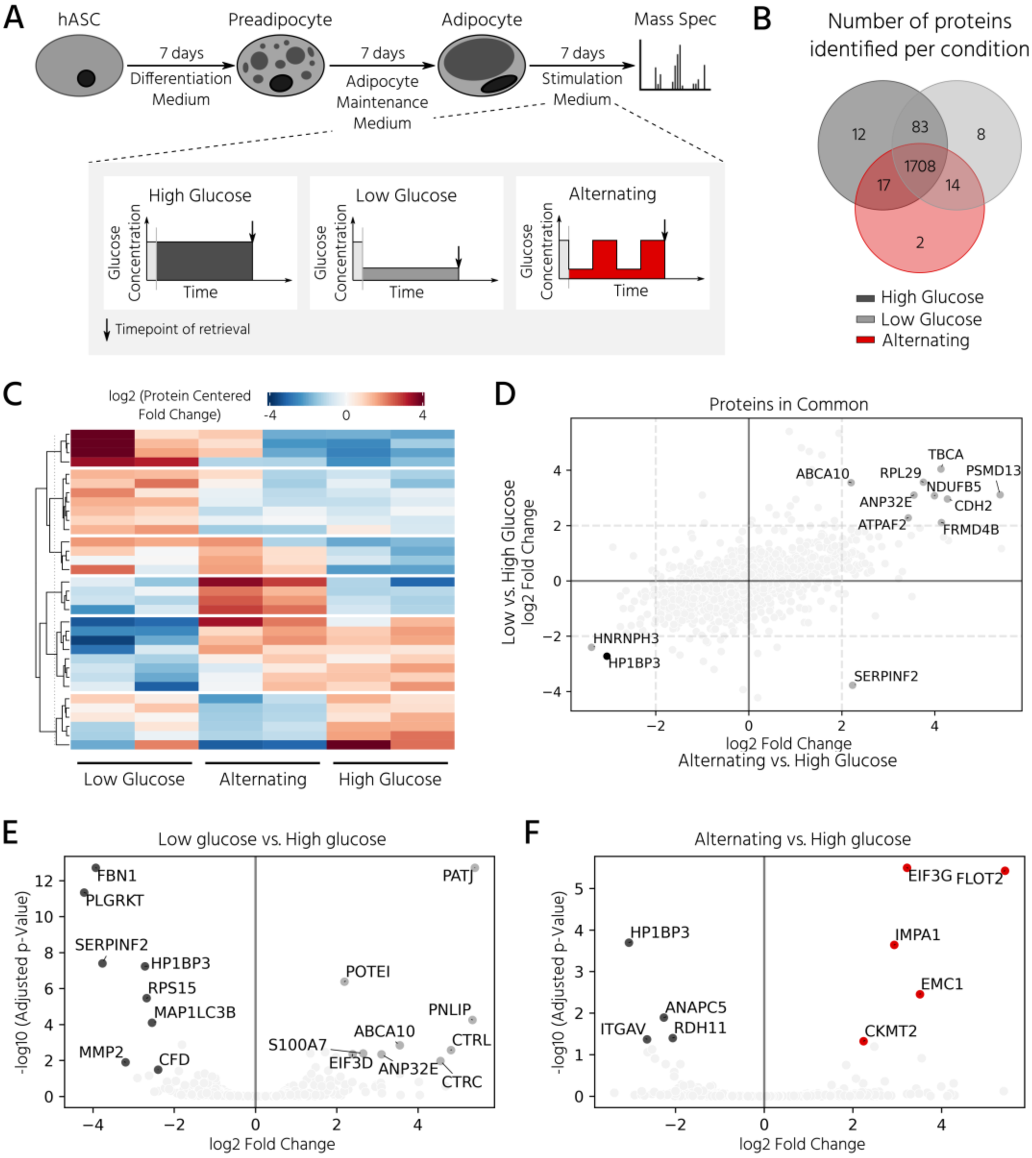

Figure 5.6 Proteomic changes of differentiated adipocytes upon prolonged exposure to varying levels of glucose concentration. (**A**) Experimental setup of the glucose treatment study. After differentiation (14 days), adipocytes were treated for an additional 7 days with either constant or alternating levels of glucose in the maintenance medium (high concentration: 25 mM, low concentration: 5 mM). (**B**) Venn diagram of identified proteins per condition. The majority of identified proteins (92.6%) were shared among all tested conditions. (**C**) Heatmap representation of significant ($p < 0.05$) proteins among all conditions. $n = 2$ biological replicates. (**D**) Comparison of log2 (fold-change) of proteins shared between the low glucose and alternating condition, both with respect to the high glucose condition. Statistical significance ($p < 0.05$) of a protein in both contrasts is indicated by a black dot. (**E**, **F**) Volcano plots of differentially expressed proteins for low glucose (E) and alternating (F) vs. high glucose treated adipocytes. Proteins with $p < 0.05$ and fold change > 2 are highlighted in respective colors: dark gray for the high glucose, light gray for the low glucose, red for the alternating condition.

glucose concentration. Notably, the basal cell culture media contained an insulin concentration higher than under physiological conditions in order to maintain cell viability. Our current study shows that adipocytes change their proteomes in response to glucose availability. These proof-of-principle experiments must be extended to simulate adipose disease conditions; however, the technical framework is laid out herein with the presented analytical workflow.

In the future, this adipose tissue-on-a-chip model could help to unravel molecular and functional mechanisms of adipose tissue in normal and pathological conditions such as obesity.

6. Conclusion and outlook

In conclusion, the suitability of 3D printing as an alternative manufacturing technique for organ-on-a-chip devices has been demonstrated in this work. Thanks to the high resolution of current DLP printers, the printing of PDMS replica molds as well as simple monolithic devices with features as small as 25 x 75 µm (width x height) is feasible. Both, 3D printing of replica molds and direct printing of microfluidic chips, required the development of specific post-processing protocols to enable the casting of PDMS layers and culturing of human stem cells, respectively. While the PlasGRAY resin showed a good compromise between printing resolution, both in *XY* and *Z*, and surface roughness compared to the other tested resins, the GR-10 resin outperformed the other two resins in biocompatibility tests according to ISO 10093-5[240] using human iPSCs. Using the latter to 3D-print a microwell insert that fits into a standard 48-well tissue culture plate enabled the formation, maintenance, and analysis of 3D cell cultures of human iPSC. With this, hundreds of human iPSC aggregates of homogeneous size (mean diameter: 80 µm ± 11 µm) have been successfully formed by cellular self-aggregation after coating the microwells with an anti-adhesive and maintained for up to seven days without any signs of comprised viability. However, monolithic microwell inserts suffered from some limitations regarding live/dead analysis of the iPSC aggregates due to high autofluorescence in the DAPI channel (wavelength: 405 nm). This autofluorescence will likely also interfere with the more detailed phenotypic analysis of aggregates for example by immunofluorescence. To address this shortcoming in the future, 3D cell cultures could be retrieved and analyzed off-chip. For this, retrieval rates need to be optimized in the future as the current sealing method of the microwell insert with an adhesive tape impeded aggregate retrieval in experiments conducted within this work.

Despite direct printing of microfluidic devices, the presented work exploited the use of 3D printing for the fabrication of PDMS replica molds with flow channels of sufficient height to render the mLSI technique compatible with 3D cell culture. For this, an adaption of the traditional soft lithography workflow using 3D-printed flow molds was developed and design rules for functional upscaled PMVs were derived. Owing to the inherent layering process of additive manufacturing, the half-rounded flow channel on the 3D-printed molds exhibited a staircase effect on their surface, resulting in a sieve-like behavior of upscaled PMVs. Employing a grayscale light exposure strategy during printing or using a thermally processable wax-based printing resin significantly reduced the staircase effect and restored the function of upscaled PMVs. Depending on the selected optimization approach, proper valve closure was observed for a control pressure of 200 kPa or 30 kPa for the anti-aliased and reflowed wax molds, respectively.

A unique feature of upscaled PMVs fabricated by anti-aliased molds was their sieve-like characteristic at a certain control pressure range (between 100-180 kPa) which allowed for constriction of the channel to entrap entities in the size range of individual cells and simultaneously passing of fluid at a precisely controllable rate. Upscaled PMVs have thus been exploited for the design of a generic unit cell for the formation, culturing, and retrieval, of 3D cell cultures on mLSI chip platforms. This design enabled the reliable formation of 3D cell cultures of NIH3T3 fibroblasts and human stem cells (iPSCs, hASCs) through self-aggregation with homogeneous sizes.

Integration of upscaled PMVs and unit cell arrays on mLSI chip platforms enabled the unrestricted and non-destructive handling of 3D cell cultures on-chip for a variety of applications. For example, the parallel formation, culture, processing, and fusion of 3D cell cultures of two fluorescently labeled NIH3T3 cell lines within an automated flow process were performed on an mLSI-based chip platform. A second mLSI-based organ-on-a-chip device has been developed to yield a higher parallelization degree than on the first platform. The second chip was developed to automate the formation, long-term culture, and retrieval of 96 3D adipose microtissues and enable longitudinal studies of adipose tissue *in vitro*. With the combination of this platform with a mass spectrometry-based analytical pipeline, the minimum cell numbers required to obtain robust and complex proteomes with over 1800 identified proteins have been determined. The adipose microtissues on the chip platform were then used to simulate periodic food intake by alternating the glucose level in the cell-feeding media every 6 h for one week. The proteomes of treated adipocytes exhibited unique protein profiles compared to non-treated controls, confirming the technical functionality and applicability of the chip platform. In the future, this adipose tissue-on-chip *in vitro* model may prove useful for elucidating the molecular and functional mechanisms of adipose tissue in normal and pathological conditions, such as obesity.

Despite these achievements and the benefits of the mLSI technology in terms of automation and parallelization, the technique requires elaborate and highly manual manufacturing, a large operating setup and equipment as well as an experienced user, hindering the adoption of the technique in an industrial context. However, with the increasing use of additive manufacturing techniques and progress in 3D-printing active microfluidic components such as PMVs, some of mLSI’s limitations will hopefully be overcome and spur its adoption at least in academic laboratories to increase the standardization and reliability of organoid models. Ongoing efforts to couple the technology with on-chip read-out functionalities for example by the integration of biosensors[317–321] furthermore enables continuous monitoring and quantifiable analysis of the cellular microenvironment in realtime and thus, provides insights into dynamic adaptations of the 3D cell cultures upon different culture conditions. It is expected that this will also foster new developments for highly parallel 3D cell culture screening applications to gain further insights into human (patho-) physiology and facilitate the application of organ-on-a-chip devices in medical and pharmaceutical sciences.

Appendix

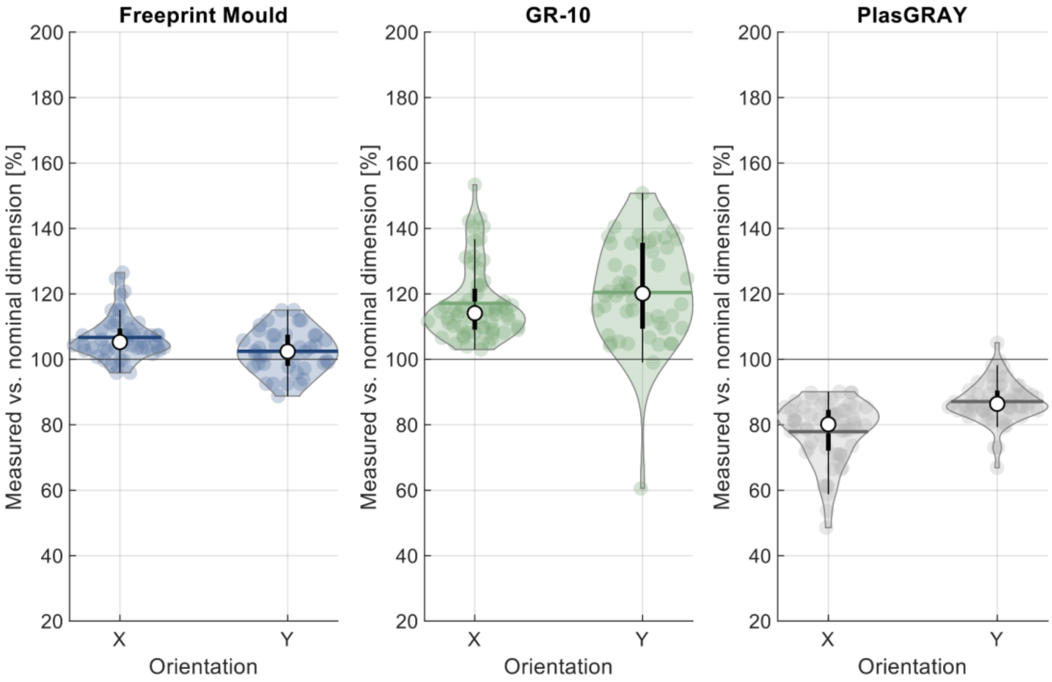

Figure A.1 Dimensional accuracy of PDMS cross-sections cast from different 3D-printed molds depending on the directional alignment of the channel. The channel axis was aligned either in X or Y direction on the building platform of the 3D printer. Displayed are the individual data points (colored points), probability density (colored structure), mean (colored line), median (white dot), and interquartile range (black bars) for the different printing resins. *N* = 2 individually printed molds with one layer of PDMS cast from each for Freeprint Mould and PlasGRAY, *N* = 1 printed mold with one layer of PDMS cast from it for GR-10.

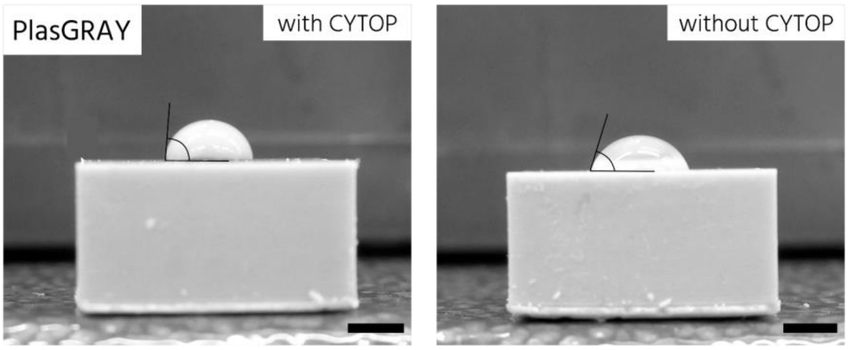

Figure A.2 Contact angle on 3D-printed PlasGRAY molds before and after CYTOP coating. The coating of the 3D-printed PlasGRAY molds with a 2% CYTOP solution increased the water contact angle, compared to the non-coated surface from 76° to 88°. Shown are representative images of a 10 µL drop of MilliQ water on top of the 3D-printed surface. Scale bars: 2 mm.

Source of variability	Sum of squares	Degrees of freedom	Mean squares	F-statistic	p-Value
Material	0.0235	1	0.02353	0.31	0.5792
Pre-extraction	3.11	1	3.11005	41.06	0
UV post-exposure	0.448	1	0.44802	5.91	0.0177
Sample volume	0.1687	1	0.16869	2.23	0.1404
Time point	9.7002	1	9.70023	128.06	0
Error	4.9994	66	0.07575		
Total	21.2099	71			

Table A.1 Results of n-way ANOVA for indirect biocompatibility testing of iPSCs for long-term extraction. The significance level alpha was set to 0.05. N-way ANOVA included the five factors listed in the first column. Levels of the factors were: material: Freeprint Mould, GR-10; pre-extraction: EtOH, none; UV post-exposure: 2x2000 flashes, none; sample volume: thick (402 mm^3), thin (201 mm^3); time point: 24 hours, 48 hours.

References

1. Jackson, E. L. & Lu, H. Three-dimensional models for studying development and disease: moving on from organisms to organs-on-a-chip and organoids. *Integr. Biol.* **8**, 672–683 (2016).
2. Bhatia, S. N. & Ingber, D. E. Microfluidic organs-on-chips. *Nat. Biotechnol.* **32**, 760–72 (2014).
3. Zheng, F. *et al.* Organ-on-a-Chip Systems: Microengineering to Biomimic Living Systems. *Small* **12**, 2253–2282 (2016).
4. Zhang, B., Korolj, A., Lai, B. F. L. & Radisic, M. Advances in organ-on-a-chip engineering. *Nat. Rev. Mater.* 1 (2018).
5. Duval, K. *et al.* Modeling physiological events in 2D vs. 3D cell culture. *Physiology* **32**, 266–277 (2017).
6. Patel, S. N. *et al.* Organoid microphysiological system preserves pancreatic islet function within 3D matrix. *Sci. Adv.* **7**, eaba5515 (2021).
7. Daoud, J. T. *et al.* Long-term in vitro human pancreatic islet culture using three-dimensional microfabricated scaffolds. *Biomaterials* **32**, 1536–1542 (2011).
8. Huch, M. & Koo, B.-K. Modeling mouse and human development using organoid cultures. *Development* **142**, 3113–3125 (2015).
9. Hohwieler, M. *et al.* Human pluripotent stem cell-derived acinar/ductal organoids generate human pancreas upon orthotopic transplantation and allow disease modelling. *Gut* **66**, 473–486 (2017).
10. Nikolaev, M. *et al.* Homeostatic mini-intestines through scaffold-guided organoid morphogenesis. *Nature* **in Press**, (2020).
11. Xiang, Y. *et al.* hESC-Derived Thalamic Organoids Form Reciprocal Projections When Fused with Cortical Organoids. *Cell Stem Cell* **24**, 487-497.e7 (2019).
12. Hushka, E. A., Yavitt, F. M., Brown, T. E., Dempsey, P. J. & Anseth, K. S. Relaxation of Extracellular Matrix Forces Directs Crypt Formation and Architecture in Intestinal Organoids. *Adv. Healthc. Mater.* **9**, 1901214 (2020).
13. Wiedenmann, S. *et al.* Single-cell-resolved differentiation of human induced pluripotent stem cells into pancreatic duct-like organoids on a microwell chip. *Nat. Biomed. Eng.* **5**, 897–913 (2021).
14. Brandenberg, N. *et al.* High-throughput automated organoid culture via stem-cell aggregation in microcavity arrays. *Nat. Biomed. Eng.* (2020) doi:10.1038/s41551-020-0565-2.
15. Takebe, T., Zhang, B. & Radisic, M. Synergistic Engineering: Organoids Meet Organs-on-a-Chip. *Cell Stem Cell* **21**, 297–300 (2017).
16. Liu, W. *et al.* Dynamic trapping and high-throughput patterning of cells using pneumatic microstructures in an integrated microfluidic device. *Lab Chip* **12**, 1702 (2012).
17. Sinha, R. *et al.* Endothelial cell alignment as a result of anisotropic strain and flow induced shear stress combinations. *Sci. Rep.* **6**, 1–12 (2016).
18. Vera, D. *et al.* Engineering Tissue Barrier Models on Hydrogel Microfluidic Platforms. *ACS Applied Materials and Interfaces* vol. 13 13920–13933 (2021).
19. Probst, C., Schneider, S. & Loskill, P. High-throughput Organ-on-a-chip systems: Current status and remaining challenges. *Curr. Opin. Biomed. Eng.* **6**, 33–41 (2018).
20. Ramadan, Q. & Zourob, M. Organ-on-a-chip engineering: Toward bridging the gap between lab and industry. *Biomicrofluidics* **14**, (2020).
21. Melin, J. & Quake, S. R. Microfluidic large-scale integration: the evolution of design

rules for biological automation. *Annu. Rev. Biophys. Biomol. Struct.* **36**, 213–231 (2007).

22. Zhang, C. *et al.* Ultra-multiplexed analysis of single-cell dynamics reveals logic rules in differentiation. *Sci. Adv.* **5**, 1–11 (2019).
23. Wu, X. *et al.* In situ characterization of the mTORC1 during adipogenesis of human adult stem cells on chip. *Proc. Natl. Acad. Sci. U. S. A.* **113**, E4143–E4150 (2016).
24. Ardila Riveros, J. C. *et al.* Automated optimization of endoderm differentiation on chip. *Lab Chip* **21**, 4685–4695 (2021).
25. Vollertsen, A. R. *et al.* Highly parallelized human embryonic stem cell differentiation to cardiac mesoderm in nanoliter chambers on a microfluidic chip. *Biomed. Microdevices* **23**, 3 (2021).
26. Frank, T. & Tay, S. Automated co-culture system for spatiotemporal analysis of cell-to-cell communication. *Lab Chip* **15**, 2192–2200 (2015).
27. Swank, Z. *et al.* A high-throughput microfluidic nanoimmunoassay for detecting anti–SARS-CoV-2 antibodies in serum or ultralow-volume blood samples. *Proc. Natl. Acad. Sci.* **118**, e2025289118 (2021).
28. Rodriguez-Moncayo, R. *et al.* A high-throughput multiplexed microfluidic device for COVID-19 serology assays. *Lab Chip* **21**, 93–104 (2021).
29. Zhang, Y., Zhang, W. & Qin, L. Mesenchymal-mode migration assay and antimetastatic drug screening with high-throughput microfluidic channel networks. *Angew. Chemie - Int. Ed.* **53**, 2344–2348 (2014).
30. Liu, W., Sun, M., Han, K. & Wang, J. Large-Scale Antitumor Screening Based on Heterotypic 3D Tumors Using an Integrated Microfluidic Platform. *Anal. Chem.* **91**, 13601–13610 (2019).
31. Moshksayan, K. *et al.* Spheroids-on-a-chip: Recent advances and design considerations in microfluidic platforms for spheroid formation and culture. *Sensors and Actuators, B: Chemical* vol. 263 151–176 (2018).
32. Silva Santisteban, T., Rabajania, O., Kalinina, I., Robinson, S. & Meier, M. Rapid spheroid clearing on a microfluidic chip. *Lab Chip* **18**, 153–161 (2018).
33. Unger, M. A., Chou, H.-P., Thorsen, T., Scherer, A. & Quake, S. R. Monolithic microfabricated valves and pumps by multilayer soft lithography. *Science (80-.).* **288**, 113–116 (2000).
34. Bartlett, N. W. & Wood, R. J. Comparative analysis of fabrication methods for achieving rounded microchannels in PDMS. *J. Micromechanics Microengineering* **26**, 115013 (2016).
35. Kuo, A. P. *et al.* High-Precision Stereolithography of Biomicrofluidic Devices. *Adv. Mater. Technol.* 1800395 (2019) doi:10.1002/admt.201800395.
36. Hwang, Y., Paydar, O. H. & Candler, R. N. 3D printed molds for non-planar PDMS microfluidic channels. *Sensors Actuators A Phys.* **226**, 137–142 (2015).
37. Parthiban, P., Vijayan, S., Doyle, P. S. & Hashimoto, M. Evaluation of 3D-printed molds for fabrication of non-planar microchannels. *Biomicrofluidics* **15**, 024111 (2021).
38. Kinstlinger, I. S. *et al.* Generation of model tissues with dendritic vascular networks via sacrificial laser-sintered carbohydrate templates. *Nat. Biomed. Eng.* **4**, (2020).
39. Brooks, J. C., Ford, K. I., Holder, D. H., Holtan, M. D. & Easley, C. J. Macro-to-micro interfacing to microfluidic channels using 3D-printed templates: Application to time-resolved secretion sampling of endocrine tissue. *Analyst* **141**, 5714–5721 (2016).
40. Gong, H., Woolley, A. T. & Nordin, G. P. 3D printed high density, reversible, chip-to-chip microfluidic interconnects. *Lab Chip* **18**, 639–647 (2018).
41. Bhargava, K. C., Thompson, B. & Malmstadt, N. Discrete elements for 3D

microfluidics. *Proc. Natl. Acad. Sci. U. S. A.* **111**, 15013–15018 (2014).

42. Lai, X. *et al.* A Rubik's microfluidic cube. *Microsystems Nanoeng.* **6**, (2020).
43. Ong, L. J. Y. *et al.* A 3D printed microfluidic perfusion device for multicellular spheroid cultures. *Biofabrication* **9**, 045005 (2017).
44. Zips, S. *et al.* Biocompatible, Flexible, and Oxygen-Permeable Silicone-Hydrogel Material for Stereolithographic Printing of Microfluidic Lab-On-A-Chip and Cell-Culture Devices. *ACS Appl. Polym. Mater.* acsapm.0c01071 (2020) doi:10.1021/acsapm.0c01071.
45. Bhattacharjee, N., Urrios, A., Kang, S. & Folch, A. The upcoming 3D-printing revolution in microfluidics. *Lab Chip* **16**, 1720–1742 (2016).
46. Mehta, V. & Rath, S. N. 3D printed microfluidic devices: a review focused on four fundamental manufacturing approaches and implications on the field of healthcare. *Bio-Design Manuf.* (2021) doi:10.1007/s42242-020-00112-5.
47. Takahashi, K. *et al.* Induction of Pluripotent Stem Cells from Adult Human Fibroblasts by Defined Factors. *Cell* **131**, 861–872 (2007).
48. Rifes, P. *et al.* Modeling neural tube development by differentiation of human embryonic stem cells in a microfluidic WNT gradient. *Nat. Biotechnol.* (2020) doi:10.1038/s41587-020-0525-0.
49. Homan, K. A. *et al.* Flow-enhanced vascularization and maturation of kidney organoids in vitro. *Nat. Methods* **16**, 255–262 (2019).
50. Koike, H. *et al.* Modelling human hepato-biliary-pancreatic organogenesis from the foregut–midgut boundary. *Nature* **574**, 112–116 (2019).
51. Laschke, M. W. & Menger, M. D. Life is 3D: Boosting Spheroid Function for Tissue Engineering. *Trends Biotechnol.* **35**, 133–144 (2017).
52. Yang, F. *et al.* A 3D human adipose tissue model within a microfluidic device. *Lab Chip* **21**, 435–446 (2021).
53. Su, C. *et al.* A novel human arterial wall-on-a-chip to study endothelial inflammation and vascular smooth muscle cell migration in early atherosclerosis. *Lab Chip* **21**, 2359–2371 (2021).
54. Campbell, J. J., Davidenko, N., Caffarel, M. M., Cameron, R. E. & Watson, C. J. A multifunctional 3D co-culture system for studies of mammary tissue morphogenesis and stem cell biology. *PLoS One* **6**, 1–9 (2011).
55. Akther, F., Little, P., Li, Z., Nguyen, N. T. & Ta, H. T. Hydrogels as artificial matrices for cell seeding in microfluidic devices. *RSC Adv.* **10**, 43682–43703 (2020).
56. Jeske, R. *et al.* Agitation in a microcarrier-based spinner flask bioreactor modulates homeostasis of human mesenchymal stem cells. *Biochem. Eng. J.* **168**, 107947 (2021).
57. Klingelhutz, A. J. *et al.* Scaffold-free generation of uniform adipose spheroids for metabolism research and drug discovery. *Sci. Rep.* **8**, 1–12 (2018).
58. Lin, R.-Z. & Chang, H.-Y. Recent advances in three-dimensional multicellular spheroid culture for biomedical research. *Biotechnol. J.* **3**, 1172–1184 (2008).
59. Zuellig, R. A. *et al.* Improved physiological properties of gravity-enforced reassembled rat and human pancreatic pseudo-islets. *J. Tissue Eng. Regen. Med.* **11**, 109–120 (2017).
60. Boos, J. A., Misun, P. M., Michlmayr, A., Hierlemann, A. & Frey, O. Microfluidic Multitissue Platform for Advanced Embryotoxicity Testing In Vitro. *Adv. Sci.* **6**, (2019).
61. Marimuthu, M. *et al.* Multi-size spheroid formation using microfluidic funnels. *Lab Chip* **18**, 304–314 (2018).
62. Liu, D., Chen, S. & Naing, M. W. A review of manufacturing capabilities of cell spheroid generation technologies and future development. *Biotechnol. Bioeng.* **25**, bit.27620 (2020).

63. Al-Ghadban, S., Pursell, I. A., Diaz, Z. T., Herbst, K. L. & Bunnell, B. A. 3D Spheroids Derived From Human Lipedema Ascs Demonstrated Similar Adipogenic Differentiation Potential and Ecm Remodeling To Non-Lipedema Ascs in Vitro. *Int. J. Mol. Sci.* **21**, 1–14 (2020).
64. Lee, G. *et al.* Generation of uniform liver spheroids from human pluripotent stem cells for imaging-based drug toxicity analysis. *Biomaterials* **269**, 120529 (2021).
65. Chen, B. *et al.* High-throughput acoustofluidic fabrication of tumor spheroids. *Lab Chip* **19**, 1755–1763 (2019).
66. Shinohara, M. *et al.* Combination of microwell structures and direct oxygenation enables efficient and size-regulated aggregate formation of an insulin-secreting pancreatic β-cell line. *Biotechnol. Prog.* **30**, 178–187 (2014).
67. Kim, K., Kim, S. H., Lee, G. H. & Park, J. Y. Fabrication of omega-shaped microwell arrays for a spheroid culture platform using pins of a commercial CPU to minimize cell loss and crosstalk. *Biofabrication* **10**, 045003 (2018).
68. Ma, L.-D. *et al.* Design and fabrication of a liver-on-a-chip platform for convenient, high-efficient, and safe in situ perfusion culture of 3D hepatic spheroids. *Lab Chip* **18**, 2547–2562 (2018).
69. Schulze, T. *et al.* A 3D microfluidic perfusion system made from glass for multiparametric analysis of stimulus-secretioncoupling in pancreatic islets. *Biomed. Microdevices* **19**, 47 (2017).
70. Barisam, M., Saidi, M. S., Kashaninejad, N. & Nguyen, N. T. Prediction of necrotic core and hypoxic zone of multicellular spheroids in a microbioreactor with a U-shaped barrier. *Micromachines* **9**, 94 (2018).
71. Davenport, C., Diekmann, U., Budde, I., Detering, N. & Naujok, O. Anterior-Posterior Patterning of Definitive Endoderm Generated from Human Embryonic Stem Cells Depends on the Differential Signaling of Retinoic Acid, Wnt-, and BMP-Signaling. *Stem Cells* **34**, 2635–2647 (2016).
72. Broutier, L. *et al.* Culture and establishment of self-renewing human and mouse adult liver and pancreas 3D organoids and their genetic manipulation. *Nat. Protoc.* **11**, 1724 (2016).
73. Torizal, F. G., Kimura, K., Horiguchi, I. & Sakai, Y. Size-dependent hepatic differentiation of human induced pluripotent stem cells spheroid in suspension culture. *Regen. Ther.* **12**, 66–73 (2019).
74. Song, L. *et al.* Neural Differentiation of Spheroids Derived from Human Induced Pluripotent Stem Cells-Mesenchymal Stem Cells Coculture. *Tissue Eng. - Part A* **24**, 915–929 (2018).
75. Takebe, T. & Wells, J. M. Organoids by design. *Science (80-.).* **364**, 956–959 (2019).
76. Kim, J., Koo, B.-K. & Knoblich, J. A. Human organoids: model systems for human biology and medicine. *Nat. Rev. Mol. Cell Biol.* **21**, 571–584 (2020).
77. Brassard, J. A. & Lutolf, M. P. Engineering Stem Cell Self-organization to Build Better Organoids. *Cell Stem Cell* **24**, 860–876 (2019).
78. Mamidi, A. *et al.* Mechanosignalling via integrins directs fate decisions of pancreatic progenitors. *Nature* **564**, 114–118 (2018).
79. McBeath, R., Pirone, D. M., Nelson, C. M., Bhadriraju, K. & Chen, C. S. Cell Shape, Cytoskeletal Tension, and RhoA Regulate Stem Cell Lineage Commitment. *Dev. Cell* **6**, 483–495 (2004).
80. Chen, C. S., Mrksich, M., Huang, S., Whitesides, G. M. & Ingber, D. E. Geometric Control of Cell Life and Death. *Science (80-.).* **276**, 1425–1428 (1997).
81. Sart, S. *et al.* Mapping the structure and biological functions within mesenchymal bodies

using microfluidics. *Sci. Adv.* **6**, (2020).

82. Lee, S. H. *et al.* Microphysiological Analysis Platform of Pancreatic Islet β-Cell Spheroids. *Adv. Healthc. Mater.* **7**, 1701111 (2018).
83. Liu, W., Wang, J.-C. & Wang, J. Controllable organization and high throughput production of recoverable 3D tumors using pneumatic microfluidics. *Lab Chip* **15**, 1195–1204 (2015).
84. Wu, L. Y., Di Carlo, D. & Lee, L. P. Microfluidic self-assembly of tumor spheroids for anticancer drug discovery. *Biomed. Microdevices* **10**, 197–202 (2008).
85. Kim, H. S., Devarenne, T. P. & Han, A. A high-throughput microfluidic single-cell screening platform capable of selective cell extraction. *Lab Chip* **15**, 2467–2475 (2015).
86. Di Carlo, D., Wu, L. Y. & Lee, L. P. Dynamic single cell culture array. *Lab Chip* **6**, 1445–1449 (2006).
87. Fu, C. Y. *et al.* A microfluidic chip with a U-shaped microstructure array for multicellular spheroid formation, culturing and analysis. *Biofabrication* **6**, (2014).
88. Wang, Y., Wang, H., Deng, P., Chen, W. & Guo, Y. In situ differentiation and generation of functional liver organoids from human iPSCs in a 3D perfusable chip system. *Lab Chip* (2018) doi:10.1039/c8lc00869h.
89. Paek, J. *et al.* Microphysiological Engineering of Self-Assembled and Perfusable Microvascular Beds for the Production of Vascularized Three-Dimensional Human Microtissues. *ACS Nano* **13**, 7627–7643 (2019).
90. Neufeld, L. *et al.* Microengineered perfusable 3D-bioprinted glioblastoma model for in vivo mimicry of tumor microenvironment. *Sci. Adv.* **7**, eabi9119 (2021).
91. Nguyen, D. H. T. *et al.* Biomimetic model to reconstitute angiogenic sprouting morphogenesis in vitro. *Proc. Natl. Acad. Sci. U. S. A.* **110**, 6712–6717 (2013).
92. Shahin-Shamsabadi, A. & Selvaganapathy, P. R. A 3D Self-Assembled In Vitro Model to Simulate Direct and Indirect Interactions between Adipocytes and Skeletal Muscle Cells. *Adv. Biosyst.* **4**, 2000034 (2020).
93. Knowlton, S. *et al.* 3D-printed microfluidic chips with patterned, cell-laden hydrogel constructs. *Biofabrication* **8**, 025019 (2016).
94. Godwin, L. A. *et al.* A microfluidic interface for the culture and sampling of adiponectin from primary adipocytes. *Analyst* **140**, 1019–1025 (2015).
95. Toh, Y. C., Blagovic, K., Yu, H. & Voldman, J. Spatially organized in vitro models instruct asymmetric stem cell differentiation. *Integr. Biol.* **3**, 1179–1187 (2011).
96. Egger, D. & Nebel, S. Introduction to 3D Cell Culture. in 1–26 (Springer, Cham, 2021). doi:10.1007/978-3-030-66749-8_1.
97. Compera, N., Atwell, S., Wirth, J., Wolfrum, B. & Meier, M. Upscaling of pneumatic membrane valves for the integration of 3D cell cultures on chip. *Lab Chip* **21**(15), 2986–2996 (2021).
98. Chou, D. B. *et al.* On-chip recapitulation of clinical bone marrow toxicities and patient-specific pathophysiology. *Nat. Biomed. Eng.* (2020) doi:10.1038/s41551-019-0495-z.
99. Kim, J. Y., Fluri, D. A., Kelm, J. M., Hierlemann, A. & Frey, O. 96-Well Format-Based Microfluidic Platform for Parallel Interconnection of Multiple Multicellular Spheroids. *J. Lab. Autom.* **20**, 274–282 (2015).
100. Liu, Y., Kongsuphol, P., Gourikutty, S. B. N. & Ramadan, Q. Human adipocyte differentiation and characterization in a perfusion-based cell culture device. *Biomed. Microdevices* **19**, 1–10 (2017).
101. Jun, Y. *et al.* In vivo–mimicking microfluidic perfusion culture of pancreatic islet spheroids. *Sci. Adv.* **5**, (2019).
102. Jackson-Holmes, E. L., Schaefer, A. W., McDevitt, T. C. & Lu, H. Microfluidic

perfusion modulates growth and motor neuron differentiation of stem cell aggregates. *Analyst* **145**, 4815–4826 (2020).

103. Liu, W. *et al.* An integrated microfluidic 3D tumor system for parallel and high-throughput chemotherapy evaluation. *Analyst* **145**, 6447–6455 (2020).
104. Rogal, J. *et al.* WAT-on-a-chip integrating human mature white adipocytes for mechanistic research and pharmaceutical applications. *Sci. Rep.* **10**, 1–12 (2020).
105. Kongsuphol, P. *et al.* In vitro micro-physiological model of the inflamed human adipose tissue for immune-metabolic analysis in type II diabetes. *Sci. Rep.* **9**, 1–14 (2019).
106. van Duinen, V. *et al.* Perfused 3D angiogenic sprouting in a high-throughput in vitro platform. *Angiogenesis* **22**, 157–165 (2019).
107. Belair, D. G. *et al.* Human Vascular Tissue Models Formed from Human Induced Pluripotent Stem Cell Derived Endothelial Cells. *Stem Cell Rev. Reports* **11**, 511–525 (2015).
108. Loskill, P. *et al.* WAT-on-a-chip: a physiologically relevant microfluidic system incorporating white adipose tissue. *Lab Chip* **17**, 1645–1654 (2017).
109. Tanataweethum, N. *et al.* Towards an Insulin Resistant Adipose Model on a Chip. *Cell. Mol. Bioeng.* **14**, 89–99 (2021).
110. Sohrabi Kashani, A. & Packirisamy, M. Efficient Low Shear Flow-based Trapping of Biological Entities. *Sci. Rep.* **9**, 5511 (2019).
111. Connolly, S., Newport, D. & McGourty, K. Cell specific variation in viability in suspension in in vitro Poiseuille flow conditions. *Sci. Rep.* **11**, 13997 (2021).
112. Shin, W. *et al.* Spatiotemporal Gradient and Instability of Wnt Induce Heterogeneous Growth and Differentiation of Human Intestinal Organoids. *iScience* **23**, 101372 (2020).
113. Cristancho, A. G. & Lazar, M. A. Forming functional fat: A growing understanding of adipocyte differentiation. *Nat. Rev. Mol. Cell Biol.* **12**, 722–734 (2011).
114. Harrison, S. E., Sozen, B., Christodoulou, N., Kyprianou, C. & Zernicka-Goetz, M. Assembly of embryonic and extraembryonic stem cells to mimic embryogenesis in vitro. *Science (80-.).* **356**, (2017).
115. Soltanian, A. *et al.* Generation of functional human pancreatic organoids by transplants of embryonic stem cell derivatives in a 3D-printed tissue trapper. *J. Cell. Physiol.* **234**, 9564–9576 (2019).
116. Sheehy, S. P. *et al.* Toward improved myocardial maturity in an organ-on-chip platform with immature cardiac myocytes. *Exp. Biol. Med.* **242**, 1643–1656 (2017).
117. Zhang, X., Li, L. & Luo, C. Gel integration for microfluidic applications. *Lab Chip* **16**, 1757–1776 (2016).
118. Nie, J., Fu, J. & He, Y. Hydrogels: The Next Generation Body Materials for Microfluidic Chips? *Small* vol. 16 2003797 (2020).
119. Kietzmann, T. Metabolic zonation of the liver: The oxygen gradient revisited. *Redox Biology* vol. 11 622–630 (2017).
120. Lee-Montiel, F. T. *et al.* Control of oxygen tension recapitulates zone-specific functions in human liver microphysiology systems. *Exp. Biol. Med.* **242**, 1617–1632 (2017).
121. Rivera, K. R., Yokus, M. A., Erb, P. D., Pozdin, V. A. & Daniele, M. Measuring and regulating oxygen levels in microphysiological systems: design, material, and sensor considerations. *Analyst* **144**, 3190–3215 (2019).
122. Danoy, M. *et al.* Characterization of liver zonation-like transcriptomic patterns in HLCs derived from hiPSCs in a microfluidic biochip environment. *Biotechnol. Prog.* **36**, e3013 (2020).
123. Bulutoglu, B. *et al.* A microfluidic patterned model of non-alcoholic fatty liver disease: applications to disease progression and zonation. *Lab Chip* **19**, 3022–3031 (2019).

124. Kang, Y. B., Eo, J., Bulutoglu, B., Yarmush, M. L. & Usta, O. B. Progressive hypoxia-on-a-chip: An in vitro oxygen gradient model for capturing the effects of hypoxia on primary hepatocytes in health and disease. *Biotechnol. Bioeng.* **117**, 763–775 (2020).
125. Nashimoto, Y. *et al.* Vascularized cancer on a chip: The effect of perfusion on growth and drug delivery of tumor spheroid. *Biomaterials* **229**, 119547 (2020).
126. Paul, N. E. *et al.* The effect of mechanical stress on the proliferation, adipogenic differentiation and gene expression of human adipose-derived stem cells. *J. Tissue Eng. Regen. Med.* **12**, 276–284 (2018).
127. Takebe, T. *et al.* Vascularized and complex organ buds from diverse tissues via mesenchymal cell-driven condensation. *Cell Stem Cell* **16**, 556–565 (2015).
128. Grassart, A. *et al.* Bioengineered Human Organ-on-Chip Reveals Intestinal Microenvironment and Mechanical Forces Impacting Shigella Infection. *Cell Host Microbe* **26**, 435-444.e4 (2019).
129. Sun, Y., Chen, C. S. & Fu, J. Forcing stem cells to behave: A biophysical perspective of the cellular microenvironment. *Annual Review of Biophysics* vol. 41 519–542 (2012).
130. Inagaki, T. *et al.* Endocrine Regulation of the Fasting Response by PPARα-Mediated Induction of Fibroblast Growth Factor 21. *Cell Metab.* **5**, 415–425 (2007).
131. Sung, J. H. *et al.* Recent Advances in Body-on-a-Chip Systems. *Anal. Chem.* **91**, 330–351 (2019).
132. Suri, S. *et al.* Microfluidic-based patterning of embryonic stem cells for in vitro development studies. *Lab Chip* **13**, 4617–4624 (2013).
133. Zhao, L., Liu, Y. Y., Liu, Y. Y., Zhang, M. & Zhang, X. Microfluidic Control of Tumor and Stromal Cell Spheroids Pairing and Merging for Three-Dimensional Metastasis Study. *Anal. Chem.* **0**, (2020).
134. Rogers, M. T. *et al.* A high-throughput microfluidic bilayer co-culture platform to study endothelial-pericyte interactions. *Sci. Rep.* **11**, 12225 (2021).
135. Yu, J. *et al.* Reconfigurable open microfluidics for studying the spatiotemporal dynamics of paracrine signalling. *Nat. Biomed. Eng.* 1–12 (2019) doi:10.1038/s41551-019-0421-4.
136. Liu, Y. *et al.* Adipose-on-a-chip: a dynamic microphysiological in vitro model of the human adipose for immune-metabolic analysis in type II diabetes. *Lab Chip* **19**, 241–253 (2019).
137. Ramadan, Q., Nair Gourikutty, S. B. & Zhang, Q. OOCHIP: Compartmentalized microfluidic perfusion system with porous barriers for enhanced cell-cell crosstalk in organ-on-a-chip. *Micromachines* **11**, (2020).
138. Campbell, S. *et al.* Beyond polydimethylsiloxane: Alternative materials for fabrication of organ on a chip devices and microphysiological systems. *ACS Biomater. Sci. Eng.* acsbiomaterials.0c00640 (2020) doi:10.1021/acsbiomaterials.0c00640.
139. Schneider, S., Brás, E. J. S., Schneider, O., Schlünder, K. & Loskill, P. Facile Patterning of Thermoplastic Elastomers and Robust Bonding to Glass and Thermoplastics for Microfluidic Cell Culture and Organ-on-Chip. *Micromachines* **12**, 575 (2021).
140. McMillan, A. H. *et al.* Rapid Fabrication of Membrane-Integrated Thermoplastic Elastomer Microfluidic Devices. *Micromachines* **11**, 731 (2020).
141. Sackmann, E. K., Fulton, A. L. & Beebe, D. J. The present and future role of microfluidics in biomedical research. *Nature* **507**, 181 (2014).
142. Wang, J. D., Douville, N. J., Takayama, S. & Elsayed, M. Quantitative analysis of molecular absorption into PDMS microfluidic channels. *Ann. Biomed. Eng.* **40**, 1862–1873 (2012).
143. Moore, T. A., Brodersen, P. & Young, E. W. K. Multiple Myeloma Cell Drug Responses

Differ in Thermoplastic vs PDMS Microfluidic Devices. *Anal. Chem.* **89**, 11391–11398 (2017).

144. Tatárová, Z., Abbuehl, J. P., Maerkl, S. & Huelsken, J. Microfluidic co-culture platform to quantify chemdotaxis of primary stem cells. *Lab Chip* **16**, 1934–1945 (2016).
145. Lohasz, C., Rousset, N., Renggli, K., Hierlemann, A. & Frey, O. Scalable Microfluidic Platform for Flexible Configuration of and Experiments with Microtissue Multiorgan Models. *SLAS Technol.* **24**, 79–95 (2019).
146. Ko, J. *et al.* Tumor spheroid-on-a-chip: A standardized microfluidic culture platform for investigating tumor angiogenesis. *Lab Chip* **19**, 2822–2833 (2019).
147. Domansky, K. *et al.* SEBS elastomers for fabrication of microfluidic devices with reduced drug absorption by injection molding and extrusion. *Microfluid. Nanofluidics* **21**, 107 (2017).
148. Day, J. H. *et al.* Injection molded open microfluidic well plate inserts for user-friendly coculture and microscopy. *Lab Chip* **20**, 107–119 (2020).
149. Berthier, E., Young, E. W. K. & Beebe, D. Engineers are from PDMS-land, Biologists are from Polystyrenia. *Lab Chip* **12**, 1224 (2012).
150. Roy, E., Geissler, M., Galas, J. C. & Veres, T. Prototyping of microfluidic systems using a commercial thermoplastic elastomer. *Microfluid. Nanofluidics* **11**, 235–244 (2011).
151. Schneider, S., Gruner, D., Richter, A. & Loskill, P. Membrane integration into PDMS-free microfluidic platforms for organ-on-chip and analytical chemistry applications. *Lab Chip* **21**, 1866–1885 (2021).
152. Vollertsen, A. R. *et al.* Modular operation of microfluidic chips for highly parallelized cell culture and liquid dosing via a fluidic circuit board. *Microsystems Nanoeng.* **6**, 107 (2020).
153. Brassard, D. *et al.* 3D thermoplastic elastomer microfluidic devices for biological probe immobilization. *Lab Chip* **11**, 4099 (2011).
154. Shaegh, S. A. M. *et al.* Rapid prototyping of whole-thermoplastic microfluidics with built-in microvalves using laser ablation and thermal fusion bonding. *Sensors Actuators, B Chem.* **255**, 100–109 (2018).
155. Skafte-Pedersen, P., Sip, C. G., Folch, A. & Dufva, M. Modular microfluidic systems using reversibly attached PDMS fluid control modules. *J. Micromechanics Microengineering* **23**, 055011 (2013).
156. Rodriguez, A. D. *et al.* A microfluidic platform for functional testing of cancer drugs on intact tumor slices. *Lab Chip* **20**, 1658–1675 (2020).
157. Horowitz, L. F. *et al.* Microdissected “cuboids” for microfluidic drug testing of intact tissues. *Lab Chip* (2020) doi:10.1039/D0LC00801J.
158. Park, S. E., Georgescu, A. & Huh, D. Organoids-on-a-chip. *Science (80-.).* **364**, 960–965 (2019).
159. Laurent, J. *et al.* Convergence of microengineering and cellular self-organization towards functional tissue manufacturing. *Nature Biomedical Engineering* vol. 1 939–956 (2017).
160. Phan, D. T. T. *et al.* A vascularized and perfused organ-on-a-chip platform for large-scale drug screening applications. *Lab Chip* **17**, 511–520 (2017).
161. Patra, B., Peng, C.-C., Liao, W.-H., Lee, C.-H. & Tung, Y.-C. Drug testing and flow cytometry analysis on a large number of uniform sized tumor spheroids using a microfluidic device. *Sci. Rep.* **6**, 21061 (2016).
162. Hirano, K. *et al.* Closed-channel culture system for efficient and reproducible differentiation of human pluripotent stem cells into islet cells. *Biochem. Biophys. Res. Commun.* **487**, 344–350 (2017).

163. Truong, V. *et al.* Automating Human Induced Pluripotent Stem Cell Culture and Differentiation of iPSC-Derived Retinal Pigment Epithelium for Personalized Drug Testing. *SLAS Technol. Transl. Life Sci. Innov.* **26**, 287–299 (2021).
164. Schuster, B. *et al.* Automated microfluidic platform for dynamic and combinatorial drug screening of tumor organoids. *Nat. Commun.* **11**, 5271 (2020).
165. Novak, R. *et al.* Robotic fluidic coupling and interrogation of multiple vascularized organ chips. *Nat. Biomed. Eng.* **4**, 407–420 (2020).
166. Herland, A. *et al.* Quantitative prediction of human pharmacokinetic responses to drugs via fluidically coupled vascularized organ chips. *Nat. Biomed. Eng.* (2020) doi:10.1038/s41551-019-0498-9.
167. Giobbe, G. G. *et al.* Functional differentiation of human pluripotent stem cells on a chip. *Nat. Methods* **12**, 637–640 (2015).
168. Michielin, F. *et al.* The Microfluidic Environment Reveals a Hidden Role of Self-Organizing Extracellular Matrix in Hepatic Commitment and Organoid Formation of hiPSCs. *Cell Rep.* **33**, 108453 (2020).
169. Dadgar, N. *et al.* A microfluidic platform for cultivating ovarian cancer spheroids and testing their responses to chemotherapies. *Microsystems Nanoeng.* **6**, 1–12 (2020).
170. Tomasi, R. F.-X., Sart, S., Champetier, T. & Baroud, C. N. Individual Control and Quantification of 3D Spheroids in a High-Density Microfluidic Droplet Array. *Cell Rep.* **31**, 107670 (2020).
171. Saint-Sardos, A. *et al.* High-Throughput Measurements of Intra-Cellular and Secreted Cytokine from Single Spheroids Using Anchored Microfluidic Droplets. *Small* **16**, 2002303 (2020).
172. Rothbauer, M., Rosser, J. M., Zirath, H. & Ertl, P. Tomorrow today: organ-on-a-chip advances towards clinically relevant pharmaceutical and medical in vitro models. *Curr. Opin. Biotechnol.* **55**, 81–86 (2019).
173. Tian, C., Tu, Q., Liu, W. & Wang, J. Recent advances in microfluidic technologies for organ-on-a-chip. *TrAC - Trends in Analytical Chemistry* (2019) doi:10.1016/j.trac.2019.06.005.
174. Song, Y., Cheng, D. & Zhao, L. *Microfluidics: Fundamentals, Devices, and Applications*. *Wiley* (2018).
175. Tabeling, P. *Introduction to microfluidics*. (OUP Oxford, 2005).
176. Oh, K. W., Lee, K., Ahn, B. & Furlani, E. P. Design of pressure-driven microfluidic networks using electric circuit analogy. *Lab on a Chip* vol. 12 515–545 (2012).
177. Blazek, M., Wu, X., Zengerle, R. & Meier, M. Analysis of fast protein phosphorylation kinetics in single cells on a microfluidic chip. in *18th International Conference on Miniaturized Systems for Chemistry and Life Sciences, MicroTAS 2014* vol. 15 267–269 (Royal Society of Chemistry, 2014).
178. Fordyce, P. M., Diaz-Botia, C. A., DeRisi, J. L. & Gomez-Sjoberg, R. Systematic characterization of feature dimensions and closing pressures for microfluidic valves produced via photoresist reflow. *Lab Chip* **12**, 4287 (2012).
179. Baek, J. Y., Park, J. Y., Ju, J. Il, Lee, T. S. & Lee, S. H. A pneumatically controllable flexible and polymeric microfluidic valve fabricated via in situ development. *J. Micromechanics Microengineering* **15**, 1015–1020 (2005).
180. Hua, Z. *et al.* A versatile microreactor platform featuring a chemical-resistant microvalve array for addressable multiplex syntheses and assays. *J. Micromechanics Microengineering* **16**, 1433–1443 (2006).
181. Kuo, C. C., Chen, C. M. & Chang, S. X. Polishing mechanism for ABS parts fabricated by additive manufacturing. *Int. J. Adv. Manuf. Technol.* **91**, 1473–1479 (2017).

182. Hansson, J., Hillmering, M., Haraldsson, T. & Van Der Wijngaart, W. Leak-tight vertical membrane microvalves. *Lab Chip* **16**, 1439–1446 (2016).
183. Lee, Y.-S., Bhattacharjee, N. & Folch, A. 3D-printed Quake-style microvalves and micropumps. *Lab Chip* **18**, 1207–1214 (2018).
184. Haeberle, S. & Zengerle, R. Microfluidic platforms for lab-on-a-chip applications. *Lab Chip* **7**, 1094–1110 (2007).
185. Hansen, C. L., Sommer, M. O. A. & Quake, S. R. Systematic investigation of protein phase behavior with a microfluidic formulator. *Proc. Natl. Acad. Sci.* **101**, 14431–14436 (2004).
186. Thorsen, T., Maerkl, S. J. & Quake, S. R. Microfluidic large-scale integration. *Science (80-.).* **298**, 580–584 (2002).
187. Gómez-Sjöberg, R., Leyrat, A. A., Pirone, D. M., Chen, C. S. & Quake, S. R. Versatile, Fully Automated, Microfluidic Cell Culture System. *Anal. Chem.* **79**, 8557–8563 (2007).
188. Woodruff, K. & Maerkl, S. J. A High-Throughput Microfluidic Platform for Mammalian Cell Transfection and Culturing. *Sci. Rep.* **6**, 1–12 (2016).
189. Fan, H. C., Wang, J., Potanina, A. & Quake, S. R. Whole-genome molecular haplotyping of single cells. *Nat. Biotechnol.* **29**, 51–57 (2011).
190. Eddings, M. A., Johnson, M. A. & Gale, B. K. Determining the optimal PDMS-PDMS bonding technique for microfluidic devices. *J. Micromechanics Microengineering* **18**, 067001 (2008).
191. Frank, P., Haefner, S., Paschew, G. & Richter, A. Rounding of negative dry film resist by diffusive backside exposure creating rounded channels for pneumatic membrane valves. *Micromachines* **6**, 1588–1596 (2015).
192. Freitas, D. N., Mongersun, A., Chau, H. & Araci, I. E. Tunable soft lithography molds enable rapid-prototyping of multi-height channels for microfluidic large-scale integration. *J. Micromechanics Microengineering* **29**, aafd9c (2019).
193. Vecchione, R., Pitingolo, G., Guarnieri, D., Falanga, A. P. & Netti, P. A. From square to circular polymeric microchannels by spin coating technology: A low cost platform for endothelial cell culture. *Biofabrication* **8**, 025005 (2016).
194. Park, W., Han, S. & Kwon, S. Fabrication of membrane-type microvalves in rectangular microfluidic channels via seal photopolymerization. *Lab Chip* **10**, 2814–2817 (2010).
195. Kamei, K. ichiro *et al.* 3D printing of soft lithography mold for rapid production of polydimethylsiloxane-based microfluidic devices for cell stimulation with concentration gradients. *Biomed. Microdevices* **17**, 36 (2015).
196. Comina, G., Suska, A. & Filippini, D. PDMS lab-on-a-chip fabrication using 3D printed templates. *Lab Chip* **14**, 424–430 (2014).
197. Razavi Bazaz, S. *et al.* Rapid Softlithography Using 3D-Printed Molds. *Adv. Mater. Technol.* 1900425 (2019) doi:10.1002/admt.201900425.
198. Li, X., Brooks, J. C., Hu, J., Ford, K. I. & Easley, C. J. 3D-templated, fully automated microfluidic input/output multiplexer for endocrine tissue culture and secretion sampling. *Lab Chip* **17**, 341–349 (2017).
199. Gong, H., Woolley, A. T. & Nordin, G. P. High density 3D printed microfluidic valves, pumps, and multiplexers. *Lab Chip* **16**, 2450–2458 (2016).
200. Zhang, R. & Larsen, N. B. Stereolithographic hydrogel printing of 3D culture chips with biofunctionalized complex 3D perfusion networks. *Lab Chip* **17**, 4273–4282 (2017).
201. Nie, J. *et al.* 3D printed Lego® -like modular microfluidic devices based on capillary driving. *Biofabrication* **10**, 035001 (2018).
202. Macdonald, N. P. *et al.* Comparing Microfluidic Performance of Three-Dimensional

(3D) Printing Platforms. *Anal. Chem.* **89**, 3858–3866 (2017).

203. Capel, A. J., Rimington, R. P., Lewis, M. P. & Christie, S. D. R. 3D printing for chemical, pharmaceutical and biological applications. *Nat. Rev. Chem.* 1 (2018) doi:10.1038/s41570-018-0058-y.
204. Ligon, S. C., Liska, R., Stampfl, J., Gurr, M. & Mülhaupt, R. Polymers for 3D Printing and Customized Additive Manufacturing. *Chem. Rev.* **117**, 10212–10290 (2017).
205. Rimington, R. P., Capel, A. J., Christie, S. D. R. & Lewis, M. P. Biocompatible 3D printed polymers via fused deposition modelling direct C2C12 cellular phenotype in vitro. *Lab Chip* **17**, 2982–2993 (2017).
206. MacDonald, N. P. *et al.* Assessment of biocompatibility of 3D printed photopolymers using zebrafish embryo toxicity assays. *Lab Chip* **16**, 291–297 (2016).
207. Romanov, V. *et al.* FDM 3D Printing of High-Pressure, Heat-Resistant, Transparent Microfluidic Devices. *Anal. Chem.* **90**, 10450–10456 (2018).
208. Nelson, M. D., Ramkumar, N. & Gale, B. K. Flexible, transparent, sub-100 µ m microfluidic channels with fused deposition modeling 3D-printed thermoplastic polyurethane. *J. Micromechanics Microengineering* **29**, 095010 (2019).
209. Waheed, S. *et al.* 3D printed microfluidic devices: enablers and barriers. *Lab Chip* **16**, 1993–2013 (2016).
210. Keating, S. J. *et al.* 3D printed multimaterial microfluidic valve. *PLoS One* **11**, e0160624 (2016).
211. Siller, I. G. *et al.* Characterization of a customized 3D-printed cell culture system using clear, translucent acrylate that enables optical online monitoring. *Biomed. Mater.* **15**, (2020).
212. Rimington, R. P. *et al.* Feasibility and Biocompatibility of 3D-Printed Photopolymerized and Laser Sintered Polymers for Neuronal, Myogenic, and Hepatic Cell Types. *Macromol. Biosci.* **18**, 1800113 (2018).
213. Zhu, F., Friedrich, T., Nugegoda, D., Kaslin, J. & Wlodkowic, D. Assessment of the biocompatibility of three-dimensional-printed polymers using multispecies toxicity tests. *Biomicrofluidics* **9**, 061103 (2015).
214. Weisgrab, G., Ovsianikov, A. & Costa, P. F. Functional 3D Printing for Microfluidic Chips. *Adv. Mater. Technol.* 1900275 (2019) doi:10.1002/admt.201900275.
215. Carve, M. & Wlodkowic, D. 3D-printed chips: Compatibility of additive manufacturing photopolymeric substrata with biological applications. *Micromachines* vol. 9 91 (2018).
216. Urrios, A. *et al.* 3D-printing of transparent bio-microfluidic devices in PEG-DA. *Lab Chip* **16**, 2287–2294 (2016).
217. Beauchamp, M. J., Gong, H., Woolley, A. T. & Nordin, G. P. 3D printed microfluidic features using dose control in X, Y, and Z dimensions. *Micromachines* **9**, 326 (2018).
218. Barata, D., Provaggi, E., Van Blitterswijk, C. & Habibovic, P. Development of a microfluidic platform integrating high-resolution microstructured biomaterials to study cell-material interactions. *Lab Chip* **17**, 4134–4147 (2017).
219. Chan, H. N. *et al.* Direct, one-step molding of 3D-printed structures for convenient fabrication of truly 3D PDMS microfluidic chips. *Microfluid. Nanofluidics* **19**, 9–18 (2015).
220. Glick, C. C. *et al.* Rapid assembly of multilayer microfluidic structures via 3D-printed transfer molding and bonding. *Microsystems Nanoeng.* **2**, 16063 (2016).
221. Olanrewaju, A. O., Robillard, A., Dagher, M. & Juncker, D. Autonomous microfluidic capillaric circuits replicated from 3D-printed molds. *Lab Chip* **16**, 3804–3814 (2016).
222. Shrestha, J. *et al.* A Rapidly Prototyped Lung-on-a-chip Model Using 3D-Printed Molds. *Organs-on-a-Chip* 100001 (2020) doi:10.1016/j.ooc.2020.100001.

223. Venzac, B. *et al.* PDMS Curing Inhibition on 3D-Printed Molds: Why? Also, How to Avoid It? *Anal. Chem.* **93**, 7180–7187 (2021).
224. Yuan, C. *et al.* Ultrafast Three-Dimensional Printing of Optically Smooth Microlens Arrays by Oscillation-Assisted Digital Light Processing. *ACS Appl. Mater. Interfaces* **11**, 40662–40668 (2019).
225. Cromwell, E. F. *et al.* Disease Modeling with 3D Cell-Based Assays Using a Novel Flowchip System and High-Content Imaging. *SLAS Technol. Transl. Life Sci. Innov.* **26**, 237–248 (2021).
226. Arnold, C., Monsees, D., Hey, J. & Schweyen, R. Surface quality of 3D-printed models as a function of various printing parameters. *Materials (Basel).* **12**, 1–15 (2019).
227. Pandey, P. M., Venkata Reddy, N. & Dhande, S. G. Part deposition orientation studies in layered manufacturing. *J. Mater. Process. Technol.* **185**, 125–131 (2007).
228. Mostafa, K., Qureshi, A. J. & Montemagno, C. Tolerance Control Using Subvoxel Gray-Scale DLP 3D Printing. in *Volume 2: Advanced Manufacturing* 1–7 (American Society of Mechanical Engineers, 2017). doi:10.1115/IMECE2017-72232.
229. Tamura, T. & Suzuki, T. Seamless fabrication technique for micro to millimeter structures by combining 3D printing and photolithography. *Jpn. J. Appl. Phys.* **58**, SDDL10 (2019).
230. Au, A. K., Bhattacharjee, N., Horowitz, L. F., Chang, T. C. & Folch, A. 3D-printed microfluidic automation. *Lab Chip* **15**, 1934–1941 (2015).
231. Wang, J. *et al.* 3D-printed peristaltic microfluidic systems fabricated from thermoplastic elastomer. *Microfluid. Nanofluidics* **21**, 1–13 (2017).
232. Rogers, C. I., Qaderi, K., Woolley, A. T. & Nordin, G. P. 3D printed microfluidic devices with integrated valves. *Biomicrofluidics* **9**, 16501 (2015).
233. Takenaga, S. *et al.* Fabrication of biocompatible lab-on-chip devices for biomedical applications by means of a 3D-printing process. *Phys. Status Solidi Appl. Mater. Sci.* **212**, 1347–1352 (2015).
234. Beckwith, A. L., Borenstein, J. T. & Velasquez-Garcia, L. F. Monolithic, 3D-Printed Microfluidic Platform for Recapitulation of Dynamic Tumor Microenvironments. *J. Microelectromechanical Syst.* **27**, 1009–1022 (2018).
235. Nourmohammadzadeh, M. *et al.* Microfluidic array with integrated oxygenation control for real-time live-cell imaging: Effect of hypoxia on physiology of microencapsulated pancreatic islets. *Anal. Chem.* **85**, 11240–11249 (2013).
236. Grist, S. M., Schmok, J. C., Andy Liu, M. C., Chrostowski, L. & Cheung, K. C. Designing a microfluidic device with integrated ratiometric oxygen sensors for the long-term control and monitoring of chronic and cyclic hypoxia. *Sensors (Switzerland)* **15**, 20030–20052 (2015).
237. Zhu, K. J., Aiani, L. M. & Pedersen, N. P. Reconfigurable 3D-Printed headplates for reproducible and rapid implantation of EEG, EMG and depth electrodes in mice. *J. Neurosci. Methods* **333**, 108566 (2020).
238. Moussus, M. & Meier, M. A 3D-printed Arabidopsis thaliana root imaging platform. *Lab Chip* **21**, 2557–2564 (2021).
239. Hart, C., Didier, C. M., Sommerhage, F. & Rajaraman, S. Biocompatibility of Blank, Post-Processed and Coated 3D Printed Resin Structures with Electrogenic Cells. *Biosensors* **10**, 1–14 (2020).
240. ISO 10993-5:2009. Biological evaluation of medical devices - Part 5: Tests for in vitro cytotoxicity.
241. ISO 10993-12:2009. Biological evaluation of medical devices - Part 12: Sample preparation and reference materials.

242. Tominaga, H. *et al.* A water-soluble tetrazolium salt useful for colorimetric cell viability assay. *Anal. Commun.* **36**, 47–50 (1999).
243. BenSaïda, A. Shapiro-Wilk and Shapiro-Fancia normality tests. (2021).
244. Madsen, M. H., Feidenhans'l, N. A., Hansen, P. E., Garnæs, J. & Dirscherl, K. Accounting for PDMS shrinkage when replicating structures. *J. Micromechanics Microengineering* **24**, 127002 (2014).
245. Lee, S. W. & Lee, S. S. Shrinkage ratio of PDMS and its alignment method for the wafer level process. *Microsyst. Technol.* **14**, 205–208 (2008).
246. Jia, J., Song, Q., Liu, Z. & Wang, B. Effect of wall roughness on performance of microchannel applied in microfluidic device. *Microsyst. Technol.* **25**, 2385–2397 (2019).
247. Sun, J., He, Y., Tao, W., Yin, X. & Wang, H. Roughness effect on flow and thermal boundaries in microchannel/nanochannel flow using molecular dynamics-continuum hybrid simulation. *Int. J. Numer. Methods Eng.* **89**, 2–19 (2012).
248. Villegas, M., Cetinic, Z., Shakeri, A. & Didar, T. F. Fabricating smooth PDMS microfluidic channels from low-resolution 3D printed molds using an omniphobic lubricant-infused coating. *Anal. Chim. Acta* **1000**, 248–255 (2018).
249. Yang, S. Y., Kim, E. S., Jeon, G., Choi, K. Y. & Kim, J. K. Enhanced adhesion of osteoblastic cells on polystyrene films by independent control of surface topography and wettability. *Mater. Sci. Eng. C* **33**, 1689–1695 (2013).
250. Hou, Y. *et al.* Surface Roughness Gradients Reveal Topography-Specific Mechanosensitive Responses in Human Mesenchymal Stem Cells. *Small* **16**, 1905422 (2020).
251. Zhang, K. *et al.* Surface roughness improvement of 3D printed microchannel. *J. Micromechanics Microengineering* **30**, 065003 (2020).
252. Kowsari, K. *et al.* Photopolymer formulation to minimize feature size, surface roughness, and stair-stepping in digital light processing-based three-dimensional printing. *Addit. Manuf.* **24**, 627–638 (2018).
253. Comina, G., Suska, A. & Filippini, D. 3D printed unibody lab-on-a-chip: Features survey and check-valves integration. *Micromachines* **6**, 437–451 (2015).
254. Gonzalez-Fernandez, T., Tenorio, A. J., Kent Leach, J. & Kent Leach, J. Three-Dimensional Printed Stamps for the Fabrication of Patterned Microwells and High-Throughput Production of Homogeneous Cell Spheroids. *3D Print. Addit. Manuf.* **7**, 139–147 (2020).
255. Ruppen, J. *et al.* Towards personalized medicine: chemosensitivity assays of patient lung cancer cell spheroids in a perfused microfluidic platform. *Lab Chip* **15**, 3076–3085 (2015).
256. Argentati, C. *et al.* Surface Hydrophilicity of Poly(l-Lactide) Acid Polymer Film Changes the Human Adult Adipose Stem Cell Architecture. *Polym. 2018, Vol. 10, Page 140* **10**, 140 (2018).
257. Tanyeri, M. & Tay, S. Viable cell culture in PDMS-based microfluidic devices. *Methods in Cell Biology* vol. 148 3–33 (2018).
258. Toyoda, T. *et al.* Cell aggregation optimizes the differentiation of human ESCs and iPSCs into pancreatic bud-like progenitor cells. *Stem Cell Res.* **14**, 185–197 (2015).
259. Sharon, N. *et al.* A Peninsular Structure Coordinates Asynchronous Differentiation with Morphogenesis to Generate Pancreatic Islets. *Cell* **176**, 790-804.e13 (2019).
260. Dahlberg, T. *et al.* 3D printed water-soluble scaffolds for rapid production of PDMS micro-fluidic flow chambers. *Sci. Rep.* **8**, 3372 (2018).
261. Tinevez, J. Y. *et al.* TrackMate: An open and extensible platform for single-particle

tracking. *Methods* **115**, 80–90 (2017).

262. Yoon, D. H., Kobayashi, K., Tanaka, D., Sekiguchi, T. & Shoji, S. Simple microfluidic formation of highly heterogeneous microfibers using a combination of sheath units. *Lab Chip* **17**, 1481–1486 (2017).
263. Kimura, H., Yamamoto, T., Sakai, H., Sakai, Y. & Fujii, T. An integrated microfluidic system for long-term perfusion culture and on-line monitoring of intestinal tissue models. *Lab Chip* **8**, 741–746 (2008).
264. Yang, T., Choo, J., Stavrakis, S. & de Mello, A. Fluoropolymer-Coated PDMS Microfluidic Devices for Application in Organic Synthesis. *Chem. - A Eur. J.* **24**, 12078–12083 (2018).
265. Kuang, X. *et al.* Grayscale digital light processing 3D printing for highly functionally graded materials. *Sci. Adv.* **5**, 1–10 (2019).
266. Beer, M. *et al.* A novel microfluidic 3D platform for culturing pancreatic ductal adenocarcinoma cells: Comparison with in vitro cultures and in vivo xenografts. *Sci. Rep.* **7**, 1325 (2017).
267. Kim, J. Y. *et al.* 3D spherical microtissues and microfluidic technology for multi-tissue experiments and analysis. *J. Biotechnol.* **205**, 24–35 (2015).
268. Armani, D., Liu, C. & Aluru, N. Re-configurable fluid circuits by PDMS elastomer micromachining. in *Technical Digest. IEEE International MEMS 99 Conference. Twelfth IEEE International Conference on Micro Electro Mechanical Systems (Cat. No.99CH36291)* 222–227 (IEEE, 1999). doi:10.1109/MEMSYS.1999.746817.
269. Jin, H.-J. J. *et al.* A multicellular spheroid formation and extraction chip using removable cell trapping barriers. *Lab Chip* **11**, 115–119 (2011).
270. Anada, T. *et al.* Three-dimensional cell culture device utilizing thin membrane deformation by decompression. *Sensors Actuators, B Chem.* **147**, 376–379 (2010).
271. Kosheleva, N. V. *et al.* Cell spheroid fusion: beyond liquid drops model. *Sci. Rep.* **10**, 1–15 (2020).
272. Fleming, P. A. *et al.* Fusion of uniluminal vascular spheroids: A model for assembly of blood vessels. *Dev. Dyn.* **239**, 398–406 (2010).
273. Foty, R. A. & Steinberg, M. S. The differential adhesion hypothesis: A direct evaluation. *Dev. Biol.* **278**, 255–263 (2005).
274. Flenner, E., Marga, F., Neagu, A., Kosztin, I. & Forgacs, G. Relating Biophysical Properties Across Scales. *Curr. Top. Dev. Biol.* **81**, 461–483 (2008).
275. Susienka, M. J., Wilks, B. T. & Morgan, J. R. Quantifying the kinetics and morphological changes of the fusion of spheroid building blocks. *Biofabrication* **8**, 045003 (2016).
276. Hajdu, Z. *et al.* Tissue spheroid fusion-based in vitro screening assays for analysis of tissue maturation. *J. Tissue Eng. Regen. Med.* **4**, 659–664 (2010).
277. Xiang, Y. *et al.* Fusion of Regionally Specified hPSC-Derived Organoids Models Human Brain Development and Interneuron Migration. *Cell Stem Cell* **21**, 383-398.e7 (2017).
278. Wu, Z. *et al.* CD146 is a Novel ANGPTL2 Receptor that Promotes Obesity by Manipulating Lipid Metabolism and Energy Expenditure. *Adv. Sci.* **2004032**, 1–17 (2021).
279. Renes, J., Rosenow, A., Roumans, N., Noben, J.-P. & Mariman, E. C. M. Calorie restriction-induced changes in the secretome of human adipocytes, comparison with resveratrol-induced secretome effects. *Biochim. Biophys. Acta - Proteins Proteomics* **1844**, 1511–1522 (2014).
280. Kugo, H. *et al.* Low glucose and serum levels cause an increased inflammatory factor in

3T3-L1 cell through Akt, MAPKs and NF-κB activation. *Adipocyte* **10**, 232–241 (2021).

281. Volz, A.-C., Omengo, B., Gehrke, S. & Kluger, P. J. Comparing the use of differentiated adipose-derived stem cells and mature adipocytes to model adipose tissue in vitro. *Differentiation* **110**, 19–28 (2019).
282. Shen, J. X. *et al.* 3D Adipose Tissue Culture Links the Organotypic Microenvironment to Improved Adipogenesis. *Adv. Sci.* **8**, 2100106 (2021).
283. Grandl, G. *et al.* Depot specific differences in the adipogenic potential of precursors are mediated by collagenous extracellular matrix and Flotillin 2 dependent signaling. *Mol. Metab.* **5**, 937–947 (2016).
284. McCarthy, M. *et al.* Fat-on-a-Chip models for research and discovery in obesity and its metabolic co-morbidities. *Tissue Eng. Part B Rev.* **26**, 586–595 (2020).
285. Slaughter, V. L. *et al.* Validation of an adipose-liver human-on-a-chip model of NAFLD for preclinical therapeutic efficacy evaluation. *Sci. Rep.* **11**, 13159 (2021).
286. Pope, B. D., Warren, C. R., Parker, K. K. & Cowan, C. A. Microenvironmental Control of Adipocyte Fate and Function. *Trends Cell Biol.* **26**, 745–755 (2016).
287. Gibler, P. *et al.* Human Adipose-Derived Stromal/Stem Cell Culture and Analysis Methods for Adipose Tissue Modeling In Vitro: A Systematic Review. *Cells* **10**, 1378 (2021).
288. Bender, R. *et al.* Human Adipose Derived Cells in Two- and Three-Dimensional Cultures: Functional Validation of an In Vitro Fat Construct. *Stem Cells Int.* **2020**, 1–14 (2020).
289. Ioannidou, A. *et al.* Hypertrophied human adipocyte spheroids as in vitro model of weight gain and adipose tissue dysfunction. *bioRxiv* (2021) doi:https://doi.org/10.1101/2021.01.06.425629.
290. Daquinag, A. C., Souza, G. R. & Kolonin, M. G. Adipose Tissue Engineering in Three-Dimensional Levitation Tissue Culture System Based on Magnetic Nanoparticles. *Tissue Eng. Part C Methods* **19**, 336–344 (2013).
291. Harms, M. J. *et al.* Mature Human White Adipocytes Cultured under Membranes Maintain Identity, Function, and Can Transdifferentiate into Brown-like Adipocytes. *Cell Rep.* **27**, 213-225.e5 (2019).
292. Li, X. & Easley, C. J. Microfluidic systems for studying dynamic function of adipocytes and adipose tissue. *Anal. Bioanal. Chem.* **410**, 791–800 (2018).
293. Zambon, A. *et al.* High Temporal Resolution Detection of Patient-Specific Glucose Uptake from Human ex Vivo Adipose Tissue On-Chip. *Anal. Chem.* **87**, 6535–6543 (2015).
294. Hu, J., Li, X., Judd, R. L. & Easley, C. J. Rapid lipolytic oscillations in ex vivo adipose tissue explants revealed through microfluidic droplet sampling at high temporal resolution. *Lab Chip* **20**, 1503–1512 (2020).
295. Dugan, C. E., Cawthorn, W. P., MacDougald, O. A. & Kennedy, R. T. Multiplexed microfluidic enzyme assays for simultaneous detection of lipolysis products from adipocytes. *Anal. Bioanal. Chem.* **406**, 4851–4859 (2014).
296. Devaud, Y. R. *et al.* Label-Free Quantification Proteomics for the Identification of Mesenchymal Stromal Cell Matrisome Inside 3D Poly(Ethylene Glycol) Hydrogels. *Adv. Healthc. Mater.* **7**, 1800534 (2018).
297. Zhang, X. *et al.* Proteome-wide identification of ubiquitin interactions using UbIA-MS. *Nat. Protoc.* **13**, 530–550 (2018).
298. Szklarczyk, D. *et al.* STRING v11: protein–protein association networks with increased coverage, supporting functional discovery in genome-wide experimental datasets. *Nucleic Acids Res.* **47**, D607–D613 (2019).

299. Frank, T. & Tay, S. Flow-switching allows independently programmable, extremely stable, high-throughput diffusion-based gradients. *Lab Chip* **13**, 1273–1281 (2013).

300. Tsai, A.-C., Liu, Y., Yuan, X. & Ma, T. Compaction, Fusion, and Functional Activation of Three-Dimensional Human Mesenchymal Stem Cell Aggregate. *Tissue Eng. Part A* **21**, 1705–1719 (2015).

301. Hammel, J. H. & Bellas, E. Endothelial cell crosstalk improves browning but hinders white adipocyte maturation in 3D engineered adipose tissue. *Integr. Biol. (Camb).* **12**, 81–89 (2020).

302. Halbgebauer, D., Dahlhaus, M., Wabitsch, M., Fischer-Posovszky, P. & Tews, D. Browning capabilities of human primary adipose-derived stromal cells compared to SGBS cells. *Sci. Rep.* **10**, 9632 (2020).

303. Didier, P. *et al.* Differentiation of human adipose-derived stem cells into "brite" (brown-in-white) adipocytes. *Front. Endocrinol. (Lausanne).* **2**, 1040 (2011).

304. Taylor, J. *et al.* Generation of immune cell containing adipose organoids for in vitro analysis of immune metabolism. *Sci. Rep.* **10**, 21104 (2020).

305. Sandoz, P. A. *et al.* Label free 3D analysis of organelles in living cells by refractive index shows pre-mitotic organelle spinning in mammalian stem cells. *bioRxiv* 407239 (2018) doi:10.1101/407239.

306. Schürmann, M., Scholze, J., Müller, P., Guck, J. & Chan, C. J. Cell nuclei have lower refractive index and mass density than cytoplasm. *J. Biophotonics* **9**, 1068–1076 (2016).

307. Ambele, M. A., Dessels, C., Durandt, C. & Pepper, M. S. Genome-wide analysis of gene expression during adipogenesis in human adipose-derived stromal cells reveals novel patterns of gene expression during adipocyte differentiation. *Stem Cell Res.* **16**, 725–734 (2016).

308. de Oliveira, C. *et al.* Pancreatic triglyceride lipase mediates lipotoxic systemic inflammation. *J. Clin. Invest.* **130**, 1931–1947 (2020).

309. Wenzel, J. J. *et al.* ABCA10, a novel cholesterol-regulated ABCA6-like ABC transporter. *Biochem. Biophys. Res. Commun.* **306**, 1089–1098 (2003).

310. Swindell, W. R. Genes regulated by caloric restriction have unique roles within transcriptional networks. *Mech. Ageing Dev.* **129**, 580–592 (2008).

311. Dhahbi, J. M., Tsuchiya, T., Kim, H. J., Mote, P. L. & Spindler, S. R. Gene Expression and Physiologic Responses of the Heart to the Initiation and Withdrawal of Caloric Restriction. *Journals Gerontol. Ser. A* **61**, 218–231 (2006).

312. Qiao, Q., Bouwman, F. G., Van Baak, M. A., Renes, J. & Mariman, E. C. M. Glucose Restriction Plus Refeeding in Vitro Induce Changes of the Human Adipocyte Secretome with an Impact on Complement Factors and Cathepsins. *Int. J. Mol. Sci. 2019, Vol. 20, Page 4055* **20**, 4055 (2019).

313. Klusóczki, Á. *et al.* Differentiating SGBS adipocytes respond to PPARγ stimulation, irisin and BMP7 by functional browning and beige characteristics. *Sci. Rep.* **9**, 5823 (2019).

314. Müller, S. *et al.* Proteomic Analysis of Human Brown Adipose Tissue Reveals Utilization of Coupled and Uncoupled Energy Expenditure Pathways. *Sci. Reports 2016 61* **6**, 1–9 (2016).

315. Gardell, A. M. *et al.* Tilapia (Oreochromis mossambicus) brain cells respond to hyperosmotic challenge by inducing myo-inositol biosynthesis. *J. Exp. Biol.* **216**, 4615–4625 (2013).

316. Youssef-Elabd, E. M. *et al.* Acute and chronic saturated fatty acid treatment as a key instigator of the TLR-mediated inflammatory response in human adipose tissue, in vitro. *J. Nutr. Biochem.* **23**, 39–50 (2012).

317. Rodriguez-Moncayo, R., Jimenez-Valdes, R. J., Gonzalez-Suarez, A. M. & Garcia-Cordero, J. L. Integrated Microfluidic Device for Functional Secretory Immunophenotyping of Immune Cells. *ACS Sensors* **5**, 353–361 (2020).

318. Zhu, J. *et al.* An integrated adipose-tissue-on-chip nanoplasmonic biosensing platform for investigating obesity-associated inflammation. *Lab Chip* **18**, 3550–3560 (2018).

319. Huang, L. *et al.* Multisensor-integrated organs-on-chips platform for automated and continual in situ monitoring of organoid behaviors. *Proc. Natl. Acad. Sci. U. S. A.* **114**, E2293–E2302 (2017).

320. Misun, P. M., Rothe, J., Schmid, Y. R. F., Hierlemann, A. & Frey, O. Multi-analyte biosensor interface for real-time monitoring of 3D microtissue spheroids in hanging-drop networks. *Microsystems Nanoeng.* **2**, (2016).

321. Bavli, D. *et al.* Real-time monitoring of metabolic function in liver-onchip microdevices tracks the dynamics of Mitochondrial dysfunction. *Proc. Natl. Acad. Sci. U. S. A.* **113**, E2231–E2240 (2016).

322. Compera, N. *et al.* Adipose microtissue-on-chip: A 3D cell culture platform for differentiation, stimulation, and proteomic analysis of human adipocytes. *Lab Chip* **22**(17), 3172–3186 (2022).

Author’s list of journal publications

- **Compera, N.**, Atwell, S., Wirth, J., Wolfrum, B. & Meier, M. Upscaling of pneumatic membrane valves for the integration of 3D cell cultures on-chip. *Lab Chip*, 21(15), 2986–2996 (2021).
- **Compera, N.**, Atwell, S., Wirth, J., von Toerne, C., Hauck, S., & Meier, M. Adipose microtissue-on-chip: A 3D cell culture platform for differentiation, stimulation, and proteomic analysis of human adipocytes. *Lab Chip*, 22(17), 3172–3186 (2022).
- Ardila Riveros, J. C., Bloechinger, A. K., Atwell, S., Moussus, M., **Compera, N.**, Rajabnia, O., Georgiev, T., Lickert, H. & Meier, M. Automated optimization of endoderm differentiation on chip. *Lab Chip*, 21(23), 4685 – 4695 (2021).
- Wirth, J., **Compera, N.**, Yin, K., Brood, S., Chang, S., Martinez-Jimenez, C. P., & Meier, M.: Spatial Transcriptomics Using Multiplexed Deterministic Barcoding in Tissue. *bioRxiv*, 2022-08 (2022).